

LOW TEMPERATURE SYNTHESIS AND CHARACTERIZATION OF  
SOME LOW POSITIVE AND NEGATIVE THERMAL EXPANSION  
MATERIALS

A Dissertation  
Presented to  
The Academic Faculty

by

Kathleen Madara White

In Partial Fulfillment  
of the Requirements for the Degree  
Doctor of Philosophy in Chemistry

Georgia Institute of Technology  
August 2006

LOW TEMPERATURE SYNTHESIS AND CHARACTERIZATION OF  
SOME LOW POSITIVE AND NEGATIVE THERMAL EXPANSION  
MATERIALS

Approved by:

Dr. Angus P. Wilkinson, Chairman  
School of Chemistry and Biochemistry  
*Georgia Institute of Technology*

Dr. E. Kent Barefield  
School of Chemistry and Biochemistry  
*Georgia Institute of Technology*

Dr. Jiri Janata  
School of Chemistry and Biochemistry  
*Georgia Institute of Technology*

Dr. John Zhang  
School of Chemistry and Biochemistry  
*Georgia Institute of Technology*

Dr. Meilin Liu  
School of Materials Science & Engineering  
*Georgia Institute of Technology*

Date Approved: July 07, 2006

To

my husband Jack

and

my sons

Jordan and Jason

## ACKNOWLEDGEMENTS

This work would not have been possible without the help, patience, and support of my advisor, Dr. Angus P. Wilkinson. My heartfelt gratitude and thanks go to him for making the graduate experience challenging and rewarding, and for giving me the opportunities to gain knowledge I had never thought possible.

I thank my committee members, valued professors during my time at GA Tech, for their generous contribution of their time, advice, and encouragement: Dr. Jiri Janata, Dr. Kent Barefield, Dr. John Zhang, and Dr. Meilin Liu.

My research gave me opportunities to travel to work with experts in their fields. I would like to thank Dr. Peter Lee and Dr. Peter Chupas from the Advanced Photon Source (APS) at Argonne National Labs. Dr. Lee and Dr. Chupas brought their expertise and tireless dedication to experiments on  $A^{IV}M^V_2O_7$  materials using high resolution, high temperature thermal expansion, and dehydration synchrotron powder XRD methods. High pressure synchrotron powder XRD studies at the CHESS facility, Cornell University, gave me the opportunity to work with Dr. Bill Bassett, whose willingness to contribute his time and expertise resulted in successful completion of experiments on  $A^{IV}M^V_2O_7$  compounds. Dr. Andrew Payzant, Dr. Scott Speakman, and Dr. Jane Howe at Oak Ridge National Labs deserve thanks and commendation for their enthusiastic help, time, and knowledge involving high temperature powder XRD and electron diffraction studies on both  $A^{IV}M^V_2O_7$  and  $M^{III}M^V_2P_4O_{14}$  materials.

I would like to thank Dr. Don Vanderveer, Dr. Juliana Cernatescu, and Dr. Johannes Leisen at GA Tech for their help in single crystal XRD, electron diffraction,

and solid state MAS  $^{31}\text{P}$ -NMR analyses, respectively.

Special thanks and appreciation go to Dr. Andrew Jupe, a member of our research group, for his extensive knowledge, time, and effort in collaboration on refinement methods for powder diffraction. I would like to thank Dr. Tamas Varga, a former group member, whose kindness and patience in helping me get started in the lab and helpful contributions of his experience are greatly appreciated. For their unwavering friendship, encouragement, and generous support, I would like to thank Mehmet Centinkol and former group member Mehmet Kutuchu.

I would like to thank many of my former undergraduate professors and friends at Kennesaw State University for their unwavering support, enthusiasm, and guidance during my graduate experience: Dr. Dan Williams, Dr. Marina Koether, Dr. Jennifer Powers, Ben Huck, and Dr. Patricia Reggio now at UNC Greensboro.

Graduate studies at GA Tech would not have been possible without the love, understanding, patience, and tireless encouragement of my husband, Jack, and sons, Jordan and Jason. It is to them I dedicate this work.

## TABLE OF CONTENTS

ACKNOWLEDGEMENTS	iv
LIST OF TABLES	x
LIST OF FIGURES	xi
LIST OF EQUATIONS, RELATIONSHIPS, AND SCHEMES	xvii
SUMMARY	xix
CHAPTER 1 INTRODUCTION	1
1.1 Thermal Expansion	1
1.1.1 Low or Negative Thermal Expansion (NTE) in Open Framework Materials	8
1.1.2 Methods to Control Thermal Expansion	14
1.2 The $A^{IV}M^V_2O_7$ Family of Compounds	15
1.2.1 Properties of $A^{IV}$ Pyrophosphates and $A^{IV}$ Pyrovanadates	17
1.2.2 Synthesis of $A^{IV}$ Pyrophosphates and $A^{IV}$ Pyrovanadates	18
1.2.3 Solid Solutions	21
1.2.4 The $M^{III}M^V P_4O_{14}$ Family – Structural Relatives of HT $ZrP_2O_7$	22
1.3 Other Families of Low or NTE Compounds	22
1.3.1 $A^{IV}M^{VI}_2O_8$	22
1.3.2 $A^{III}_2M^{VI}_3O_{12}$ Family	23
1.3.3 NZP (NASICON) Family	24
1.3.4 The $A^{IV}_2M^V_2O_9$ Family	25
1.3.5 Lithia-Alumina-Silica (LAS) $Li_2O-Al_2O_3-SiO_2$ Family	25
1.3.6 Cordierite Family ( $2MgO \cdot 2Al_2O_3 \cdot 5SiO_2$ )	26

1.3.7	Silica and SiO <sub>2</sub> -TiO <sub>2</sub> Glasses	27
1.3.8	Zeodur	27
1.3.9	Invar	28
1.4	Goals of Research	28
1.5	References	30
CHAPTER 2 INSTRUMENTAL METHODS AND DATA ANALYSIS		36
2.1	X-Ray Diffraction	36
2.1.1	Powder X-Ray Diffraction (Powder XRD) and Variable Temperature Thermal Expansion Analysis at Georgia Institute of Technology and at Oak Ridge National Laboratory, Oak Ridge, TN	41
2.1.2	Synchrotron Powder XRD	43
2.1.3	Synchrotron Powder XRD at Argonne National Labs, Argonne, IL	43
2.1.4	High Pressure Synchrotron Powder XRD at CHESS	47
2.2	Transmission Electron Microscopy	50
2.3	Thermal Analysis	52
2.3.1	TG/DTA	53
2.4	MAS <sup>31</sup> P-NMR	53
2.5	Software	54
2.5.1	JADE	54
2.5.2	Rietveld Refinement and LeBail Fitting	54
2.5.3	CRYSFIRE and CHECKCELL	55
2.5.4	Fit2d	56
2.6	References	57
CHAPTER 3 LOW TEMPERATURE SYNTHESIS AND CHARACTERIZATION OF SOME A <sup>IV</sup> M <sup>V</sup> <sub>2</sub> O <sub>7</sub> COMPOUNDS: ZrP <sub>2</sub> O <sub>7</sub> , ZrV <sub>2</sub> O <sub>7</sub> , CeP <sub>2</sub> O <sub>7</sub> , AND PbP <sub>2</sub> O <sub>7</sub>		60

3.1 Introduction	60
3.1.1 Hydrolytic and Non-hydrolytic Sol-Gel Synthesis	62
3.1.2 Autoclave Techniques	66
3.2 Non-hydrolytic Sol-Gel Synthesis of $\text{ZrP}_2\text{O}_7$ ( <i>KMW02</i> and <i>KMW04</i> )	66
3.2.1 Experimental	67
3.2.2 Results and Discussion	68
3.3 Non-hydrolytic Sol-gel Synthesis of $\text{ZrV}_2\text{O}_7$	72
3.3.1 Non-hydrolytic Sol-Gel Synthesis of $\text{V}_2\text{O}_5$ ( <i>KMW11</i> , <i>KMW14</i> , <i>KMW15</i> , and <i>KMW19</i> )	72
3.3.1.1 Experimental	72
3.3.1.2 Results and Discussion	73
3.3.2 Non-hydrolytic Sol-Gel Synthesis of $\text{ZrV}_2\text{O}_7$ ( <i>KMW23</i> , <i>KMW24</i> , <i>KMW25</i> , <i>KMW26</i> , <i>KMW27</i> , <i>KMW38</i> )	74
3.3.2.1 Experimental	74
3.3.2.2 Results and Discussion	75
3.4 Synthesis of $\text{ZrP}_2\text{O}_7$ Directly From Zirconium and Phosphorus Starting Materials Using Mild Autoclave Conditions ( <i>KMW95</i> and <i>KMW122</i> )	78
3.4.1 Experimental	79
3.4.2 Results and Discussion	79
3.5 Low Temperature Synthesis, Structural Studies, High Pressure Behavior, and Thermal Properties of $\text{CeP}_2\text{O}_7$	80
3.5.1 Experimental	81
3.5.2 Results and Discussion	82
3.5.2.1 Structural Studies	82
3.5.2.2 High Pressure Synchrotron Powder XRD	94

3.5.2.3	Thermophysical Properties	103
3.6	Synthesis and Thermal Properties of $\text{PbP}_2\text{O}_7$ ( <i>KMW311</i> )	112
3.6.1	Experimental	112
3.6.2	Results and Discussion	113
3.7	Conclusion	118
3.8	References	121
CHAPTER 4 SYNTHESIS AND CHARACTERIZATION OF SOME $\text{M}^{\text{III}}\text{M}'^{\text{V}}\text{P}_4\text{O}_{14}$ , STRUCTURAL RELATIVES OF $\text{ZrP}_2\text{O}_7$		127
4.1	Introduction	127
4.2	Synthesis and Thermal Properties of $\text{M}^{\text{III}}\text{M}'^{\text{V}}\text{P}_2\text{O}_7$ Compounds ( <i>KMW255</i> , <i>KMW256</i> , <i>KMW257</i> , <i>KMW262</i> , <i>KMW263</i> , <i>KMW287</i> , and <i>KMW296</i> )	131
4.2.1	Experimental	131
4.2.2	Results and Discussion	132
4.2.3	Electron Diffraction	145
4.3	Conclusion	146
4.4	References	149
CHAPTER 5 POSSIBLE AREAS FOR FUTURE STUDY		150

## LIST OF TABLES

Table 3.1	ZrP <sub>2</sub> O <sub>7</sub> Fractional Atom Positions, P a -3 Symmetry Operations, and Transformation Atom Coordinates for CeP <sub>2</sub> O <sub>7</sub>	87
Table 3.2	Refined Fractional Coordinates and Equivalent Isotropic Displacement Parameters	88
Table 3.3	Refined Bond Distances (Å) and Bond Angles (°) for Ce:O From TOPAS Refinement	89
Table 3.4	Refined P-O Bond Distances (Å) and Bond Angles (°) for CeP <sub>2</sub> O <sub>7</sub> from TOPAS	90
Table 3.5	Refined Ce – O – P Bond Angles (°) for CeP <sub>2</sub> O <sub>7</sub> from TOPAS	91
Table 3.6	Pressure (GPa), Refined Lattice Constants (Å), Cell Volumes (Å <sup>3</sup> ), and Ruby Peak Widths (nm) for CeP <sub>2</sub> O <sub>7</sub>	97
Table 3.7	Refined Lattice Constants (Å) and Temperature for CeP <sub>2</sub> O <sub>7</sub> Thermal Expansion Study (ORNL Data)	106
Table 3.8	Refined Atom Coordinates for PbP <sub>2</sub> O <sub>7</sub> from Rietveld Refinement; ZrP <sub>2</sub> O <sub>7</sub> model	113
Table 3.9	Bond Distances and Angles from Refinement of PbP <sub>2</sub> O <sub>7</sub>	114
Table 3.10	Refined Lattice Constants (Å) and Temperature (°C) for PbP <sub>2</sub> O <sub>7</sub> ORNL Data	115
Table 4.1	Summary of Data for M <sup>III</sup> M <sup>V</sup> P <sub>4</sub> O <sub>14</sub> Compounds	138

## LIST OF FIGURES

Figure 1.1:	Graphic representation of anharmonic pair potential, $\phi$ , as a function of interatomic distance, $r$ , showing vibration at two different temperatures ( $T_2 > T_1$ ), demonstrating positive thermal expansion. Modified from Barrera, et al.	2
Figure 1.2:	Graphic representation of harmonic pair potential, $\phi$ , as a function of interatomic distance, $r$ , showing vibration at two different temperatures ( $T_2 > T_1$ ), where the mean distance does not change with temperature.	3
Figure 1.3:	Categories for materials based on CTE.	8
Figure 1.4:	Drawing depicts M-O-M linkages (metals shown as gray circles; oxygen atoms are open circles) and effect of longitudinal (left) and transverse (right) oxygen atom vibrations on M-M distance. Modified from Evans, Mary, and Sleight.	9
Figure 1.5:	Left, two-dimension representation of rigid corner-sharing polyhedra; right, the reduction of volume as temperature increases. The individual polyhedra show no distortion with increasing temperature. Modified from Evans.	10
Figure 1.6:	(a) A square lattice of rigid $\text{MO}_4$ units; M filled circles, O open circles. (b) Rotational displacements in the lattice shown in (a) illustrating effect of a RUM in the lattice with a bent M-O-M angle $\pi - 2\theta$ . Modified from Barrera, et al.	10
Figure 1.7:	Changes of cell edges, $a$ and $c$ , and volume for $\text{PbTiO}_3$ with increasing T. Cell volume reaches minimum close to $490^\circ\text{C}$ . Modified from Sleight.	13
Figure 1.8:	Structure of cubic $\text{A}^{\text{IV}}\text{M}^{\text{V}}_2\text{O}_7$ family consisting of $\text{A}^{\text{IV}}\text{O}_6$ octahedra (dark) and $\text{MO}_4$ tetrahedra (light) in a corner-sharing arrangement resembling the NaCl structure.	16
Figure 1.9:	Compilation plots of lattice constant ( $\text{\AA}$ ) vs temperature for some $\text{A}^{\text{IV}}\text{M}^{\text{V}}_2\text{O}_7$ compounds. Modified from Sleight.	20
Figure 1.10:	Percent relative expansion versus temperature for three solid solutions of the $\text{A}^{\text{III}}_2\text{M}^{\text{VI}}_3\text{O}_{12}$ family. Modified from Evans	24
Figure 2.1:	Diagram of powder XRD on microcrystalline sample	

	showing incident beam, diffracted beam to a detector through a receiving slit, and the Bragg angle of diffraction.	37
Figure 2.2:	X-ray radiation diffracting (solid arrows) from two parallel lattice planes and incident beams (dotted arrows). The angle $2\theta$ is that which is made between the incident and diffracting beams; $d$ is the distance between planes and $\lambda$ is the wavelength.	37
Figure 2.3:	Top, Panalytical X'Pert Pro experimental set up with furnace at Oak Ridge National Labs. Bottom, sample stage; sample is transferred to the round ceramic lipped holder at the top.	42
Figure 2.4:	Experimental set up using a furnace modified for heating capillaries. The samples in this experiment were heated in air. Picture modified from T. Varga.	44
Figure 2.5:	Experimental set up on 32ID beamline at APS. Spinning sample unit holds 1 mm capillary. Black, angular device holds detector array. Photo courtesy Dr. Peter Lee.	46
Figure 2.6:	Detector array on 32ID beamline showing four of the eleven NaI detector heads, Si (111) crystal analyzers, and beam slits inside housing unit. Photo courtesy Dr. Peter Lee.	46
Figure 2.7:	High pressure synchrotron experimental set up at CHESS. Sample stage is on the optical table and apparatus to center the collimated beam are shown.	48
Figure 2.8:	Two halves of unassembled four post DAC showing 1/3 carat diamonds on each half.	49
Figure 2.9:	Assembled, but open, DAC receiving methanol/ethanol pressure transmitting medium via capillary tubing.	50
Figure 3.1:	JADE identification of supercell, room temperature structure for $ZrP_2O_7$ prepared by non-hydrolytic sol-gel methods ( <i>KMW04</i> ). Inset shows weak supercell peaks of powder pattern matching those in the PDF database for the compound.	69
Figure 3.2:	MAS $^{31}P$ -NMR of <i>KMW02</i> , the synthetic product.	70
Figure 3.3:	MAS $^{31}P$ -NMR (a) experimental results for crystalline $ZrP_2O_7$ ( <i>KMW02</i> ), horizontal scale is in ppm.	71

Figure 3.4:	Powder XRD patterns for $ZrV_2O_7$ ( <i>KMW23</i> ) at room temperature and after heating between 300 - 700°C. Some impurity peaks from $V_2O_5$ are observed; arrows point to areas on the 700°C scan where impurity peaks decrease or disappear when compared to the 600°C scan.	76
Figure 3.5:	TG/DTA of raw product, $ZrV_2O_7$ . Arrows indicate temperatures at which mass losses occur.	77
Figure 3.6:	Powder pattern for <i>KMW95</i> matched to the cubic supercell structure for $ZrP_2O_7$ .	80
Figure 3.7:	Zoom images of GSAS RAWPLOT scans d-spacing 2.34-2.52 Å for room temperature $CeP_2O_7$ ; (a) lab powder XRD and (b) high resolution synchrotron powder XRD.	83
Figure 3.8:	Room temperature MAS $^{31}P$ -NMR for $CeP_2O_7$ . Arrows point to two areas of overlap indicating possibly more than one closely related P group.	85
Figure 3.9:	GSAS LeBail fit to high resolution synchrotron data for $CeP_2O_7$ using quasi-cubic unit cell. Lower curve under vertically oriented symmetry tick marks is the difference curve; inset shows experimental data (top curve) and difference curve (lower curve) of representative low intensity peaks not accounted for by this model.	86
Figure 3.10:	(a) Graphic represents the refined structure of $CeP_2O_7$ in P 1 using refined atom positions and filling atoms around the unit cell for comparison to (b), representation of a cubic structure in P a -3 modeled with Ce, P, and O using $ZrP_2O_7$ as a model. For (a) and (b), Ce is large medium gray, P is small light gray, and O is black.	93
Figure 3.11:	Compiled plots of high pressure synchrotron study on $CeP_2O_7$ from the initial “as closed” pressure of 0.00 GPa_1 to 3.17 GPa. Appearance of small peaks denoted by arrows at 1.29 GPa. Peak intensities are incremented by 200 counts additively.	94
Figure 3.12:	Compiled scans of synchrotron powder patterns for increasing pressures. Peak intensity decreases with increasing pressure. Some new peaks disappear; one peak appears at around 12.4 two-theta (°) at 6.23 GPa, indicated by arrow, is attributed to ruby diffraction. Peak intensities are incremented by 200 counts additively.	95

Figure 3.13:	Compiled scans of synchrotron powder patterns from the maximum pressure attained, 10.4 GPa, to ambient pressure, designated as 0.0 GPa <sub>2</sub> . The initial “as-closed” scan, labeled 0.0 GPa <sub>1</sub> is included for comparison. The arrow indicates the appearance of small peaks in the two-theta (°) range 8.3 – 9.4, which do not appear at the lower pressure (0.0 GPa <sub>2</sub> ). Peak intensities are incremented by 200 counts additively.	96
Figure 3.14:	Powder XRD scan at final pressure, 0.00 GPa <sub>2</sub> , showing retention of amorphous component (bracketed) that developed at around 2.73 – 3.17 GPa (increasing pressure).	97
Figure 3.15:	Plots of refined lattice constant and FWHM versus pressure for CeP <sub>2</sub> O <sub>7</sub> . Lattice constant vs. pressure curve shows steadily decreasing lattice constants. One subtle change in slope (indicated by bold, dashed line) at 1.29 GPa may indicate a pressure-induced phase change. Error bars are included.	100
Figure 3.16:	Plot of refined peak width for ruby spectra versus pressure. Data reflects measurements prior to scanning of sample. Error bars are included.	101
Figure 3.17:	Plot of pressure versus the log of volume. Straight lines are fit to two sets of data that reflect obvious differences in decreasing cell volume. The bulk modulus for each straight line fit is shown in the legend.	102
Figure 3.18:	TG/DTA of Ce(HPO <sub>4</sub> ) <sub>2</sub> · 2.1H <sub>2</sub> O. Heating ramp rate was 10°C per minute in argon gas; 25-1109°C. Regions 1 – 4 indicate percent mass loss used in calculations.	104
Figure 3.19:	Contour plot of <i>in situ</i> high temperature synchrotron powder XRD scans for Ce(HPO <sub>4</sub> ) <sub>2</sub> · 1.6 H <sub>2</sub> O; capillary, 1.3°C/minute heating ramp rate in argon gas. Estimated temperatures are taken from observed temperatures, ramp rate, and scan times. The Phases Identified column refers to analyses of individual scans at each temperature using powder diffraction database files in JADE. Lines across the plot indicate blocks of contour scans where apparent phase changes occur.	106
Figure 3.20:	Third and fifth major low angle peaks from synchrotron thermal expansion study for all temperatures explored. Low temperature scans show decreasing two-theta (°) values; higher temperature scans show increasing two-theta (°) values.	107

Figure 3.21:	Refined lattice constant versus temperature for $\text{CeP}_2\text{O}_7$ showing thermal expansion behavior between room temperature and $805^\circ\text{C}$ ; error bars are included. Data obtained at Oak Ridge National Labs (ORNL).	109
Figure 3.22:	Modified figure from Sleight with TE curve of $\text{CeP}_2\text{O}_7$ fit to approximate scale.	111
Figure 3.23:	Zoom image of two-theta ( $^\circ$ ) range 15.0 – 56.0. Crosses on peaks represent experimental data. Outline of peak shapes represent refined data. Vertical lines are reflections for $\text{P a } \bar{3}$ space group. Lower curve is difference pattern between refined and experimental data. Arrows indicate un-modeled peaks.	114
Figure 3.24:	Lattice constant versus temperature curve for $\text{PbP}_2\text{O}_7$ from <i>in situ</i> thermal expansion study at ORNL ( $25 - 340^\circ\text{C}$ ). A linear curve is fit to the data points showing a high degree of linearity based on the R value of 0.99979. Error bars are included. All sigma values are 0.0001 for lattice constants.	118
Figure 4.1:	Plot of refined lattice constant versus temperature from data supplied by J. S. O. Evans for $\text{ZrP}_2\text{O}_7$ showing the long-range to short range order phase transition around $290^\circ\text{C}$ .	129
Figure 4.2:	(a) Compiled plots of refined lattice constants versus temperature for $\text{AlTaP}_4\text{O}_{14}$ , $\text{AlNbP}_4\text{O}_{14}$ , and $\text{GaNbP}_4\text{O}_{14}$ . Data for $\text{AlTaP}_4\text{O}_{14}$ obtained from Varga et al. (b) Compiled plots for the remaining $\text{M}^{\text{III}}\text{M}^{\text{V}}$ -pyrophosphate compounds.	133
Figure 4.3:	Plots of lattice constant versus temperature for (a) $\text{AlNbP}_4\text{O}_{14}$ , (b) $\text{InNbP}_4\text{O}_{14}$ , and (c) $\text{BiTaP}_4\text{O}_{14}$ showing possible phase transitions. Error bars are not included for clarity.	134
Figure 4.4:	Zoom image of powder pattern obtained from ORNL data for $\text{AlNbP}_4\text{O}_{14}$ . Peaks match those for PDF # 00-038-1468, cubic superlattice, $\text{TiP}_2\text{O}_7$ . Vertical reflections for $\text{TiP}_2\text{O}_7$ are shown through peaks of pattern.	135
Figure 4.5:	Zoom image of powder pattern obtained from ORNL data for $\text{GaNbP}_4\text{O}_{14}$ . Peaks match those for PDF # 00-038-1468, cubic superlattice, $\text{TiP}_2\text{O}_7$ . Vertical reflections for $\text{TiP}_2\text{O}_7$ are shown through peaks of pattern.	135
Figure 4.6:	Zoom image of powder pattern obtained from ORNL	

- data for  $\text{BiTaP}_4\text{O}_{14}$ . Below the powder pattern are reflections from the PDF that show peaks in the pattern match those for PDF # 00-010-0004, cubic  $\text{ZrP}_2\text{O}_7$ , and two impurity phases: PDF # 00-025-0932,  $\text{TaPO}_4$  and PDF # 00-016-0906,  $\text{BiTaPO}_4$ . 136
- Figure 4.7: Powder pattern obtained from Scintag data for  $\text{ScNbP}_4\text{O}_{14}$ . Vertical lines through the peaks represent reflections for cubic  $\text{ZrP}_2\text{O}_7$  (PDF # 00-010-0004). One peak, indicated by ^, could be from an unidentified impurity. 137
- Figure 4.8: Powder pattern obtained from Scintag data for  $\text{InNbP}_4\text{O}_{14}$ . Vertical lines through the peaks represent reflections for cubic  $\text{ZrP}_2\text{O}_7$  (PDF # 00-010-0004). Two peaks, indicated by arrows, could belong to an unidentified impurity phase. 138
- Figure 4.9: Powder pattern from ORNL data for  $\text{YbNbP}_4\text{O}_{14}$ . Peaks match those for PDF # 00-010-0004, cubic  $\text{ZrP}_2\text{O}_7$ . Vertical lines from the baseline of the patterns through the peaks for  $\text{YbNbP}_4\text{O}_{14}$  are the reflections for  $\text{ZrP}_2\text{O}_7$ . One impurity phase was identified  $\text{YbP}_3\text{O}_9$ ; its peaks denoted by \*. An unidentified peak at 84.5 two-theta ( $^\circ$ ) is indicated by ^. 138
- Figure 4.10: Room temperature lattice constants versus average ionic radii for  $\text{M}^{\text{III}}\text{M}^{\text{V}}$ -pyrophosphate compounds. Most compounds cluster around the linear fit to the data (equation at top of plot). Error bars are included. 142
- Figure 4.11: Plot of average linear CTE versus average ionic radius for  $\text{M}^{\text{III}}\text{M}^{\text{V}}$ -pyrophosphates in the temperature range 600-900 $^\circ\text{C}$ . Error bars are included. 143
- Figure 4.12: Instantaneous CTE versus temperature for  $\text{M}^{\text{III}}\text{M}^{\text{V}}$ -pyrophosphates. 143
- Figure 4.13: (a) – (e) Lattice constant versus temperature plots with quadratic fits to curves. (a)  $\text{AlNbP}_4\text{O}_{14}$ ; (b)  $\text{GaNbP}_4\text{O}_{14}$ ; (c)  $\text{InNbP}_4\text{O}_{14}$ ; (d)  $\text{YbNbP}_4\text{O}_{14}$ ; and (e)  $\text{BiTaP}_4\text{O}_{14}$ . Error bars are not included for clarity. 144
- Figure 4.14: ED pattern of  $\text{AlNbP}_4\text{O}_{14}$  showing some reflections indexed on the subcell and weak supercell reflections indicated by the arrows. Weak reflections are in pairs horizontally and vertically across the pattern between the strong reflections. 145
- Figure 4.15: ED pattern of  $\text{AlNbP}_4\text{O}_{14}$  from the same crystallite shown in Figure 4.14. Weak superlattice reflections are apparent. 146

## LIST OF EQUATIONS, RELATIONSHIPS, AND SCHEMES

### CHAPTER 1

(1)	Volume CTE, $\beta$	4
(2)	Maxwell relationship applied to $\beta$	4
(3)	$\beta$ at constant volume expressed as elastic response to thermal stress	5
(4)	Thermal pressure coefficient at constant volume	5
(5)	Grüneisen relationship defined for $\beta$	5
(6)	Grüneisen parameter and energy efficiency in pressure changes	6
(7)	Grüneisen thermodynamic parameter	6
(8)	Average Grüneisen parameter	6
(9)	Instantaneous linear CTE	7
(10)	Average linear CTE	7

### CHAPTER 2

(1)	Diffraction described by Bragg's law	36
(2)	Minimum wavelength of continuous radiation	38
(3)	Fractional decrease in intensity	38
(4)	Intensity of incident beam traveling distance $x$	39
(5)	Intensity relationship to mass absorption coefficient	39
(6)	Pressure relationship to ruby fluorescence emission	49
(7)	Bulk modulus, $B_0$	50
(8)	Wavelength of electron beam	51
(9)	Camera constant	51

## CHAPTER 3

(1)	Organic route in hydrolytic sol-gel synthesis	63
(2)	Hydroxylation producing metal alkoxide hydroxide	64
(3)	Hydroxylation involving alcohols and metal halides	64
(4)	Aprotic condensation between metal halide and metal alkoxide	65
(5)	Possible two-step process in aprotic condensation using ether as oxygen donor with metal halide	65
(6)	Idealized reaction in non-hydrolytic sol-gel synthesis of $\text{ZrP}_2\text{O}$	67
(7)	Dehydration and chemical changes in precursor $\text{Ce}(\text{HPO}_4)_2 \cdot 2.32\text{H}_2\text{O}$	104

## SUMMARY

This thesis examines the low temperature syntheses, characterization, and both thermophysical and high pressure properties of some low positive and negative thermal expansion (NTE) materials. It contributes to knowledge on the use of low temperature methods, such as hydrolytic sol-gel, non-hydrolytic sol-gel, and mild autoclave techniques, and provides evidence for the limits of some methods and the potential for the use of others. Diffraction, thermal expansion and high pressure studies provide new information regarding structures, thermal behavior, and pressure-induced phase transitions for some low positive and NTE materials.

Chapter 3 presents work on  $\text{ZrP}_2\text{O}_7$ ,  $\text{ZrV}_2\text{O}_7$ ,  $\text{CeP}_2\text{O}_7$ , and  $\text{PbP}_2\text{O}_7$ . Low temperature synthesis techniques proved successful for some compounds resulting in their inclusion into categories of materials, previously unreported, that can be produced using these methods. Characterization of materials, using lab and high resolution synchrotron powder XRD, led to the assignment of a new symmetry for  $\text{CeP}_2\text{O}_7$ . Studies using *in situ* high temperature lab and synchrotron powder XRD for  $\text{CeP}_2\text{O}_7$  and  $\text{PbP}_2\text{O}_7$  revealed their thermal properties for the first time, and facilitated a comparison of their behavior to those of other  $\text{A}^{\text{IV}}\text{M}^{\text{V}}_2\text{O}_7$ . High pressure diffraction measurements on  $\text{CeP}_2\text{O}_7$  provide data for the estimation of bulk moduli and suggests two possible pressure-induced phase transitions, properties previously unreported in the literature.

In Chapter 4, some  $\text{M}^{\text{III}}\text{M}'^{\text{V}}\text{P}_4\text{O}_{14}$  are examined. Low temperature hydrolytic sol-gel methods enabled the preparation of several new compounds in the  $\text{M}^{\text{III}}\text{M}'^{\text{V}}\text{P}_4\text{O}_{14}$  family. The impact of a broad range of  $\text{M}^{\text{III}}\text{M}'^{\text{V}}$  cation sizes substituted into the

pyrophosphate structure is examined using *in situ* high temperature powder diffraction.

These data suggest  $\text{AlNbP}_4\text{O}_{14}$ ,  $\text{InNbP}_4\text{O}_{14}$ , and  $\text{BiTaP}_4\text{O}_{14}$ , show a phase transition

between room temperature and  $900^\circ\text{C}$ .

# CHAPTER 1

## INTRODUCTION

### 1.1 Thermal Expansion

Thermal expansion is a necessary consideration in a number of applications where increases and decreases in temperatures can affect physical dimensions, stability, integrity, and mechanical properties of materials. Dimensional stability is necessary for positioning in precision optics, such as mirrors in telescopes or waveguides for use in telecommunications. Thermal shock resistance is often poor in materials with large thermal expansion coefficients, while manufacturers must also consider the mutual expansion and contraction of components as temperature changes.<sup>1,2</sup>

The stability and integrity of materials subjected to high temperatures or large temperature fluctuations is a problem related to their thermal expansion properties. Microcracking can occur in materials where expansion is anisotropic and it can lead to a degradation of properties. However, microcracking is used as an advantage in some materials where it leads to an increase in thermal shock resistance. Isotropic thermal expansion materials, those that expand or contract equally along all three axes, are desirable when faced with some of the problems with anisotropic materials.<sup>2-4</sup>

Frameworks made up of strong bonds that expand little and are of low density, so there is room for internal expansion or contraction, are the types of materials that are the subject of the current research.

Materials expand when heated due to the anharmonicity of the potential energy function. Figure 1.1 shows the asymmetry of the pair potential for two bonded atoms.

With an increase of temperature from  $T_1$  to  $T_2$ , the mean distance between the two atoms

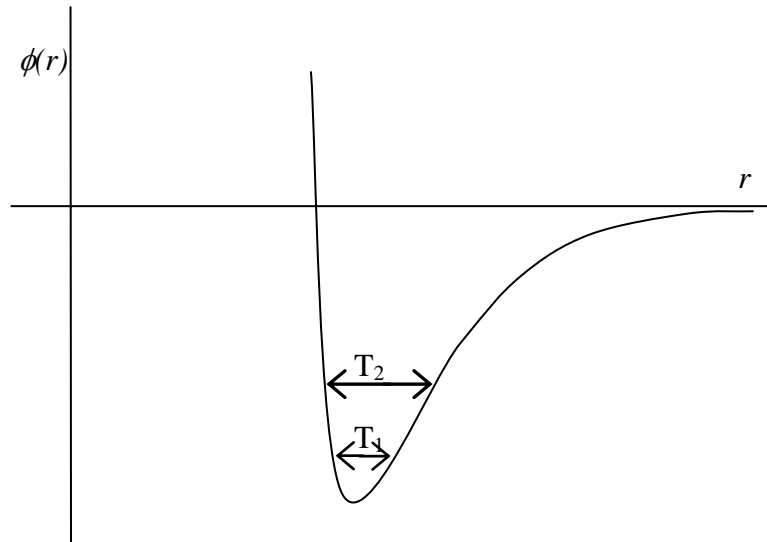


Figure 1.1: Graphic representation of anharmonic pair potential,  $\phi$ , as a function of interatomic distance,  $r$ , showing vibration at two different temperatures ( $T_2 > T_1$ ), demonstrating positive thermal expansion. Modified from Barrera, et al.; *J. Physics: Condens. Matter*.

increases.<sup>5</sup> Strong bonds, with generally shorter average interatomic bond distances, typically exhibit a more harmonic interatomic potential function, deepening the potential well and accessing more symmetric vibrational modes, Figure 1.2.<sup>4</sup>

Thermal expansion in solids cannot be fully appreciated by only considering the lengthening of bonds. While different bond lengths and bond strengths affect the extent of thermal expansion,<sup>1</sup> the impact on the thermal behavior of a three-dimensional structure necessitates additional considerations.

In framework solids, all lattice vibrational (phonon) modes must be considered.

While some vibrational modes can lead to an increase in unit cell size, other vibrational modes can result in a decrease. In addition, different vibrational modes are excited at different temperatures. Thermal expansion, therefore, depends upon the energies of

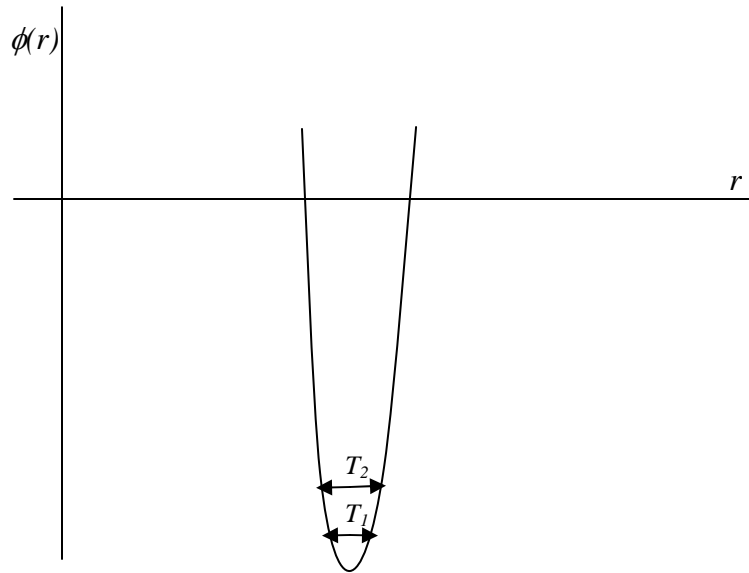


Figure 1.2: Graphic representation of harmonic pair potential,  $\phi$ , as a function of interatomic distance,  $r$ , showing vibration at two different temperatures ( $T_2 > T_1$ ), where the mean distance does not change with temperature.

various vibrational modes present in the three-dimensional structure, the impact of each mode on unit cell dimensions, and on temperature.<sup>2, 5</sup>

Thermal expansion in materials is often expressed using the volume coefficient of thermal expansion (CTE).<sup>3</sup> The volume CTE,  $\beta$ , is defined with the following relationship:<sup>5</sup>

$$\beta = \frac{\partial(\ln V)}{\partial T} = \left( \frac{1}{V} \frac{\partial V}{\partial T} \right)_P, \quad (1)$$

where V is volume and T is temperature at constant pressure, P. Thermal expansion is always in the direction of increasing entropy and this can be expressed by applying a Maxwell relation to equation (1) as follows:

$$\beta = \frac{1}{V} \left( \frac{\partial V}{\partial T} \right)_P = -\frac{1}{V} \left( \frac{\partial S}{\partial P} \right)_T = \chi_T \left( \frac{\partial S}{\partial V} \right)_T, \quad (2)$$

where S is entropy and  $\chi_T$  is the isothermal compressibility,  $-(\partial V / \partial P)_T / V$ , which is always positive and signifies the change in volume with increasing temperature is always in the direction of increasing disorder. The sign of  $\beta$  is related to that of  $(\partial S / \partial V)_T$ . A positive sign for  $\beta$  shows increasing entropy with increasing volume; a negative sign for  $\beta$  denotes increasing disorder when the volume decreases at constant temperature. As pressure increases and volume decreases under non-isothermal conditions, entropy decreases in materials exhibiting normal thermal expansion and  $\beta$  is positive in these compounds. NTE is anomalous in this limited scope as materials with NTE show increasing entropy with decreasing volume. For a quantum or ideal gas,  $\beta$  is always positive, so NTE is considered to be result of particle interaction. An example of this type of particle interaction is the NTE of liquid water below 4 °C, where, due to breaking of hydrogen bonds, there is an increase in entropy upon compression. At these low

temperatures, this interaction compensates for any tendency toward decreasing disorder.<sup>3,</sup>

5

At constant volume,  $\beta$  can be expressed as the following:

$$\beta = \chi_T \left( \frac{\partial P}{\partial T} \right)_V = \left( \frac{\partial P}{\partial T} \right)_V \left( \frac{-\partial \ln V}{\partial P} \right)_T, \quad (3)$$

which is thermal expansion expressed as the elastic response to thermal stress. There is a change in pressure as temperature increases at constant volume and then a change in volume at higher temperature at the initial pressure. As temperature approaches zero, compressibility approaches a finite limit and  $\beta$  has a temperature dependence related to the thermal pressure coefficient,  $(\partial P / \partial T)_V$ .

The thermal pressure coefficient can be expressed in terms of heat capacity per unit volume,  $C_v/V$ , and the Grüneisen parameter,  $\gamma$ , and takes into consideration those materials where the volume CTE,  $\beta$ , and  $C_v$ , have the same or similar temperature dependence. Thus,

$$\left( \frac{\partial P}{\partial T} \right)_V = \left( \frac{C_v}{V} \right) \gamma, \quad (4)$$

and the following Grüneisen relationship is defined for volume CTE,  $\beta$ :

$$\beta(T) = \frac{\gamma K_0 C_v}{V_0}, \quad (5)$$

where  $K_0$  is isothermal compressibility and  $V_0$  is the molar volume at 0K.  $C_v/V_0$  determines the amount of energy the material gains as temperature increases and  $\gamma$  determines energy effectiveness in changing the pressure:<sup>3, 5</sup>

$$\gamma = \left( \frac{\partial P}{\partial(U/V)} \right)_v = - \left( \frac{\partial \ln T}{\partial \ln V} \right)_s, \quad (6)$$

where  $U$  is the internal energy.

The Grüneisen thermodynamic parameter,  $\gamma$ , represents the anharmonicity of a crystal potential and is defined as:

$$\gamma = \frac{-d(\ln \nu)}{d(\ln V)}, \quad (7)$$

where  $\nu$  is the frequency of the vibrational mode and  $V$  is the volume. Vibrational modes which have a decrease in frequency as volume decreases will have a negative Grüneisen value.<sup>6</sup> In complex materials, the population of all vibrational modes at a given temperature must be considered giving the following relationship

$$\gamma_{av} = \frac{\sum c_i \gamma_i}{\sum c_i}, \quad (8)$$

where  $c_i$  is the weight of the contribution of a mode to the overall specific heat,  $C_v$ , at

constant volume. Due to the large temperature dependence of  $C_v$ , a generalization associated with the Grüneisen function (equation (5)) is that compounds with strong bonds will have lower CTE values.<sup>1</sup> An empirical proposition that bond expansion is inversely proportional to the square of bond strength, however, does not hold experimentally for all compounds. In complex frameworks, with corner-, edge-, or face-sharing polyhedra, linkages and polyhedral rotation of the network are determining factors in bulk thermal expansion.

The instantaneous linear CTE,  $\alpha$ , is how most thermal expansion measurements are defined.  $\alpha$  replaces  $\beta$  and  $L$  (length) replaces  $V$  (volume) in equation (1) giving the following relationship:<sup>5</sup>

$$\alpha = \frac{\partial(\ln L)}{\partial T} = \frac{1}{L} \frac{\partial L}{\partial T}, \quad (9)$$

where  $L$  is the length. In non-cubic crystals, where lattice constants  $a$ ,  $b$ , and  $c$  are not necessarily equivalent,  $\alpha$  is directional. The average linear CTE is defined as follows:

$$\alpha_{avg} = \frac{(L - L_0)}{L_0(T - T_0)}, \quad (10)$$

where  $L$  and  $L_0$  are the maximum and minimum lengths observed, and  $T$  and  $T_0$  are the maximum and minimum temperatures observed, respectively.<sup>1,3</sup>  $\alpha_{avg}$  is the normalized slope of a lattice constant vs. temperature curve. The length,  $L$ , can be the length of bulk materials found using dilatometry or the lattice constants of the unit cell that can be found

using X-ray diffraction techniques. When reporting CTE values,  $\alpha$  or  $\beta$ , the range of temperatures over which the CTE value was measured must be cited. Materials are often grouped into categories depending upon their CTE values (see Figure 1.3). Negative thermal expansion compounds are also categorized in this manner.

	<u>CTE (ppm K<sup>-1</sup>)</u>
High Expansion	$\alpha > 8.0$
Intermediate Expansion	$2.0 < \alpha < 8.0$
Low Expansion	$\alpha < 2.0$

Figure 1.3: Categories of materials based on CTE.

### ***1.1.1 Low or Negative Thermal Expansion (NTE) in Open Framework Materials***

Open framework materials are low density three-dimensional networks of linked polyhedra. Low or NTE behavior is observed in some compounds in which  $\text{MO}_6$  octahedra are linked to  $\text{MO}_4$  tetrahedra, for example. All lattice (phonon) vibrational modes must be considered and can result in overall positive or negative  $\alpha$ ,  $\beta$ , or Grüneisen,  $\gamma$ , values. A cubic material, where lattice constants  $a = b = c$ , will have a unit cell that contracts or expands isotropically. A non-cubic material, on the other hand, can display anisotropic thermal expansion having the overall effect of low or negative volume thermal expansion.<sup>1</sup>

One cause of low or NTE in open framework materials is transverse oxygen vibrational modes. In Figure 1.4, the image on the right depicts local transverse oxygen (open circle) vibrations between two metals (gray circles) where the oxygen is 2-coordinate. As the oxygen in the M-O-M (metal-oxygen-metal) linkage vibrates transversely rather than longitudinally (far left diagram) due to increasing temperature, the distance between the metals bonded to the oxygen decreases, assuming there is negligible expansion of the M-O bond. Lattice modes involving transverse motion are often lower in energy than those involving bond elongations and can be excited at lower

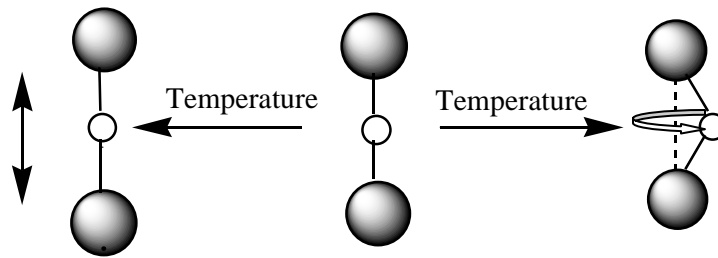


Figure 1.4: Drawing depicts M-O-M linkages (metals shown as gray circles; oxygen atoms are open circles) and affect of longitudinal (left) and transverse (right) oxygen atom vibrations on M-M distance. Modified from Evans, Mary, and Sleight, *Physica B* 241-243, 311 (1998).

temperatures, thus playing a major roll in the overall Grüneisen parameter (Section 1.1, equation (5)) and possibly leading to low temperature NTE or low positive thermal expansion. The impact of transverse oxygen vibrations in a three-dimensional open framework on the CTE can depend on the rigidity of the  $\text{MO}_6$  and  $\text{MO}_4$  polyhedra as well as the strength of M-O-M bonds linking them.<sup>3</sup>

Rigid unit modes (RUMs) are low energy phonon modes associated with some rigid framework materials and represent another way of describing transverse oxygen

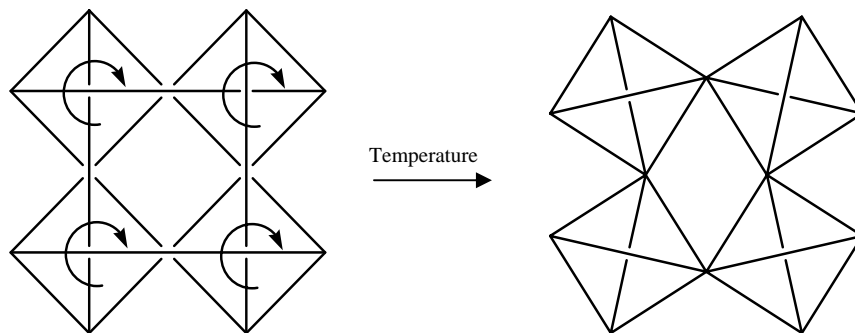


Figure 1.5: Left, two-dimension representation of rigid corner-sharing polyhedra; right, the reduction of volume as temperature increases. The individual polyhedra show no distortion with increasing temperature. Modified from Evans; *J. Chem. Soc.; Dalton Transactions*, 1999.<sup>3</sup>

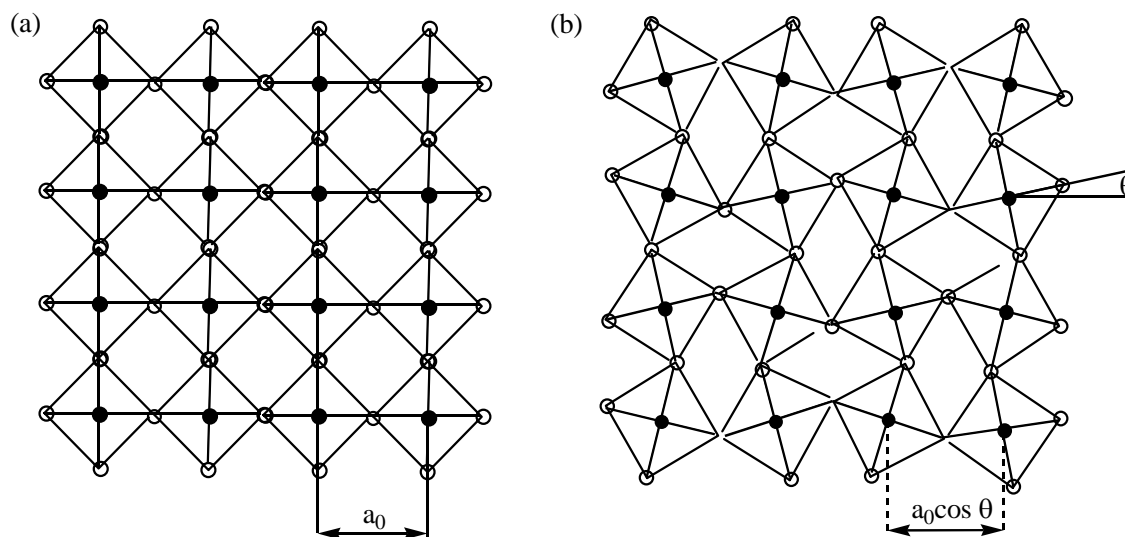


Figure 1.6: (a) A square lattice of rigid  $\text{MO}_4$  units; M filled circles, O open circles. (b) Rotational displacements in the lattice shown in (a) illustrating effect of a RUM in the lattice with a bent M-O-M angle  $\pi - 2\theta$ . Modified from Barrera, et al.; *J. Phys.: Condens. Matter*.<sup>5</sup>

vibrations that takes into account the whole crystal. Corner-sharing polyhedra with strong M-O bonds and relatively short O-O bonds prevent distortion of individual polyhedra, but the M-O-M links are relatively easy to bend. Rocking motions of the polyhedra lead to transverse oxygen motion in the M-O-M bonds and coupled rotation of polyhedra; the result is a reduction of volume as the structure folds up upon itself without distortion of the polyhedra.<sup>3-5</sup> Figure 1.4 represents rigid corner-sharing polyhedra with flexible M-O-M links and the impact of increasing temperature due to RUMs.

Figure 1.5 shows a graphical example of a rigid framework (a) of  $\text{MO}_4$  units and (b) after propagation of a representative RUM through it along with a resulting bent M-O-M angle. The rigid  $\text{MO}_4$  units are joined to one another through oxygen in (a). In (b), the units dynamically rotate in different directions reducing the internal volume of the framework.

A mathematical model that calculates whether or not RUMs are allowed in specific structures has been developed that is not dependent on a specific temperature range. Use of the model has led to some interesting knowledge concerning NTE framework materials. It has been determined that the predicted existence of RUMs in compounds is not always a reliable indicator of NTE, but that there is an apparent relationship between the existence of RUMs and NTE in some materials.<sup>7</sup> Studies using the model have found RUMs in materials that exhibit NTE after a temperature-induced phase transition and which disappear below the phase transition temperature along with NTE.  $\text{NbPO}_5$  and  $\text{TaPO}_5$ , have been examined and support this RUM model. Each structure is tetragonal in the high temperature phase exhibiting NTE and in the low temperature phase, which exhibits no NTE. Some of the members of the  $\text{MO}_2$  family of

aluminophosphates and silicates ( $\text{SiO}_4$  or  $\text{AlO}_4$  and  $\text{PO}_4$  tetrahedra) consist of very rigid frameworks all found to possess RUMs and large NTE coefficients of thermal expansion.

Other compounds, however, show a temperature-induced phase transition and NTE above the transition temperature, but there are no RUMs either above or below the temperature of phase transition. The  $\text{A}^{\text{IV}}\text{M}^{\text{V}}_2\text{O}_7$  (Section 1.2) and  $\text{A}^{\text{III}}_2\text{MO}_3\text{O}_{12}$  (Section 1.3.2) families are examples of compounds containing no RUMS, but which contain other low energy phonon modes.  $\text{A}^{\text{IV}}\text{M}^{\text{VI}}_2\text{O}_8$  compounds (Section 1.3.1), on the other hand, are dissimilar in structure to  $\text{A}^{\text{IV}}\text{M}^{\text{V}}_2\text{O}_7$  materials in that there are tetrahedra with one corner linkage unattached. These compounds are considered underconstrained, contain many RUMs, and exhibit varying degrees of negative thermal expansion over large temperature ranges.<sup>3, 7-10</sup>

Quasi-rigid unit modes (qRUMs)<sup>3, 5, 7, 11</sup> are similar to RUMs but involve some distortion of polyhedra and have higher energy. QRUMs are thought to contribute to a variety of thermal expansion behavior including high positive and intermediate positive TE or high positive and NTE in some individual compounds. In these structures, the size of the cation in  $\text{MO}_6$  octahedra and  $\text{MO}_4$  tetrahedra facilitate polyhedra distortion upon heating. Several members of the  $\text{A}^{\text{IV}}\text{M}_2\text{O}_7$  family of compounds (Section 1.2) have been reported to contain qRUMs as a contributor to low positive or NTE and contain no RUMs.<sup>4, 7, 12, 13</sup>

NTE has also been observed in some ferroelectric compounds, where a ferroelectric-paraelectric phase transition upon heating can overcome normal positive expansion leading to volume contraction over narrow temperature ranges.<sup>3, 4, 14</sup>  $\text{PbTiO}_3$  is

an example. At room temperature, the structure is tetragonal with distorted  $\text{TiO}_6$  octahedra with average Ti-O bonds of 1.766 Å, 4 x 1.979 Å, 1 x 2.390 Å, and an average bond length of 2.012 Å. As the temperature increases, the octahedra become regular as the ferroelectric-paraelectric phase transition temperature, 490 °C, is approached. Above the temperature of phase transition,  $\text{PbTiO}_3$  is cubic. Positive thermal expansion occurs along the  $a$  and  $b$  axes in the tetragonal phase, while contraction occurs along the  $c$  axis. This contraction is enough to result in volume decrease for the structure. Figure 1.6 shows how the cell edges and volume change with increasing temperature for  $\text{PbTiO}_3$ . Note the volume contraction is limited to a narrow range around the phase transition temperature. The rationale for this behavior is that while the  $\text{TiO}_6$  octahedra become more regular, there is a decrease in anion-anion repulsion, and it is this decrease in repulsion that results in

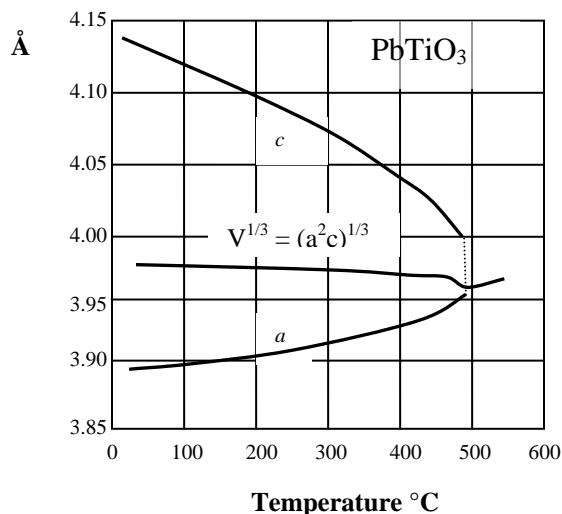


Figure 1.7: Changes of cell edges,  $a$  and  $c$ , and volume for  $\text{PbTiO}_3$  with increasing  $T$ . Cell volume reaches minimum close to 490°C. Modified from Sleight; *Inorg. Chem.* <sup>4</sup>

smaller bond distances and, therefore, smaller polyhedra volume.

Some ferromagnetic compounds have also been shown to exhibit low positive and/or NTE within narrow temperature ranges due to magnetostriction. Examples of this type of thermal behavior are found in the Fe-Ni alloy, Invar (Section 1.3.9), and other intermetallic compounds. The thermal expansion behavior of these compounds is normal and positive, but large contractions are found near their Curie temperatures resulting from the absorption of thermal energy as magnetic domains disappear; very low and in some cases both low positive and NTE is observed. Above the Curie temperature, thermal motion dominates and can overcome the forces responsible for magnetic alignment.<sup>1,3</sup>

### ***1.1.2 Methods to Control Thermal Expansion***

One method to control thermal expansion is the production of composites with a negative thermal expansion material offsetting the positive thermal expansion in another material.<sup>3</sup> Alternatively, CTEs of one-phase materials can be tuned through framework stuffing and cation substitution.

Framework stuffing consists of introducing additional ions into void spaces in polyhedral frameworks. Examples include the stuffed derivative of quartz,  $\beta$ -spodumene, and a stuffed derivative of keatite (a polymorph of silica),  $\beta$ -eucryptite. These materials belong to the LAS system,  $\text{Li}_2\text{O}-\text{Al}_2\text{O}_3-\text{SiO}_2$ . Some of the Si in the parent framework is replaced by Al and charge balanced with Li ions stuffed into interstices of the quartz or keatite framework. Normally,  $\alpha$ -quartz has a very large CTE,  $400 \pm 50 \times 10^{-6}\text{K}^{-1}$  across the [100] plane, and  $140 \pm 30 \times 10^{-6}\text{K}^{-1}$  across the [101] plane in the temperature range from 22°C to 1400°C, but replacing some Si with Al and stuffing the framework with Li

ions stabilizes the  $\beta$ -quartz and keatite structures, reducing the CTE to  $0.9 \times 10^{-6} \text{K}^{-1}$  in  $\beta$ -spodumene ( $\text{LiO}_2:\text{Al}_2\text{O}_3:\text{SiO}_2$  ratio 1:1:4) and to  $-6.2 \times 10^{-6} \text{K}^{-1}$  in  $\beta$ -eucryptite ( $\text{LiO}_2:\text{Al}_2\text{O}_3:\text{SiO}_2$  ratio 1:1:2) in the temperature range from  $25^\circ\text{C}$  to  $1000^\circ\text{C}$ .<sup>1, 15</sup>

Cation substitution, on the other hand, is where metals of different ionic radii and/or a variety of valence states are substituted for a metal ion in a compound.<sup>16</sup> For example, substitution of  $\text{Zr}^{\text{IV}}$  with  $\text{M}^{\text{III}}\text{M}^{\text{V}}$  in  $\text{ZrP}_2\text{O}_7$  can suppress the temperature-induced phase transition observed for the parent material (Sections 1.2 and 1.2.4; Chapter 4).<sup>17</sup> Solid solutions (Section 1.2.3) can also be used to tune CTE's.<sup>18</sup>

## 1.2 The $\text{A}^{\text{IV}}\text{M}^{\text{V}}_2\text{O}_7$ Family of Compounds

One of the most interesting families of low and negative thermal expansion compounds comprises  $\text{A}^{\text{IV}}\text{M}^{\text{V}}_2\text{O}_7$  materials. Members of this family, as well as related solid solutions, usually have cubic structures ( $\text{Pa}\bar{3}$  space group) at high temperature, exhibiting isotropic thermal expansion, and are isostructural with the high temperature (HT) form of  $\text{ZrP}_2\text{O}_7$ . Some members of this family serve as the basis for the research presented in this thesis.

For pyrophosphates, the  $\text{A}^{\text{IV}}$  cation includes Zr, Ti, Mo, Re, W, Th, U, Pu, Ce, Hf, Pb, Sn, Ge, and Si;  $\text{M}^{\text{V}} = \text{P}, \text{V}, \text{or As}$ .<sup>18-22</sup> Pyrovanadate compounds ( $\text{M}^{\text{V}} = \text{V}$ ) have only been prepared for  $\text{Zr}^{4+}$  or  $\text{Hf}^{4+}$ , while pyroarsenates ( $\text{M}^{\text{V}} = \text{As}$ ) have been prepared with  $\text{Zr}^{4+}$  and  $\text{Th}^{4+}$ .<sup>18, 23, 24</sup>

The structures of all  $\text{A}^{\text{IV}}\text{M}^{\text{V}}_2\text{O}_7$  compounds are related to that of the parent compound, the HT form of  $\text{ZrP}_2\text{O}_7$ . It is based on corner sharing  $\text{ZrO}_6$  octahedra and  $\text{PO}_4$  tetrahedra in a flexible, open framework. Each octahedron is connected through its

corners to six tetrahedra and each tetrahedron is connected to three octahedra and one other tetrahedron (see Figure 1.7). The structure closely resembles that of NaCl, but of lower symmetry due to the substitution of  $M^V_2O_7^{4-}$  units for  $Cl^-$  in the NaCl structure.<sup>2, 18</sup>

A low temperature (LT) form of  $ZrP_2O_7$  also exists. It was described in a 1996 work as a  $3a \times 3a \times 3a$  cubic (space group  $P a \bar{3}$ ) superlattice and more recently as an orthorhombic superlattice, (space group  $Pbca$ ).<sup>12, 21, 22</sup> Most of the P-O-P bonds are bent away from  $180^\circ$ , which is thermodynamically more favorable than  $180^\circ$ . As temperature increases, the LT phase transforms to the HT structure; the P-O-P angles average  $180^\circ$ .

Other  $A^{IV}M^V_2O_7$  compounds have been reported in the literature to have low

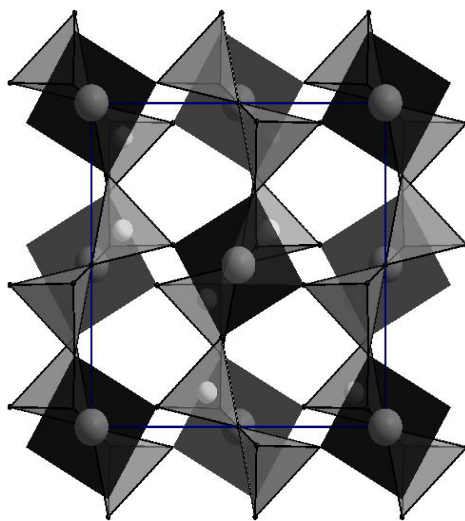


Figure 1.8: Structure of cubic  $A^{IV}M_2O_7$  family consisting of  $A^{IV}O_6$  octahedra (dark) and  $MO_4$  tetrahedra (light) in a corner-sharing arrangement.

temperature superstructures:  $\text{ZrV}_2\text{O}_7$ ,<sup>25</sup>  $\text{HfV}_2\text{O}_7$ ,<sup>26</sup>  $\text{SiP}_2\text{O}_7$ ,<sup>27</sup>  $\text{GeP}_2\text{O}_7$ ,<sup>20, 28, 29</sup>  $\text{TiP}_2\text{O}_7$ ,<sup>30-32</sup>  
 $\text{CeP}_2\text{O}_7$ ,<sup>33</sup> and  $\text{SnP}_2\text{O}_7$ .<sup>34, 35</sup>

### 1.2.1 Properties of $A^{\text{IV}}$ Pyrophosphates and $A^{\text{IV}}$ Pyrovanadates

$A^{\text{IV}}\text{M}^{\text{V}}_2\text{O}_7$  compounds have been topics for study due to interesting structural and thermal properties. Heating  $\text{ZrP}_2\text{O}_7$ , for example, results in a phase transition at around 290 °C; the structure changes from the LT superstructure to the HT simple cubic structure. Zirconium pyrophosphate exhibits high positive thermal expansion ( $\alpha_{\text{avg}} = 12.4 \times 10^{-6}\text{K}^{-1}$ ) up to the temperature of phase transition (290 °C), an incommensurate form is present in a narrow temperature range,<sup>12, 36</sup> and at high temperatures intermediate positive thermal expansion  $\alpha = 5.4 \times 10^{-6}\text{K}^{-1}$  (600-700K) is observed.<sup>3</sup>

$\text{ZrV}_2\text{O}_7$  exhibits two phase transitions at approximately 77°C and 102°C, changing from a  $(3a \times 3a \times 3a)$  superstructure to an incommensurate form at the lower phase transition temperature and finally to a simple cubic HT form.  $\text{ZrV}_2\text{O}_7$  exhibits positive thermal expansion up to around 102°C and then negative thermal expansion up to about 800°C, with degradation of the compound around this temperature.<sup>37, 38</sup>

Several other pyrophosphate compounds exhibit unusual thermal expansion.  $\text{UP}_2\text{O}_7$  exhibits both positive and NTE, intermediate thermal expansion up to 400°C with a CTE of  $\alpha_{\text{avg}} = 4.9 \times 10^{-6} \text{K}^{-1}$  and NTE from 400°C up to 1200°C,  $\alpha_{\text{avg}} = -3.7 \times 10^{-6} \text{K}^{-1}$ .<sup>39</sup>  $\text{ThP}_2\text{O}_7$  is another compound that exhibits both positive and NTE, but the transition from positive to negative expansion occurs around 150°C and NTE continues to temperatures greater than 850°C with a larger negative CTE than found for  $\text{UP}_2\text{O}_7$ .<sup>40</sup>

TiP<sub>2</sub>O<sub>7</sub>, on the other hand, was found to have a high positive thermal expansion coefficient by Harrison and Hummel in 1959 ( $\alpha_{\text{avg}} = 12.2 \times 10^{-6} \text{ K}^{-1}$ , 50 – 1000 °C) with no abrupt phase changes in the temperature range studied.<sup>41</sup> Both SnP<sub>2</sub>O<sub>7</sub><sup>42</sup> and GeP<sub>2</sub>O<sub>7</sub><sup>29</sup> also show nearly linear positive thermal expansion up to approximately 825°C and 970°C, respectively.

Published thermal data for all A<sup>IV</sup>M<sup>V</sup><sub>2</sub>O<sub>7</sub> compounds is incomplete. No published data on thermal expansion behavior have been found in the literature for A<sup>IV</sup> = Mo, Re, W, Pu, Pb, Hf, and Ce; M<sup>V</sup> = P.

Thermal expansion studies of some A<sup>IV</sup>-pyrophosphates suggest a tendency of increasing negative thermal expansion as the size of the A<sup>IV</sup> cation increases.<sup>2</sup> In Figure 1.9, thermal expansion data for some A<sup>IV</sup>-pyrophosphates and ZrV<sub>2</sub>O<sub>7</sub> are shown. The ionic radius of Ti, Zr, U, and Th are 0.605 Å, 0.72 Å, 0.89 Å, and 0.94 Å, respectively.<sup>43</sup> The thermal expansion curves become more negative as the tetravalent ionic radii increase for the pyrophosphates. An explanation for this tendency toward negative thermal expansion is that unit cell edges increase and the octahedra become larger, due to the larger central cation, making the polyhedra easier to distort.<sup>44</sup> For ZrV<sub>2</sub>O<sub>7</sub>, the unit cell edge increases when V replaces P, which causes NTE to become more pronounced in the material.

### ***1.2.2 Synthesis of A<sup>IV</sup> Pyrophosphates and A<sup>IV</sup> Pyrovanadates***

The preparation of A<sup>IV</sup>M<sup>V</sup><sub>2</sub>O<sub>7</sub> compounds has been dominated by standard solid state synthesis techniques. HfV<sub>2</sub>O<sub>7</sub><sup>26</sup>, ZrV<sub>2</sub>O<sub>7</sub><sup>45-48</sup>, ThP<sub>2</sub>O<sub>7</sub><sup>40</sup>, UP<sub>2</sub>O<sub>7</sub><sup>39</sup>, TiP<sub>2</sub>O<sub>7</sub><sup>32, 49</sup>, SnP<sub>2</sub>O<sub>7</sub><sup>42</sup>, ReP<sub>2</sub>O<sub>7</sub><sup>50</sup>, MoP<sub>2</sub>O<sub>7</sub><sup>51</sup>, and WP<sub>2</sub>O<sub>7</sub><sup>52</sup> have been prepared by these methods. The

process generally entails heating intimate mixtures of metal oxides often at high temperatures for several hours to several days. A representative example is the solid state synthesis of  $\text{WP}_2\text{O}_7$  using  $\text{WO}_3$ , W, and  $(\text{NH}_4)_2\text{HPO}_4$ , prepared at  $900^\circ\text{C}$  in an evacuated quartz tube for 4 to 6 days. In addition, sols have been prepared using metal oxides or metal chlorides and concentrated solutions of  $\text{H}_3\text{PO}_4$  or excess concentrations of other soluble phosphates to obtain  $\text{A}^{\text{IV}}$  pyrophosphates.  $\text{ZrP}_2\text{O}_7$ <sup>22, 53-55</sup>,  $\text{SiP}_2\text{O}_7$ <sup>56</sup>,  $\text{NbP}_2\text{O}_7$ <sup>19</sup>,  $\text{SnP}_2\text{O}_7$ <sup>35, 42</sup>, and  $\text{TiP}_2\text{O}_7$ <sup>41</sup> have been obtained upon subsequent heat treatments of the sols. Most of the compounds prepared using concentrated solutions of phosphoric acid often crystallize to the pyrophosphate at temperatures comparable to those obtained found using solid state methods. The exception is  $\text{ZrP}_2\text{O}_7$ , which has a crystallization temperature that has been reported to depend on the phosphate concentration, with slightly lower crystallization temperatures (around  $1000^\circ\text{C}$ ) found with increasing phosphoric acid concentration.<sup>55</sup>

$\text{CeP}_2\text{O}_7$  has been synthesized by heat treatment of the product from acid reflux of cerium sulfate hydrate in concentrated  $\text{H}_3\text{PO}_4$ ,<sup>57</sup> as well as other methods described in Section 3.5. Acid reflux methods have also been used in the preparation of  $\text{PuP}_2\text{O}_7$  with plutonium oxalate in concentrated  $\text{H}_3\text{PO}_4$ ,<sup>58</sup> and in the preparation of  $\text{PbP}_2\text{O}_7$  (Section 3.6) with lead (IV) acetate dissolved in hot glacial acetic acid, along with the addition of  $\text{H}_3\text{PO}_4$  and distilled water. Crystalline lead pyrophosphate is obtained after heating the precursor  $\text{Pb}(\text{HPO}_4)_2 \cdot \text{H}_2\text{O}$  to around  $300^\circ\text{C}$ .

Direct precipitation from aqueous solutions of hafnium and vanadium oxalates and subsequent thermal decomposition of the precipitates, at approximately  $700^\circ\text{C}$ , has been reported for  $\text{HfV}_2\text{O}_7$ <sup>59</sup>. Thermal treatment (between  $260^\circ\text{C}$  and  $270^\circ\text{C}$  or above

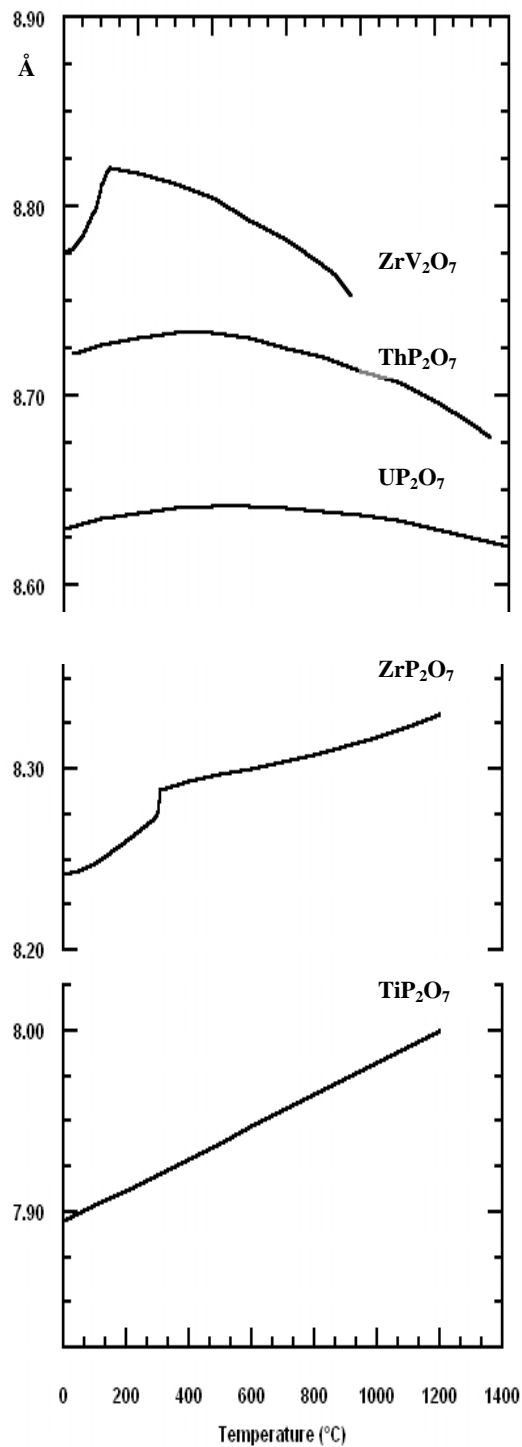


Figure 1.9: Compilation plots of lattice constant (Å) vs. temperature for some  $A^{IV}M^V_2O_7$  compounds. Modified from Sleight; *Inorg. Chem.*<sup>4</sup>

350°C) of precipitates from an aqueous solution of zirconium oxynitrate and ammonium vanadium oxide results in  $\text{ZrV}_2\text{O}_7$ <sup>45, 48</sup>.

Mild hydrothermal synthesis techniques have been used recently in the preparation of  $\alpha\text{-GeP}_2\text{O}_7$ . In this synthesis,  $\text{GeO}_2$  and concentrated  $\text{H}_3\text{PO}_4$  are autoclaved to produce the dihydrogen phosphate precursor,  $\alpha\text{-Ge}(\text{HPO}_4)_2 \cdot \text{H}_2\text{O}$ . With subsequent heat treatment at 800°C, crystalline  $\alpha\text{-GeP}_2\text{O}_7$  is obtained. Notable in this study is that the temperature required to produce  $\alpha\text{-GeP}_2\text{O}_7$  is 300°C lower than that reported for solid state synthesis of  $\text{GeP}_2\text{O}_7$  (1100 °C).<sup>28, 29</sup>  $\text{ZrP}_2\text{O}_7$  has been achieved using an autoclave and ZrP amorphous sol (from  $\text{ZrCl}_4$ ) and concentrated  $\text{H}_3\text{PO}_4$  (greater than 14.5M) after crystallization of the autoclaved product at 973°C (see Section 3.4). Autoclave time and temperature, as well as the concentration of phosphoric acid, are noted to affect the type of product obtained.<sup>60</sup>

### **1.2.3 Solid Solutions**

Solid solutions isostructural with  $\text{ZrP}_2\text{O}_7$  have been prepared for  $\text{ZrV}_{2-x}\text{P}_x\text{O}_7$  and  $\text{HfV}_{2-x}\text{P}_x\text{O}_7$  with essentially identical thermal expansion results.<sup>18</sup> The solid solution  $\text{ZrV}_{2-x}\text{P}_x\text{O}_7$  is of particular interest as the parent compounds,  $\text{ZrV}_2\text{O}_7$  and  $\text{ZrP}_2\text{O}_7$ , exhibit negative and low positive thermal expansion properties, respectively, and both crystallize and degrade at different temperatures. Both solid state and direct precipitation methods have been used to prepare  $\text{ZrV}_{2-x}\text{P}_x\text{O}_7$  (and  $\text{ZrHf}_{2-x}\text{P}_x\text{O}_7$ ). In a study by Korthuis, et al., various compositions in the solid solution  $\text{ZrV}_{2-x}\text{P}_x\text{O}_7$  were prepared. The phase transitions for  $\text{ZrV}_2\text{O}_7$  (Section 1.2.1 and Figure 1.8) are totally suppressed when  $x = 1.2$  for the solid solution, and positive thermal expansion is realized when  $x = 1.6$ .<sup>18</sup>

Other solid solutions prepared by solid state methods include  $Zr_xTh_{1-x}P_2O_7$  (starting materials:  $ThO_2$ ,  $2ZrO_2CO_2 \cdot xH_2O$ , and  $(NH_4)_2HPO_4$  heated at  $900^\circ C$ ).<sup>40, 61</sup> Ota and Yamai<sup>61</sup> reported the synthesis of the solid solution  $Ce_{1-x}Zr_xP_2O_7$  along with thermal expansion data for  $Ce_{0.2}Zr_{0.8}P_2O_7$ . Preparation of  $Ce_{1-x}Zr_xP_2O_7$  involved high temperature ( $1200^\circ C - 1500^\circ C$ ) treatments of sols prepared with  $ZrOCl_2 \cdot 8H_2O$ , substituting cerium oxide or carbonate, and concentrated solutions of  $H_3PO_4$ .

#### 1.2.4 The $M^{III}M^V P_4O_{14}$ Family – Structural Relatives of HT $ZrP_2O_7$

Compounds with  $ZrP_2O_7$ -type structures have been prepared by substitution of  $Zr^{IV}$  in  $ZrP_2O_7$  with  $M^{III}$  and  $M^V$  cations resulting in a general form  $M^{III}M^V P_4O_{14}$  (Chapter 4.). Their thermal expansion behavior is quite different from that observed for  $ZrP_2O_7$ .<sup>16, 17</sup> The abrupt temperature-induced order/disorder phase transition observed for  $ZrP_2O_7$  (Section 1.2.1 and Figure 1.8) is suppressed or eliminated in the temperature ranges reported in literature.

### 1.3 Other Families of Low or NTE Compounds

#### 1.3.1 $A^{IV}M^{VI}_2O_8$

$A^{IV}M^V_2O_7$  compounds are not the only family exhibiting interesting thermal properties or structure. The  $A^{IV}M^{VI}_2O_8$  family, where  $A^{IV} = Zr$  or  $Hf$ ;  $M^{VI} = W$  or  $Mo$ , exhibit strong isotropic negative thermal expansion over a wide range of temperatures.<sup>2, 10, 13, 62, 63</sup> Cubic  $\alpha$ - $ZrW_2O_8$ , for example, is structurally similar to  $ZrP_2O_7$  having the same symmetry at high temperature, and consists of linked  $ZrO_6$  octahedra and  $WO_4$  tetrahedra, but with two crystallographically distinct  $WO_4$  tetrahedra.<sup>2</sup> Cubic zirconium

tungstate (space group P2<sub>1</sub>3), prepared by solid state methods using ZrO<sub>2</sub> and WO<sub>3</sub> heated at 1200 °C for several days, is thermodynamically stable between 1105 °C and 1231 °C.<sup>10</sup>

Quenched cubic zirconium tungstate remains kinetically stable when heated up to approximately 600°C. In addition, a metastable trigonal phase of ZrW<sub>2</sub>O<sub>8</sub> was prepared by Wilkinson, et al., using non-hydrolytic sol-gel techniques with calcination around 750 °C.<sup>64</sup> Cubic ZrW<sub>2</sub>O<sub>8</sub> can be prepared at low temperature using aqueous solutions of precursor materials ZrOCl<sub>2</sub> · 8H<sub>2</sub>O and (NH<sub>4</sub>)<sub>6</sub>H<sub>2</sub>W<sub>12</sub>O<sub>40</sub> in which the precipitate is autoclaved and then heated at around 600 °C.<sup>65</sup>

### 1.3.2 $A^{III}_2M^{VI}_3O_{12}$ Family

Representative of the  $A^{III}_2M^{VI}_3O_{12}$  family of NTE materials is scandium tungstate, Sc<sub>2</sub>(WO<sub>4</sub>)<sub>3</sub>. Orthorhombic in structure, scandium tungstate consists of corner sharing ScO<sub>6</sub> octahedra and WO<sub>4</sub> tetrahedra. Neutron powder diffraction studies have shown scandium tungstate to exhibit anisotropic thermal expansion with *a* and *c* axes of the unit cell contracting and the *b* axis expanding upon heating over a wide range of temperatures. The overall affect is NTE between -263 °C and 177 °C ( $\alpha_v = -6.5 \times 10^{-6} \text{ K}^{-1}$ , where  $\alpha_v$  is the volume coefficient of thermal expansion; 50-450 K).<sup>3</sup> A wide variety of cations, from Al<sup>3+</sup> to Y<sup>3+</sup>, can be substituted on the Sc site. Such substitutions lead to positive, zero, and NTE behavior in the resulting compounds. Figure 1.10 shows examples of substituted compounds and their thermal expansion behavior. In<sub>2</sub>(WO<sub>4</sub>)<sub>3</sub> shows both

positive and negative thermal expansion, while  $\text{InAl}(\text{WO}_4)_3$  and  $\text{Al}_2(\text{WO}_4)_3$  exhibit zero and NTE, respectively.

Aliovalent doping in this family of compounds has led to the synthesis of  $\text{Zr}_2(\text{WO}_4)(\text{PO}_4)_2$ . Systems involving Zr/W/P/O, specifically  $2\text{ZrO}_2 \cdot \text{WO}_3 \cdot \text{P}_2\text{O}_5$ , were investigated by Martinek and Hummel in 1970 and prepared using solid state synthesis methods with heat treatments between 800 °C and 1500 °C.<sup>66</sup> Related to this study, Evans, et al., prepared  $\text{Zr}_2(\text{WO}_4)(\text{PO}_4)_2$ , space group Pnca, by solid state methods. Many of the compounds in this family exhibit orthorhombic (space group Pnca) to monoclinic (space group  $\text{P } 2_1/a$ ) phase transitions with decreasing temperature with the orthorhombic form containing two crystallographically distinct tetrahedral groups. The compound  $\text{Zr}_2(\text{WO}_4)(\text{PO}_4)_2$  was found to have  $\text{ZrO}_6$  octahedra in a corner-sharing arrangement with

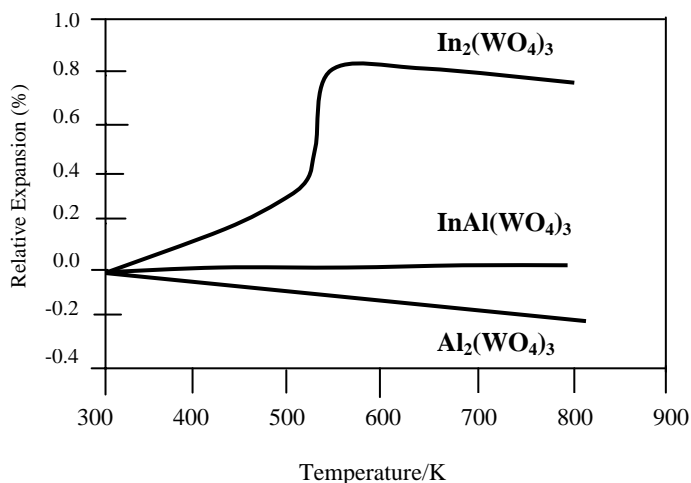


Figure 1.10: Percent relative expansion versus temperature for three solid solutions of the  $\text{A}^{\text{III}}_2\text{M}^{\text{VI}}_3\text{O}_{12}$  family. Modified from Evans; *J. Chem. Soc., Dalton Trans.*<sup>3</sup>

WO<sub>3</sub> and PO<sub>4</sub> tetrahedra, with one of the tetrahedral sites occupied by tungsten and the other by phosphorus.<sup>67</sup>

### 1.3.3 NZP (NASICON) Family

NZP compounds were discovered when researchers noted a strong decrease in positive thermal expansion with decreasing content of x in the NASICON compound Na<sub>1+x</sub>Zr<sub>2</sub>P<sub>3-x</sub>Si<sub>x</sub>O<sub>12</sub> (based on NaZr<sub>2</sub>(PO<sub>4</sub>)<sub>3</sub> structure). NZP and CTP, with general formulas NaZr<sub>2</sub>P<sub>3</sub>O<sub>12</sub> and CaTi<sub>4</sub>P<sub>6</sub>O<sub>24</sub>, respectively, have served as parent compounds for a wide range of ionic substitutions.<sup>1</sup> Partial or complete substitution affords tailoring of a desired characteristic, such as thermal expansion. NZP compounds are rhombohedral (R $\bar{3}c$  space group) with a three-dimensional framework of corner sharing PO<sub>4</sub> tetrahedra and (Zr/Ti)O<sub>6</sub> octahedra.

NZP materials in generally exhibit anisotropic expansion properties.<sup>1,3</sup> In R $\bar{3}c$ , *a* and *b* axes are always equal, but thermal behavior may involve the expansion of some axes and the contraction of others. Expansion anisotropy in some NZP materials can be eliminated by preparation of solid solutions of materials that show reverse lattice expansion behavior.

### 1.3.4 The A<sup>IV</sup><sub>2</sub>M<sup>V</sup><sub>2</sub>O<sub>9</sub> Family

Most work on the A<sup>IV</sup><sub>2</sub>M<sup>V</sup><sub>2</sub>O<sub>9</sub> family has been performed on zirconyl phosphate polymorphs.<sup>53,66,68</sup> The two polymorphs of zirconyl phosphate, the stable  $\alpha$ - form and the  $\beta$ - metastable form, have been prepared separately; however, it has been observed

that a  $\beta$ - to  $\alpha$ - irreversible transition occurs upon heating the  $\alpha$ -form at a temperature of 1150 °C. In 2003, Wallez, et al. synthesized a material interesting for its anisotropic ultralow thermal expansion properties.  $\beta$ -(Zr<sub>2</sub>O)(PO<sub>4</sub>)<sub>2</sub> is the phase achieved by heating  $\alpha$ -zirconyl phosphate at 1100°C. Anisotropy in the structure has been found to occur upon heating  $\beta$ -(Zr<sub>2</sub>O)(PO<sub>4</sub>)<sub>2</sub>, evidenced by strong shrinkage along the *b*-axis of the crystal unit cell, while the *a*- and *c*- axes expand, accounting for an overall ultralow thermal expansion.<sup>69</sup>

### 1.3.5 *Lithia-Alumina-Silica (LAS) Li<sub>2</sub>O-Al<sub>2</sub>O<sub>3</sub>-SiO<sub>2</sub>) Family*

The LAS family of compounds includes thermal shock-resistant ceramics, which are used in the production of dinnerware, aircraft glazing, laboratory bench tops, and mirror blanks for telescopes.<sup>1</sup> Compounds in this family comprise ultralow and negative thermal expansion materials with unique characteristics based on spodumene and eucryptite structures, respectively.  $\beta$ -spodumene (LiAlSi<sub>2</sub>O<sub>6</sub>) and  $\beta$ -eucryptite (LiAlSiO<sub>4</sub>), developed by F. A. Hummel, are derivatives of the  $\beta$ -quartz and keatite structures, respectively, where some of the Si<sup>4+</sup> ions are replaced by Al<sup>3+</sup> ions with charge balance coming from stuffed Li<sup>+</sup> ions in the channels of the structure (Section 1.1.2).

The structure of  $\beta$ -spodumene consists of corner sharing Si and Al tetrahedra forming interconnected five-membered rings, which create channels. The ultralow thermal expansion of  $\beta$ -spodumene is anisotropic and due to the release of strain in the five-membered rings; *a* and *b* axes contract, and corner-connecting oxygen atom angles increase, the *c*-axis expands, resulting in an overall ultralow thermal expansion for the

material.  $\beta$ -eucryptite consists of a spiral network of tetrahedra that, when heated, are put under torsion stress with contraction of the network, like that in a coiled spring.

### ***1.3.6 Cordierite Family ( $2\text{MgO} \cdot 2\text{Al}_2\text{O}_3 \cdot 5\text{SiO}_2$ )***

The crystal structure of magnesium cordierite,  $\text{Mg}^{\text{VI}}_2\text{Al}^{\text{IV}}_3(\text{Si}_5\text{Al})^{\text{IV}}\text{O}_{18}$ , is based on corner-sharing of one Al tetrahedron and five Si tetrahedra forming six-membered hexagonal rings. The rings are, in turn, interconnected to form two structural cavities per structural unit. The cordierite family consists of anisotropic low thermal expansion materials with small expansion along the  $a$ -axis, parallel to the rings, and a small contraction along the  $c$ -axis, perpendicular to the rings.<sup>1</sup>

### ***1.3.7 Silica and $\text{SiO}_2$ - $\text{TiO}_2$ Glasses***

In general, glasses possess many attractive properties for use as thermal shock-resistant materials, such as homogeneity, non-porosity, chemical inertness, and their isotropic nature. Silica ( $\text{SiO}_2$ ) and silicate glasses (continuous, random networks of silica-oxygen linkages) exhibit these characteristics along with ultralow CTEs ( $\alpha = 0.5 \times 10^{-6} \text{ }^\circ\text{C}^{-1}$  for silica in the temperature range from 25 - 800°C). Pyrex brand dinnerware is produced using an optimum composition of silica and boric oxide, which is added to increase thermal expansion. The low thermal expansion observed in silica and silicate glasses is due to strong Si-O bonds, where changes in volume due to thermal perturbation would be small. The addition of  $\text{TiO}_2$  to silica glasses can affect the CTEs of resulting products, which can increase or decrease depending on the  $\text{TiO}_2$  concentration.<sup>1</sup> One type

of titanium silicate glass used in optical mirror applications has a reported zero CTE over a wide range of temperatures.

### **1.3.8 Zeodur**

Zeodur consists of a glassy phase (approximately 30%) and a crystalline phase (approximately 70%) and is characterized by low positive expansion and low NTE, depending upon synthesis processes, over a range of temperatures from  $-195\text{ }^{\circ}\text{C}$  to  $600\text{ }^{\circ}\text{C}$ . The crystalline phase (high quartz structure) is embedded in a glassy phase of  $\text{SiO}_2$  and  $\text{AlPO}_4$  matrix and exhibits NTE, while the glassy phase displays low positive thermal expansion behavior. Zero thermal expansion is possible in this material by tailoring the amounts of crystalline and glassy phases during processing.<sup>1</sup>

### **1.3.9 Invar**

A metallic alloy consisting of around 35% Ni, Invar is a low expanding material with a CTE  $\alpha = 0.07 \times 10^{-6}\text{ }^{\circ}\text{C}^{-1}$  at  $20\text{ }^{\circ}\text{C}$ . The observed low expansion has been reported as a consequence of the arrangement of magnetic domains in the alloy upon the absorption of thermal energy (Section 1.1.1). Normal, positive thermal expansion of the material is observed below the Curie temperature; a contraction is observed close to this point, and the resumption of normal thermal expansion and paramagnetic behavior is observed as heating continues. The Invar effect and overall low thermal expansion in Invar alloys appears to be a direct result of magnetic microdomains (compositional atomic inhomogeneities) and magnetostriction phenomenon. Lattice expansion, due to

increased vibrations between ordered compositional inhomogeneous atoms, is cancelled by a ferromagnetic ordering process.<sup>1</sup>

#### 1.4 Goals of Research

Two families of low and NTE materials are the focus of the research for this present work, the  $A^{IV}M^V_2O_7$  and  $M^{III}M^V P_4O_{14}$  families (Sections 1.2 and 1.2.4, respectively). The variety of synthesis methods and its impact on temperatures of crystallization provides an opportunity to examine known members of the  $A^{IV}M^V_2O_7$  family to determine if different synthesis methods and/or starting materials unexplored in the literature can alter the crystallization behavior of some pyrophosphates. Low temperature synthesis methods, such as non-hydrolytic and hydrolytic sol-gel methods, acid digestion, and mild autoclave methods, will be used to make this determination.

Hydrolytic sol-gel methods will be used to explore the possibility of producing a broader range of  $M^{III}M^V P_4O_{14}$  materials using various combinations of  $M^{III}$  cations with  $Nb^{5+}$  or  $Ta^{5+}$  cation starting materials. With a larger number of compounds for analysis, trends in CTEs and room temperature lattice constants for compounds can be examined, as well as trends in lattice constants, average ionic radii, and CTE's.

Characterization techniques, such as high resolution synchrotron powder XRD, *in situ* high temperature synchrotron powder XRD, and high-pressure synchrotron powder XRD, will be used to examine details of structure, as well as thermal expansion and high pressure behavior, previously unexplored in the literature for some  $A^{IV}M^V_2O_7$  compounds. TEM/ED and *in situ* high temperature lab powder XRD will be used to examine  $M^{III}M^V P_4O_{14}$  materials in order to examine structural properties,

thermophysical properties, and any impact of substitution of various  $M^{III}M^V$  cations on the ordering of the framework of compounds at room temperature and upon heating.

## 1.5 References

1. Roy, R.; Agrawal, D. K.; McKinstry, H. A., Very Low Thermal Expansion Coefficient Materials. *Annu. Rev. Mater. Sci.* **1989**, 19, 59-81.
2. Sleight, A. W., Isotropic Negative Thermal Expansion. *Annual Review of Materials Science* **1998**, 28, 29-43.
3. Evans, J. S. O., Negative Thermal Expansion Materials. *J. Chem. Soc. Dalton Trans.* **1999**, 3317-3326.
4. Sleight, A. W., Compounds that Contract on Heating. *Inorg. Chem.* **1998**, 37, 2854-2860.
5. Barrera, G. D., Bruno, J. A. O., Barron, T. H. K., and Allan, N. L., Negative thermal expansion. *J. Phys.: Condens. Matter* **2005**, 17, R217-R252.
6. Evans, J. S. O.; Mary, T. A.; Sleight, A. W., Negative thermal expansion materials. *Physica B* **1998**, 241-243, 311-316.
7. Tao, J. Z. a. S., A. W., The role of rigid unit modes in negative thermal expansion. *Journal of solid State Chemistry* **2003**, 173, (2), 442-448.
8. Evans, J. S. O.; David, W. I. F.; Sleight, A. W., Structural investigation of the negative-thermal-expansion material  $ZrW_2O_8$ . *Acta Cryst.* **1999**, B55, 333-340.
9. Mary, T. A.; Evans, J. S. O.; Vogt, T.; Sleight, A. W., Negative Thermal Expansion from 0.3 to 1050 Kelvin in  $ZrW_2O_8$ . *Science* **1996**, 272, 90-92.
10. Martinek, C.; Hummel, F. A., Linear Thermal Expansion of Three Tungstates. *J. Am. Ceram. Soc.* **1968**, 51, 227-228.
11. Hammonds, K. D., dove, M. T, Giddy, A. P, and Heine, V., *Am. Mineral.* **1994**, 79, 1207.
12. Withers, R. L.; Tabira, Y.; Evans, J. S. O.; King, I. J.; Sleight, A. W., A New Three-Dimensional Incommensurately Modulated Cubic Phase (in  $ZrP_2O_7$ ) and its Symmetry Characterization via Temperature-Dependent Electron Diffraction. *J. Solid State Chem.* **2001**, 157, 186-192.
13. Pryde, A. K. A.; Hammonds, K. D.; Dove, M. T.; Heine, V.; Gale, J. D.; Warren, M. C., Origin of the Negative Thermal Expansion in  $ZrW_2O_8$  and  $ZrV_2O_7$ . *J. Phys. Condens. Matter* **1996**, 8, 10973-10982.
14. Xing. X., C., J., Deng, J., and Liu, G., Solid solution  $Pb_{1-x}Sr_xTiO_3$  and its thermal expansion. *Journal of Alloys and Compounds* **2003**, 360, 286-289.

15. Ackermann, R. J., Thermal Expansion and the High-Low Transformation in Quartz. I. High-Temperature X-ray Studies. *J. Appl. Cryst.* **1974**, 7, 461-467.
16. Oyetola, S.; Verbaere, A.; Guyomard, D.; Crosnier, M. P.; Piffard, Y.; Tournoux, M., New  $ZrP_2O_7$ -like diphosphates of either mixed ( $M^{III}_{0.5}M^{V}_{0.5}$ ) cations (  $M=Sb, Bi, Hd, Eu$ ;  $M'=Sb, Nb, Ta$ ) or  $M^V$  cations ( $M'=Ta, Nb$ ): synthesis and structure. *Eur. J. Solid State Inorg. Chem.* **1991**, 28, 23-36.
17. Varga, T., Preparation and thermal expansion of  $(M^{III0.5}M^{V0.5})P_2O_7$  with the cubic  $ZrP_2O_7$  structure. *Journal of Solid State Chemistry* **2005**, 178, 3541-3546.
18. Korthuis, V.; Khosrovani, N.; Sleight, A. W.; Roberts, N.; Dupree, R.; Warren, W. W., Negative Thermal Expansion and Phase Transitions in the  $ZrV_{2-x}P_xO_7$  Series. *Chem. Mater.* **1995**, 7, 412-417.
19. Fukuoka, H.; Imoto, H.; Saito, T., Preparation of Cubic Niobium Pyrophosphate Containing Nb(IV) and Topotactic Extraction of Phosphorus Atoms. *J. Solid State Chem.* **1995**, 119, 98-106.
20. Hagman, L. O.; Kierkegaard, P., Note on the Structures of  $M^{IV}P_2O_7$  ( $M^{IV} = Ge, Zr$ , and U). *Acta Chem. Scand.* **1969**, 23, 327-328.
21. Khosrovani, N.; Korthuis, V.; Sleight, A. W.; Vogt, T., Unusual  $180^\circ$  P-O-P Bond Angles in  $ZrP_2O_7$ . *Inorg. Chem.* **1996**, 35, 485-489.
22. King, I. J.; Fayon, F.; Massiot, D.; Harris, R. K.; Evans, J. S. O., A space group assignment of  $ZrP_2O_7$  obtained by  $^{31}P$  solid state NMR. *Chem. Commun.* **2001**, 1766-1767.
23. Hajo, O., *Naturwissenschaften* **1961**, 52, 344.
24. Le Flem, G. L., J.; Hagenmuller, P., *Memoires Presentes A La Societe Chimique* **1966**, 1880.
25. Pedregosa, e. a., *Anales. Asoc. Quim. Argentina* **1972**, 60, 397.
26. Baran, E. J., The unit cell of hafnium divanadate. *J. Less Common Met.* **1976**, 46, 343-345.
27. Tillmans, E.; Gebert, W.; Baur, W. H., Computer Simulations of Crystal Structures Applied to the Solution of the Superstructure of Cubic Silicodiphosphate. *J. Solid State Chem.* **1973**, 7, 69-84.
28. Vollenkle, H.; Wittmann, A.; Nowotny, H., Uber Diphosphate vom Typ  $Me(IV)P_2O_7$ . *Monatshefte fur Chemie* **1963**, 94, 956-963.

29. Losilla, E. R.; Cabeza, A.; Bruque, S.; Aranda, M. A. G.; Sanz, J.; Iglesias, J. E.; Alonso, J. A., Syntheses, Structures, and Thermal Expansion of Germanium Pyrophosphates. *J. Solid State Chem.* **2001**, 156, 213-219.
30. Helluy, X.; Marichal, C.; Sebald, A., Through-Bond Indirect and Through-Space Direct Dipolar Coupling  $^{31}\text{P}$  MAS NMR Constraints for Spectral Assignment in the Cubic  $3\times 3\times 3$  Superstructure of  $\text{TiP}_2\text{O}_7$ . *J. Phys. Chem. B* **2000**, 104, 2836-2845.
31. Sanz, J.; Iglesias, J. E.; Soria, J.; Losilla, E. R.; Aranda, M. A. G.; Bruque, S., Structural Disorder in the Cubic  $3\times 3\times 3$  Superstructure of  $\text{TiP}_2\text{O}_7$ . XRD and NMR Study. *Chem. Mater.* **1997**, 9, 996-1003.
32. Norberg, S. T.; Svensson, G.; Albertsson, J., A  $\text{TiP}_2\text{O}_7$  superstructure. *Acta Cryst. Section C* **2001**, 57, 225-227.
33. Botto, V. I. L. a. B., E. J., Kristallographische Daten, IR-Spektrum und thermisches Verhalten von Cer(IV)-Diphosphat. *Z. anorg. allg. Chem.* **1977**, 430, 283-288.
34. Fayon, F.; King, I. J.; Harris, R. K.; Gover, R. K. B.; Evans, J. S. O.; D., M., Characterization of the room-temperature structure of  $\text{SnP}_2\text{O}_7$  by  $^{31}\text{P}$  through space and through bond NMR correlation spectroscopy. *Chem. Mater.* **2003**, 15, 2234-2239.
35. Huang, C.-H.; Knop, O.; Othen, D. A., Pyrophosphates of Tetravalent Elements and a Mossbauer Study of  $\text{SnP}_2\text{O}_7$ . *Canadian Journal of Chemistry* **1975**, 53, 79-91.
36. Krogh Andersen, A. M. N., P., *Ab initio* structure determination and Rietveld refinement of a high-temperature phase of zirconium hydrogen phosphate and a new polymorph of zirconium pyrophosphate from *in situ* temperature-resolved powder diffraction data. *Acta Crystatollgr., Section B* **2000**, B56, 618-625.
37. Evans, J. S. O.; Hanson, J. C.; Sleight, A. W., Room-Temperature Superstructure of  $\text{ZrV}_2\text{O}_7$ . *Acta Cryst.* **1998**, B54, 705-713.
38. Withers, R. L.; Evans, J. S. O.; Hanson, J.; Sleight, A. W., An *in Situ* Temperature-Dependent Electron and X-ray Diffraction Study of Structural Phase Transitions in  $\text{ZrV}_2\text{O}_7$ . *J. Solid State Chem.* **1998**, 137, 161-167.
39. Kirchner, H. P.; Merz, K. M.; Brown, W. R., Thermal Expansion of Uranium Pyrophosphate and Ceramic Bodies in the System  $\text{UO}_2\text{-P}_2\text{O}_7$ . *J. Am. Ceram. Soc.* **1963**, 46, 137-141.
40. Laud, K.; Hummel, F. A., The system  $\text{ThO}_2\text{-P}_2\text{O}_5$ . *J. Am. Ceram. Soc.* **1971**, 54, 296-298.
41. Harrison, D. E.; Hummel, F. A., Reactions in the System  $\text{TiO}_2\text{-P}_2\text{O}_5$ . *J. Am. Ceram. Soc.* **1959**, 42, 487-490.

42. Gover, R. K. B.; Withers, N. D.; Allen, S.; Withers, R. L.; Evans, J. S. O., Structure and Phase Transitions in  $\text{SnP}_2\text{O}_7$ . *J. Solid State Chem.* **2002**, 166, 42-48.
43. Shannon, R. D., Revised Effective Ionic Radii and Systematic Studies of Interatomic Distances in Halides and Chalcogenides. *Acta Crystallogr., Section A* **1976**, A32, 751-767.
44. Sleight, A. W., Thermal Contraction. *Endeavour* **1995**, 19, 64-68.
45. Buchanan, R. C.; Walter, G. W., Properties of Hot-Pressed Zirconium Pyrovanadate Ceramics. *J. Electrochem. Soc.* **1983**, 130, 1905-1910.
46. Craig, D. F.; Hummel, F. A., Zirconium Pyrovanadate Transitions. *J. Am. Ceram. Soc.* **1972**, 55, 532.
47. Burdese, A., et al., *Anal. Chim. (Rome)* **1960**, 50, 1570.
48. Peyronel, G., *Gazz. Chim. Ital.* **1942**, 72, 77.
49. Lezama, L. R., J. M.; Mesa, J. L.; Rojo, T., *Journal of Solid State Chemistry* **1995**, 115, 146-151.
50. Banks, E.; Sacks, R.,  $\text{ReP}_2\text{O}_7$ : A New Isomorph of  $\text{ZrP}_2\text{O}_7$ . *Mat. Res. Bull.* **1982**, 17, 1053-1055.
51. Kinomura, N.; Hirose, M.; Kumada, N.; Muto, F., Molybdenum (IV) Pyrophosphate Isostructural with  $\text{ZrP}_2\text{O}_7$ . *Mat. Res. Bull.* **1985**, 20, 379-382.
52. Teweldemedhin, Z. S.; Ramanujachary, K. V.; Greenblatt, M., New Tungsten Pyrophosphate with Cubic Zirconium Pyrophosphate-Type Structure. *Mat. Res. Bull.* **1993**, 28, 427-434.
53. Harrison, D. E.; McKinstry, H. A.; Hummel, F. A., High-Temperature Zirconium Phosphates. *J. Am. Ceram. Soc.* **1954**, 37, 277-280.
54. Pole, G. R.; Beinlich, A. W.; Gilbert, N., Physical Properties of some High-Temperature Refractory Compositions. *J. Am. Ceram. Soc.* **1946**, 29, 208-222.
55. Clearfield, A.; Blessing, R. H., The Preparation and Crystal Structure of a Basic Zirconium Molybdate and its Relationship to Ion Exchange Gels. *J. Inorg. Nucl. Chem.* **1972**, 34, 2643-2663.
56. Liebau, V. F.; Bissert, G.; Koppen, N., Synthese und kristallographische Eigenschaften einiger Phasen im System  $\text{SiO}_2\text{-P}_2\text{O}_5$ . *Z. Anorg. Alleg. Chem.* **1968**, 359, 113-134.
57. Alberti, G., Costantino, U., and Zsinka, L., Crystalline Insoluble Acid Salts of Tetravalent Metals - XII. *Inorg. nucl. Chem.* **1972**, 34, 3549-3560.

58. Bjorklund, C. W., The Preparation of  $\text{PuP}_2\text{O}_7$  and  $\text{PuPO}_4$ . *J. Am. Chem. Soc.* **1958**, 79, 6347-6350.
59. Turquat, C.; Muller, C.; Nigrelli, E.; Leroux, C.; Soubeyroux, J.-L.; Nihoul, G., Structural investigation of temperature-induced phase transitions in  $\text{HfV}_2\text{O}_7$ . *The European Physical Journal Applied Physics* **2000**, 10, 15-27.
60. Krogh Anderson, A. M.; Norby, P.; Hanson, J. C.; Vogt, T., Preparation and Characterization of a New 3-Dimensional Zirconium Hydrogen Phosphate,  $\tau\text{-Zr}(\text{HPO}_4)_2$ ; Determination of the Complete Crystal Structure by Combining Synchrotron X-ray Crystal Diffraction and Neutron Powder Diffraction. *Inorg. Chem.* **1998**, 37, 876-881.
61. Ota, T.; Yamai, I., Thermal-Expansion of  $\text{ZrP}_2\text{O}_7$  and Related Solid-Solutions. *Journal of Materials Science* **1987**, 22, (10), 3762-3764.
62. Lind, C.; Wilkinson, A. P.; Hu, Z.; Short, S.; Jorgensen, J. D., Synthesis and Properties of the Negative Thermal Expansion Material Cubic Zirconium Molybdate. *Chemistry of Materials* **1998**, 10, 2335-2337.
63. Evans, J. S. O.; Mary, T. A.; Vogt, T.; Subramanian, M. A.; Sleight, A. W., Negative Thermal Expansion in  $\text{ZrW}_2\text{O}_8$  and  $\text{HfW}_2\text{O}_8$ . *Chem. Mater.* **1996**, 8, 2809-2823.
64. Wilkinson, A. P.; Lind, C.; Pattanaik, S., A New Polymorph of  $\text{ZrW}_2\text{O}_8$  Prepared using Nonhydrolytic Sol-Gel Chemistry. *Chem. Mater.* **1999**, 11, 101-108.
65. Closmann, C.; Sleight, A. W., Low-Temperature Synthesis of  $\text{ZrW}_2\text{O}_8$  and Mo-Substituted  $\text{ZrW}_2\text{O}_8$ . *Journal of Solid State Chemistry* **1998**, 139, 424-426.
66. Martinek, C. A.; Hummel, F. A., Subsolidus Equilibria in the System  $\text{ZrO}_2\text{-WO}_3\text{-P}_2\text{O}_5$ . *J. Am. Ceram. Soc.* **1970**, 53, 159-161.
67. Evans, J. S. O.; Mary, T. A.; Sleight, A. W., Structure of  $\text{Zr}_2(\text{WO}_4)(\text{PO}_4)_2$  from Powder X-ray Data: Cation Ordering with No Superstructure. *J. Solid State Chem.* **1995**, 120, 101-104.
68. Laud, K. R.; Hummel, F. A., Subsolidus Relations in the System  $\text{ZrO}_2\text{-ThO}_2\text{-P}_2\text{O}_5$ . *J. Am. Ceram. Soc.* **1971**, 54, 407-409.
69. Wallez, G. L., S.; Souron, J. P.; Quarton, M.; Suard, E., Beta-Zirconium Oxide Monophosphate: Structural Keys for an Ultralow Expansion Material. *Chem. Mater.* **2003**, 15, 3793-3797.

## CHAPTER 2

### INSTRUMENTAL METHODS AND DATA ANALYSIS

#### 2.1 X-Ray Diffraction

X-Ray diffraction encompasses single crystal and powder X-ray diffraction (XRD) methods and is concerned with both structure analysis and phase identification.<sup>1</sup> Single crystal diffraction has the advantage in its ability to aid in the determination of structure and atomic positions of most crystalline compounds; however, not all crystalline compounds form crystals large enough for single crystal XRD. Powder XRD is primarily a method to determine the identity of microcrystalline compounds by their powder patterns, and secondarily a method for structure analysis.

Diffraction is described by Bragg's Law:

$$n\lambda = 2d \sin \theta, \quad (1)$$

where  $\lambda$  is the wavelength,  $n$  is an integer representing the order of the diffracted beam,  $d$  is d-spacing between lattice planes, and  $2\theta$  is the angle of diffraction.<sup>3</sup>

Figure 2.1 shows how an incident x-ray beam strikes a microcrystalline powder sample, is diffracted, and travels to a detector at the Bragg angle. The diffracted beam is not a single beam as depicted in the diagram, but is a cone-shaped set of scattered beams. X-rays are only diffracted when the incident angle on the lattice plane equals the diffracted angle.

In powder diffraction, one is interested in determining d-spacing between lattice

planes of crystalline materials. Figure 2.2 illustrates Bragg's law, equation (1). The angle between the incident beam (dashed lines) and the diffracted beams (solid lines) is  $2\theta$ ;  $d$ -spacing is a material characteristic, but  $2\theta$  is dependent on the wavelength,  $\lambda$ .

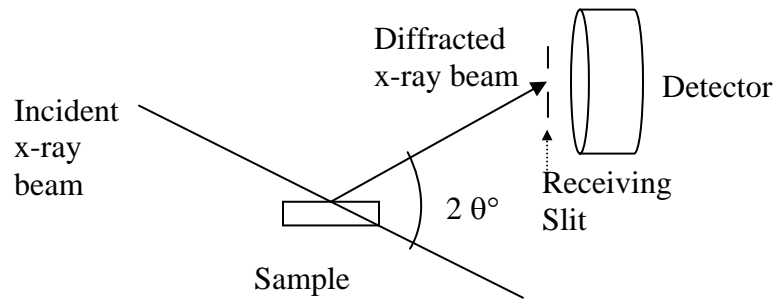


Figure 2.1: Diagram of powder XRD on microcrystalline sample showing incident beam, diffracted beam to a detector through a receiving slit, and the Bragg angle of diffraction.

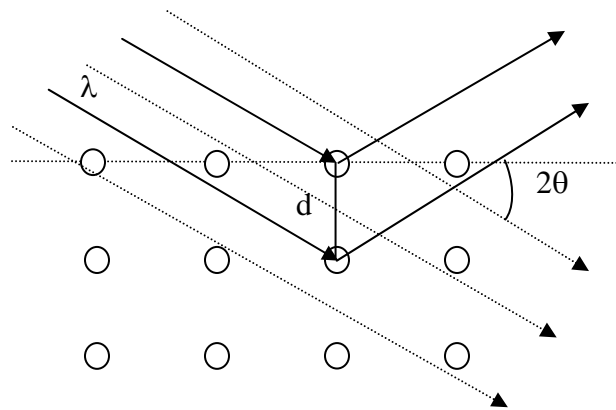


Figure 2.2: X-ray radiation diffracting (solid arrows) from two parallel lattice planes and incident beams (dotted arrows). The angle  $2$ -theta is that which is made between the incident and diffracting beams;  $d$  is the distance between planes and  $\lambda$  is the wavelength.

In laboratory XRD instruments, X-rays are typically produced when a Cu or Mo anode, for example, is bombarded with high energy electrons. The Cu or Mo atomic electrons are excited to higher energy levels by the incident high energy electrons; when the excited electrons in Cu or Mo anodes transition to lower energy levels, photons are emitted in the X-ray region. Other anode materials include W, Fe, Ag, Cr, Co, and Ag. The minimum wavelength of the continuous radiation produced is a function of Planck's constant,  $h$ , times the speed of light,  $c$ , over the maximum accelerating potential,  $V$  (in kV), of the high energy particles:<sup>1</sup>

$$\lambda_{\min} = \frac{hc}{V} = \frac{12.3985}{V} \text{ \AA} \quad (2)$$

The radiation is collimated to irradiate a powder sample at the wavelength of the anode material. The intensity of the x-ray beam decreases as it passes through the sample and this decrease is related to the distance the beam travels,  $x$ , and  $\mu$ , the linear absorption coefficient (dependent of the properties of the substance, its density, and the wavelength of the x-rays). The fractional decrease in intensity,  $I$ , is, therefore:<sup>4,5</sup>

$$-\frac{dI}{I} = \mu dx \quad (3)$$

Integration of equation (3) gives the following relationship between intensity of the incident beam ( $I_0$ ) and the beam after it travels a distance  $x$  through the material:

$$I = I_0 \exp(-ux) \quad (4)$$

The linear absorption coefficient,  $\mu$ , is linearly proportional to  $\rho$ , the density of the substance and can be expressed as the mass absorption coefficient ( $\mu/\rho$ ) in the following equation:

$$I_x = I_0 \exp\left(-\rho \frac{\mu}{\rho} x\right) \quad (5)$$

The diffracted x-ray beams are collimated through slits and can proceed through a monochromator to select a wavelength of interest, or directly to a detector. For example, a graphite crystal monochromator can be used to select only the  $\text{CuK}\alpha$  wavelength and filter out  $\text{CuK}\beta$  radiation from a Cu anode x-ray tube. In a solid state semi-conductor detector, undesirable wavelengths can be filtered out with energy discriminating electronics.

Detection of diffracted beams can be accomplished by a variety of devices. Strips of photographic film were used initially in powder x-ray diffraction, surrounding the sample to capture diffracted beam image patterns (concentric arcs around a beam center) from which d-spacing could be calculated and indexing of the pattern (determination of lattice planes) could be accomplished. Photographic film is still used for powder x-ray detection, but detectors have evolved to include charge-coupled devices (CCD), solid state semi-conductor devices, scintillation counters, image plates (IP), and a variety of other technologies.

The common characteristic of all detectors is to provide a method for capturing the energy from diffracted beams and integrating that energy into electrical signals that

can be recorded by a computer processing method.<sup>6</sup> Differences include the types of methods and materials used to capture the diffracted energy. Image plate (IP) detectors can provide rapid capture of powder patterns in several minutes and are reusable. Some IP detectors consist of plate with an outer protective layer, a photo stimulation phosphor layer, and two support layers, one a polymer and the other an outer metal supporting layer. The active layer resides in the phosphor layer where crystals (doped barium fluoro-bromide crystals, for example) are embedded in a resin. X-rays diffracted from samples excite the crystals to a semi-stable state. With illumination of barium fluoro-bromide crystals with red laser light, the crystals are excited and stimulated to release the stored information in the form of a blue luminescence signal, the amount of which is dependent on the initial X-ray excitation. Illumination of the crystals with white light for a short period of time releases all stored energy in the crystals and the IP is ready for use again.<sup>1,</sup>

4

Solid state semi-conductor detectors are based on the creation of electron-hole pairs in Si or Ge. When incident X-ray radiation strikes silicon, for example, electrons are promoted to the conduction band. Conductivity results and a potential applied across the Si crystal results in a current pulse that accompanies the absorption of each photon. The size of the pulse is directly proportional to the energy of the absorbed photons. The solid-state semi-conductor detector allows good energy discrimination to select or reject certain wavelengths.<sup>1, 7</sup>

An example of a scintillation detector is one consisting of a transparent crystal of sodium iodide activated by the doping of a small concentration of thallium iodide and often in the shape of a cylinder. One of the plane surfaces of the cylinder faces the

cathode of a photomultiplier tube. Radiation is absorbed by the scintillator crystal and released as photons of fluorescence radiation. The flashes of blue light produced by the scintillator crystal are transmitted to a photomultiplier tube, where a chain of dynodes (photosurfaces), each at a successively higher potential, accelerate and, thus, multiplies the electrons resulting in an exponential increase in the signal. The electrons are eventually collected at the anode and converted to electrical pulses.<sup>1,7</sup>

In the present research, laboratory powder X-ray diffraction in the Bragg-Brentano ( $\theta$ : $\theta$ ) arrangement was the method of initial characterization for the synthesized products. Synchrotron radiation (Section 2.1.2) was employed for high resolution structure studies, high pressure studies, and *in situ* high temperature thermal expansion and dehydration studies. Detectors used included solid state semiconductor detectors, IPs, and scintillators.

### ***2.1.1 Powder X-Ray Diffraction and Variable Temperature Thermal Expansion Analysis at Georgia Institute of Technology and at Oak Ridge National Laboratory, Oak Ridge, TN***

The instrumentation used for the majority of samples prepared in the present research was a Scintag X1 Advanced Diffraction System with a Cu K $\alpha$  X-ray tube, and a Peltier cooled Si semi-conductor detector. Powder samples were loaded onto a normal sample stage for room temperature powder X-ray diffraction.

A Panalytical X'Pert Pro lab powder XRD instrument with an Anton Paar XRK 900 high temperature furnace and an X'Celerator Real Time Multiple Si strip detector were used for many samples prepared in this research courtesy of Dr. Andrew Payzant at the High Temperature Materials Laboratory, Oak Ridge National Labs, Oak Ridge, TN.

A 0.04 radian soller slit, a 10mm mask to limit the width of the incident beam, and a programmable divergence slit ( $0.5^\circ - 1.0^\circ - 0.5^\circ$ ) were used on the incident beam side, while a 0.04 radian soller slit, Ni foil, and an anti-scatter slit was used on the diffracted beam side. Figure 2.3, top image, shows the X'Pert Pro experimental set up with Anton Paar XKD 900 furnace housing the sample and X'Celerator detector. The bottom image in Figure 2.3 is the sample stage that fits into the Anton Paar XKD 900 furnace.

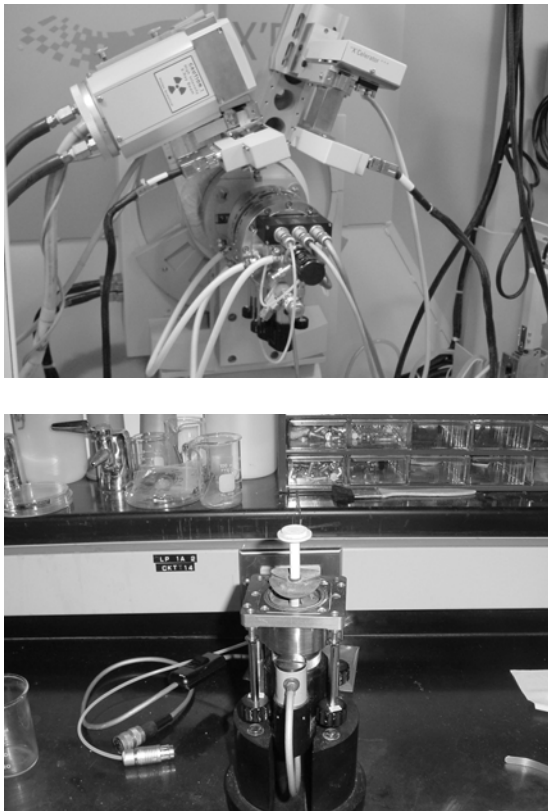


Figure 2.3: Top, Panalytical X'Pert Pro experimental set up with furnace at Oak Ridge National Labs. Bottom, sample stage; sample is transferred to the round ceramic lipped holder at the top.

The sample holder consists of a ceramic disk on a rod that serves as an attachment

base to the sample stage unit. The sample is loaded into the basin of the disk to its rim and smoothed, usually with a glass microscope slide. The thermocouple is inserted through the base of the sample stage to be situated parallel with the sample holder, but bent away from it by about 2 mm. Variable temperature studies were accomplished from room temperature up to 900°C with varied increments depending upon the sample. Scans covered 13 to 140 two-theta (°) and were programmed to begin when the desired temperature was reached.

### ***2.1.2 Synchrotron Powder XRD***

Synchrotron X-rays consist of highly intense white radiation that is collimated, pulsed, and polarized. Highly kinetic energy electrons are accelerated around a large evacuated ring and constrained inside the ring using magnets. Synchrotron radiation is the emission from the accelerated particles (electrons or positrons) due to the magnetic fields. The radiation emitted by synchrotron sources is much brighter than that from conventional lab x-ray instruments.<sup>5</sup>

Synchrotron radiation makes it possible to detect fine details in peaks of powder patterns that can aid in structural studies of compounds. In a high resolution experiment, X-rays diffracted from the powder sample are diffracted again using a single crystal analyzer before reaching the detector.<sup>4</sup> The use of a single crystal as a receiving slit permits the highest angular resolution, ~ 0.01° full width at half maximum (FWHM), which results in the widths of diffraction peaks being determined by the sample. In addition, fluorescence from the sample is eliminated.

### ***2.1.3 Synchrotron Powder XRD at Argonne National Labs, Argonne, IL***

Some synchrotron experiments were performed at the Advanced Photon Source (APS) at Argonne National Laboratory, Argonne, IL. Experiments involving the use of synchrotron powder XRD included *in situ* variable temperature thermal expansion ( $\lambda = 0.605122 \text{ \AA}$ ) studies from 14K to 300K and from 25°C to 750°C on cerium pyrophosphate, and an *in situ* dehydration study ( $\lambda = 0.13762 \text{ \AA}$ ) on a sample of cerium dihydrogen phosphate hydrate from 25°C to 800°C. A flat plate cryostat set up with a helium displax cooling system was used for low temperature thermal expansion scans, while for high temperature scans the samples were loaded into quartz capillaries plugged with silanized quartz wool. The capillaries were placed into a furnace made for the

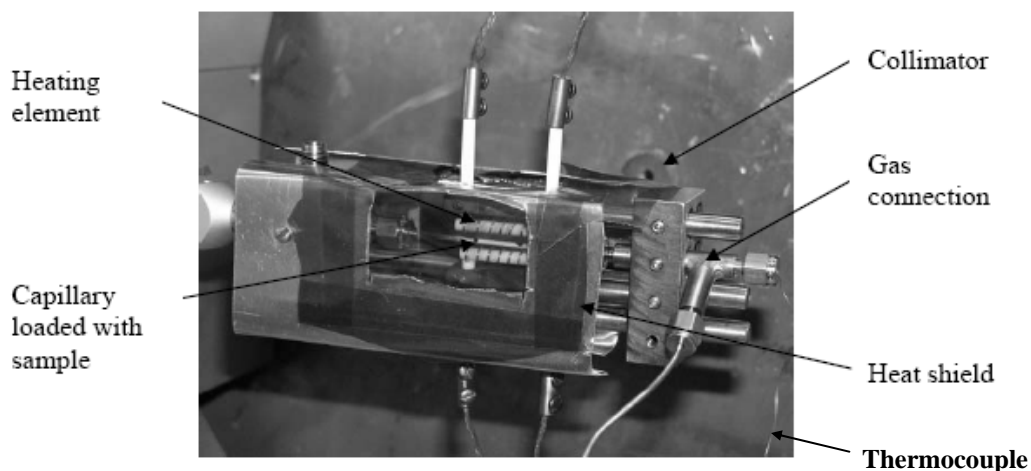


Figure 2.4: Experimental set up using a furnace modified for heating capillaries. The samples in this experiment were heated in air. Picture modified from T. Varga.<sup>2</sup>

purpose of high temperature synchrotron powder XRD, Figure 2.4. The collimator reduces the background around the sample. The available gas connection was used in the

dehydration study for flowing argon gas, though the high temperature thermal expansion experiment was done in air. The heat shield consists of metal plates held together with screws and covered with Kapton tape; two heating elements can be seen above and below the capillary loaded with sample in Figure 2.4. Power connections at the top and bottom of the device join the heating elements to a power source. A thermocouple (Omega K-type) was inserted into the sample, through the silanized wool in the capillary, and attached to a thermocouple reader. The experimental set up also included motorized rocking of the capillary and furnace.

A MAR 345 image plate detector (11 ID B beam line) was used for the dehydration study; wavelength and sample to detector distance calibration had previously been done with a  $\text{CeO}_2$  standard. Data was processed using Fit2d<sup>8</sup> (Section 2.54) software and saved as standard GSAS<sup>9</sup> (Section 2.52) data files for analysis; JADE software was used to analyze the patterns in the form of .chi files from Fit2d software. In the thermal expansion study, a Cyberstar LaCl scintillator detector was used (1-BM-C beam line); optics included a silicon (111) analyzer crystal. The horizontal beam size was 1.5 mm; the vertical beam size was 0.5mm. Silicon was used as a standard for calibration of the wavelength. CMPR software, compiled by Brian H. Toby at the NIST Center for Neutron Research, was used to view the experimental data and to save it in a more convenient form.

High resolution synchrotron powder XRD was also used for a room temperature structural study of  $\text{CeP}_2\text{O}_7$  (32ID beam line) with the help of Dr. Peter Lee. Figure 2.5 shows the experimental set up on 32ID beamline highlighting the motorized sample

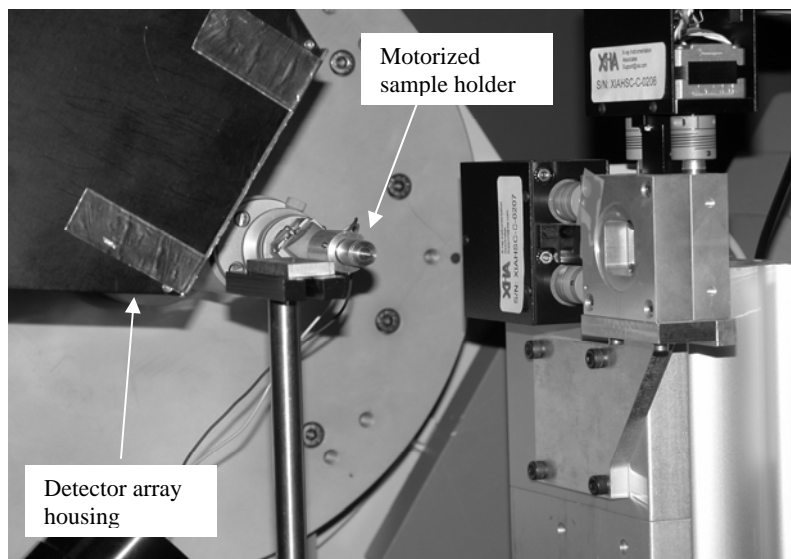


Figure 2.5: Experimental set up on 32ID beamline at APS. Spinning sample unit holds 1 mm capillary. Black, angular device holds detector array. Photo courtesy, Dr. Peter Lee.

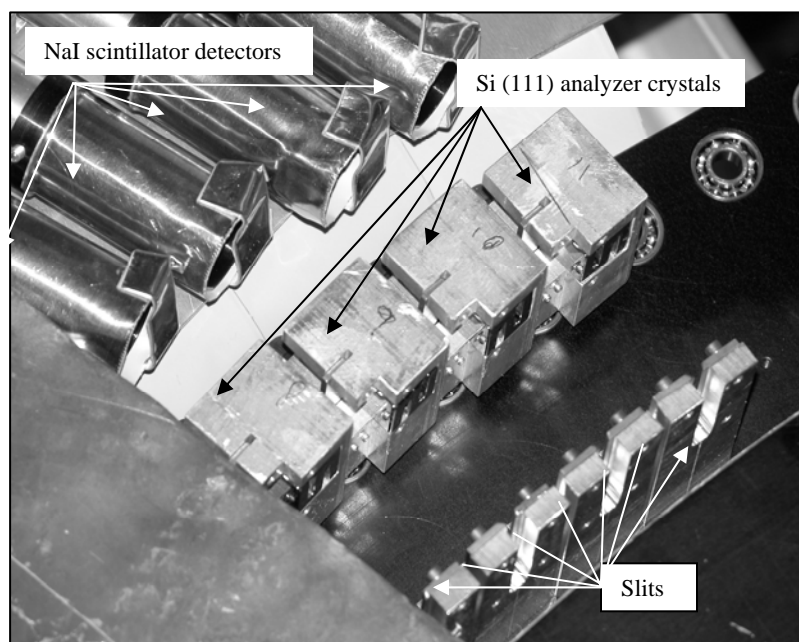


Figure 2.6: Detector array on 32ID beamline showing four of the eleven NaI detector heads, Si (111) crystal analyzers, and beam slits inside housing unit. Photo courtesy, Dr. Peter Lee.

holder and housing for detector array (photographs courtesy of Dr. Peter Lee). The sample was packed in a 1mm capillary and mounted for spinning. The beam line has a Kohzu monochromator which consists of water-cooled diamond (111) crystals; the wavelength was 0.4961475 Å. Figure 2.6 shows four of the eleven Si (111) NaI detector units inside the housing.

#### **2.1.4 High Pressure Synchrotron Powder XRD at CHESS**

High pressure experiments are an important component of the overall study of thermal expansion materials. Pressure-induced phase transitions including crystalline-to-crystalline and amorphization can result in property changes.<sup>10</sup>

Cornell High Energy Synchrotron Source (CHESS), Cornell University, Ithaca, New York, was utilized for high pressure synchrotron studies on cerium pyrophosphate using diamond anvil cells (DACs). Figure 2.7 shows the experimental set up. The sample stage is on an optical table and can be moved in three-dimensions under computer control. 25.1 keV X-rays were selected using a Ge (111) monochromator and collimated to 50 microns. Diffraction data were recorded on a MAR 345 IP detector. The data were processed with Fit2d<sup>11</sup> software (Section 2.54) and saved as standard GSAS<sup>9</sup> (Section 2.52) files; JADE<sup>12</sup> software (Section 2.51) was used for phase identification.

Samples were loaded into prepared metal gaskets (rhenium or steel), ~ 125 µm thick with a 200 – 300 µm hole drilled in the center to receive the sample. Gaskets were centered on one of two diamonds, each approximately 600 µm across the face and 1.6 mm thick, after an indentation was made on the gasket by closing the two halves of the

cell. In Figure 2.8, diamonds are visible in the center of the blue epoxy holding them onto the backing plate; the metal gasket is not shown.

The pressure transmitting medium used was a mixture of methanol/ethanol (approximately 4:1 MeOH : EtOH). A DAC can be seen assembled in Figure 2.9, which also shows the method of loading the methanol/ethanol pressure transmission medium onto the sample before closing the DAC. The DAC sits on a microscope stage, assembled, but open enough to insert a pulled glass tip of a capillary over the sample.

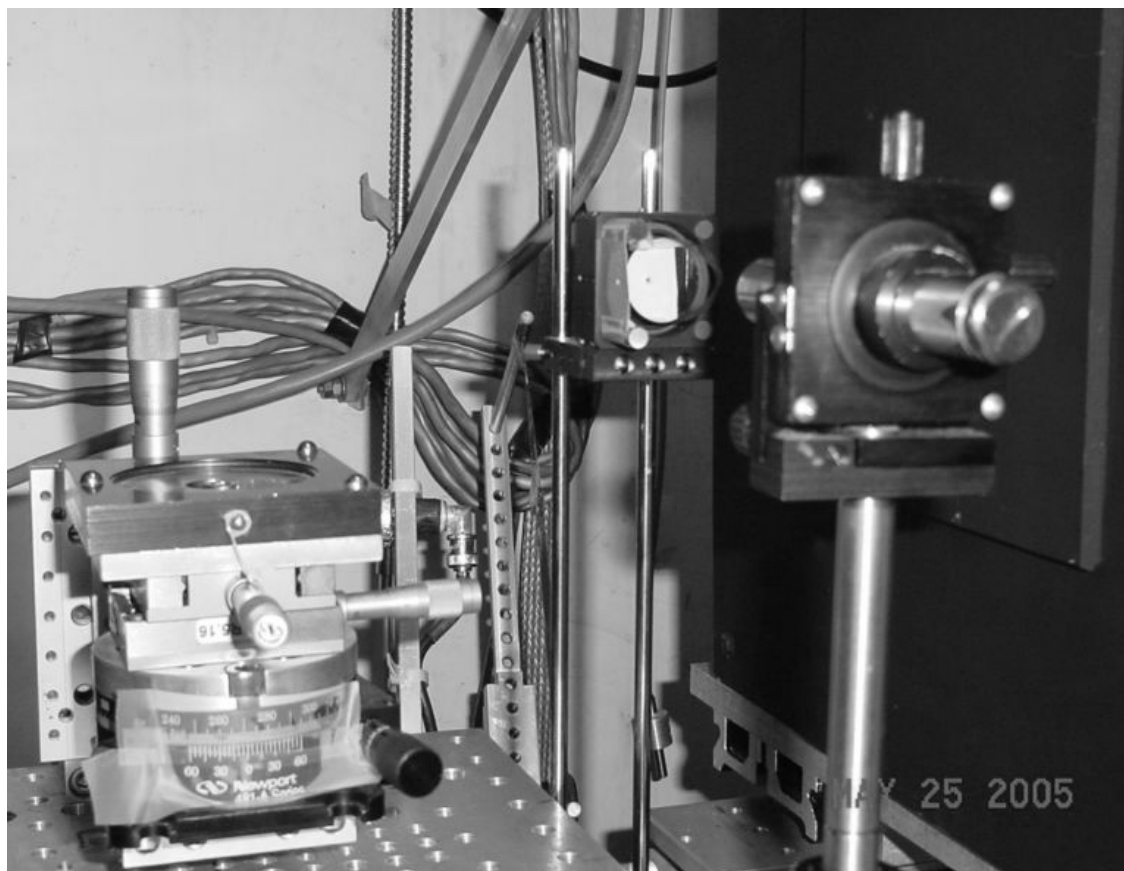


Figure 2.7: High pressure synchrotron experimental set up at CHESS. Sample stage is on the optical table and apparatus to center the collimated beam are shown.

While viewing under the microscope, the pressure transmission medium is injected through the capillary and the DAC is quickly closed to avoid evaporation of the liquid.

In order to determine the pressure in the DAC, several ruby chips were placed into the sample. Prior to and after each synchrotron scan, the wavelength of emission of the ruby chips was obtained using fluorescence spectroscopy. Emission positions were refined and peak widths recorded. The average ruby peak width was determined for each pressure. The error in peak widths was based on the standard deviation of peak widths before and after the experiment divided by  $\sqrt{2}$ .

Pressure is related to the wavelength,  $\lambda$ , of ruby fluorescence emission by the following equation:

$$P = (\lambda - 694.23) \times 2.746, \quad (6)$$

where 694.23 (nm) is the wavelength of ruby emission under ambient conditions and 2.746 is a conversion constant;  $\lambda$  is the emission wavelength and P is in units of GPa.

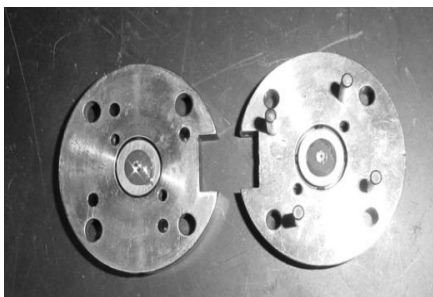


Figure 2.8: Two halves of unassembled four post DAC showing 1/3 carat diamonds on each half.

The ratio of pressure to the decrease in volume is referred to as the bulk modulus,  $B_0$ , and is a value often cited as a physical property of materials. Generally, low values of the bulk modulus indicate materials with soft lattice structures, while high values indicate relatively stiff lattices.<sup>13</sup> The inverse of the bulk modulus is compressibility.  $B_0$  is represented by the following relationship:

$$B_0 = \frac{\Delta P}{\frac{\Delta V}{V}} = \frac{\Delta P}{\ln V} \quad (7)$$

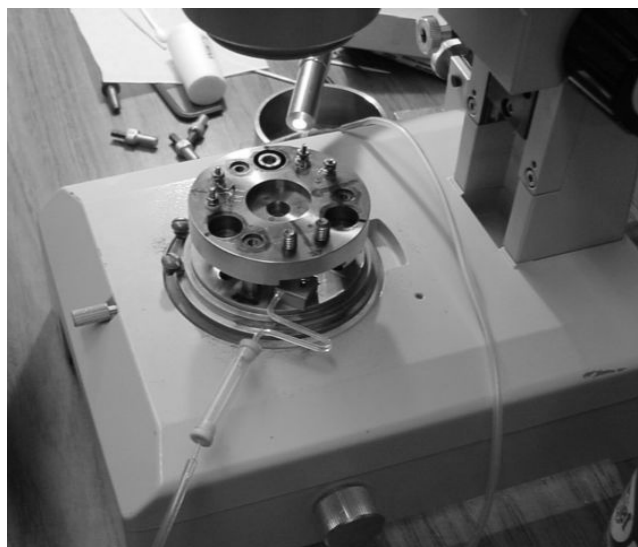


Figure 2.9: Assembled, but open, DAC receiving methanol/ethanol pressure transmitting medium via capillary tubing.

## 2.2 Transmission Electron Microscopy (TEM)

An HF\_2000 FE TEM (Oak Ridge National Labs; Dr. Jane Howe), was used for electron diffraction (ED) on powder samples. Preparation of samples for use with this TEM consisted of dry mounting powders on 3-mm grids of lacey carbon film supported

on 300-mesh Cu. The operating voltage was 200 kV and a CCD camera was used to record images and electron diffraction (ED) patterns.

The wavelength of the electron beam can be found from the following relationship:

$$\lambda = \frac{h}{\sqrt{2meV(1 + \frac{eV}{2mc^2})}}, \quad (8)$$

where  $h$  is Planck's constant ( $6.626 \times 10^{-34}$  Js),  $m$  is mass of an electron ( $9.109 \times 10^{-31}$  kg),  $e$  is electron charge ( $1.602 \times 10^{-19}$  C),  $V$  is operating voltage (J/C), and  $c$  is the speed of light in a vacuum ( $2.998 \times 10^8$  m/s).<sup>14</sup> Prior to use of the instrument, the operating voltage and the camera length are known values.

TEM/electron diffraction permits magnification of a single crystallite and the recording of diffraction spots from individual crystallites. An image of the diffraction serves as a template for determining the average distances between the beam center and reflections around it. The camera constant is related to Bragg's law, equation (1), by the following relationship,<sup>15</sup>

$$\text{Camera constant} = 2L\lambda = 2rd, \quad (9)$$

where  $L$  is the camera length,  $r$  is the average distance between reflections, and  $d$  is d-spacing.

The average camera constant for the HF\_2000 FE TEM was calculated to be 1032 Å·pixel and was determined from TEM/ED on a Si [110] calibrant; the camera length

was 0.4m.

### **2.3 Thermal Analysis**

Thermal expansion of materials can be quantified using powder x-ray methods or by dilatometry. The latter was not chosen as an option in the present research due to the limitation of the method to bulk measurements for changes in length, width, and height. Microscopic changes in the lattice constants of a material can be obtained by the use of the former.

The analysis of phase transitions in synthesized materials, on the other hand, is enhanced by the use of a number of thermal analysis methods. Such methods include Differential Scanning Calorimetry (DSC), Calorimetry, Thermal Gravimetric Analysis (TGA), and Differential Thermal Analysis (DTA). The choice of method depends on the information being sought. Calorimetry, for example, gives information to calculate heats of formation,  $\Delta H_f$ , while DSC and DTA supply information on the temperature at which heat is lost or gained by the sample under programmed ramping and heating. DSC and DTA differ in the manner in which a reference sample is treated. In DSC, the reference and sample are maintained at the same temperature. The measurement in DSC is the heat required to maintain the same temperature for the sample and reference. DTA, on the other hand, measures the difference in temperature between the sample and reference heated in the same furnace. TGA measures the mass loss during programmed heating of the sample. For most of the materials in the present research, important considerations included phase transition temperature, water content, and mass loss upon heating.

### **2.3.1 TG/DTA**

A Seiko SSC/5200 system TG/DTA 3200 instrumentation (Textiles Department at Georgia Institute of Technology) was used exclusively in the present research. The instrument permitted a programmed maximum temperature of 1200 °C and analyses could be carried out in inert atmosphere (argon or nitrogen gases) or air. Ramp rates and gas mixtures were varied depending upon the experiment being performed. Exotherm and endotherm curves from DTA measurements demonstrated the heat expelled by the sample or heat lost from the surroundings, respectively, which provided information for temperatures of crystallization and/or temperatures at which structural transitions may be occurring. This information could be compared to known thermal property data to assist with the characterization of samples, as well as to determine a process of heat treatments for the bulk sample. TG measurements provided information on mass loss due to water content in certain hydrated samples produced in this research.

### **2.4 MAS <sup>31</sup>P-NMR**

Solid state MAS (Magic Angle Spinning) <sup>31</sup>P-NMR (Nuclear Magnetic Resonance) was used for the characterization of unique crystallographic phosphorous groups (P-groups) for some samples in this work. The MAS technique makes it possible to obtain some structural information from solid materials.<sup>16</sup> A sample is rotated at a high velocity and at a critical angle, 54.74°, to the applied magnetic field. The instrument used was a Bruker DSX200 NMR spectrometer under the supervision of Dr. Johannes Leisen at Georgia Institute of Technology, School of Chemistry and Biochemistry. All samples had a spinning speed of 10 kHz. The 90 degree pulse length was adjusted to be 90

microseconds. Spectra were calibrated with respect to the chemical shift of ADP, ammonium dihydrogen phosphate, at 0 ppm. Direct polarization (DP) experiments were run where the  $^{31}\text{P}$  nucleus is excited directly using shortened pulses in order to eliminate very long relaxation times.

## **2.5 Software**

### **2.5.1 JADE**

Initial analysis of powder diffraction data was accomplished using JADE<sup>17</sup>. This software offers the ability to search for matching powder patterns from a database (PDF, powder diffraction file) containing thousands of patterns. In this manner, phase and impurity identification and the impact of synthesis method, temperature variation, insertion experiments, or other processes on samples can be readily observed.

### **2.5.2 Rietveld Refinement and LeBail Fitting**

Rietveld refinement<sup>18</sup> is a computational technique for crystal structure refinement and sample analysis using X-ray or neutron powder diffraction data. Refinements using the Rietveld method can result in the accurate determination of structural parameters (lattice constants, atomic positions, thermal parameters, and site occupancies) and quantitative phase content for samples consisting of mixed phases. The GSAS (General Structure Analysis System)<sup>9</sup> software, created by Allen Larson and Robert Von Dreele of Los Alamos National Laboratory, and a graphical interface linked to GSAS, EXPGUI,<sup>19</sup> developed by Brian Toby at the National Institute of Standards and

Technology (NIST), were used for the Rietveld analysis of powder patterns. TOPAS is another refinement package created by A. Coelho<sup>20</sup> for Rietveld, Le Bail, and simulated annealing processes and was also used for refinement.

A structural model is needed for Rietveld refinement with space group, cell parameters, and atomic positions. However, the LeBail method fits background, peak shape, lattice constants, and other parameters to provide a best fit to the experimental data without a structural model.<sup>21</sup>

### **2.5.3 CRYSFIRE and CHECKCELL**

CRYSFIRE<sup>22</sup> is a peak indexing package where peak positions from powder X-ray diffraction (for example, from JADE software) are input for purposes of obtaining potential unit cell parameters. The output from CRYSFIRE consists of lattice constants  $a$ ,  $b$ ,  $c$ ,  $\alpha$ ,  $\beta$ ,  $\gamma$ , volume, and a figure of merit (FOM) for each unit cell found by CRYSFIRE. The software itself is a combination of known algorithms, each used for indexing. DICVOL91,<sup>23</sup> TREOR,<sup>24</sup> ITO12,<sup>25</sup> TAUP,<sup>26</sup> KOHL,<sup>27,28</sup> and LZON<sup>29</sup> are some of the programs used within CRYSFIRE. All lattice types can be considered and the program has convenient algorithm parameter input and search options (volume, wavelength, intensity, two-theta ( $^\circ$ ) or d-spacing).

The output from CRYSFIRE is in the form compatible with CHEKCELL,<sup>30</sup> a program that permits, among other things, visualization of all potential unit cells compared to the peak positions input into CRYSFIRE. Along with the FOM from CRYSFIRE, CHEKCELL shows the ratio of the volume of each proposed cell to that of cell with the highest FOM ( $V/V_1$  parameter) calculated by CRYSFIRE. CHEKCELL

also contains the LePage program<sup>31</sup> for simple and supercell conversions.

#### **2.5.4 *Fit2d***

Fit2d is a program for manipulation of diffraction data from area detectors. It can be used to integrate images and give conventional powder diffraction patterns.<sup>11</sup>

## 2.6 References

1. Jenkins, R. S.; Snyder, R. L., *Introduction to Powder X-ray Diffraction*. John Wiley & Sons, Inc.: New York, 1996; Vol. 138.
2. Varga, T., *Synthesis and Characterization of Some Low and Negative Thermal Expansion Materials*. Georgia Institute of Technology, Atlanta, 2005.
3. Warren, B. E., *X-ray Diffraction*. Dover: New York, 1990.
4. David, W. I.; McCusker, L. B.; Baerlocher, Ch., *Structure Determination from Powder Diffraction Data*. Oxford University Press: New York, 2002.
5. Stout, G. H.; Jenkins, L. H., *X-ray Structure Determination - A Practical Guide*. 2<sup>nd</sup> ed.; John Wiley & Sons, Inc.: New York, 1989.
6. Schwartz, L. H.; Jerome B., *Diffraction From Materials*. 2nd Edition ed.; Springer-Verlag: Berlin, 1987.
7. Skoog, D. A. H.; Nieman, T., *Principles of Instrumental Analysis*. Fifth ed.; Saunders College Publishing: Philadelphia, 1998.
8. Hammersley, A. P.; Svensson, S. O.; Hanfland, M.; Fitch, A. N.; Hausermann, D., Two-dimensional detector software: From real detector to idealised image or two-theta scan. *High Pressure Research* 1996, 14, 235-248.
9. Larson, A. C.; Von Dreele, R. B., *GSAS - General Structure Analysis System*. Report LA-UR-86-748: Los Alamos Laboratory, 1987.
10. Lind, C.; VanDerveer, D. G.; Wilkinson, A. P.; Chen, J.; Vaughan, M. T.; Weidner, D. J., New high pressure form of the negative thermal expansion materials zirconium molybdate and hafnium molybdate. *Chem. Mater.* 2001, 13, 487-490.
11. Hammersley, A. P.; Svensson, S. O.; Hanfland, M.; Fitch, A. N. *Internal Report ESRF98HA01T Reference Manual V 3.1 Fit2D v 9.129, 9.129*; ERSF Grenoble from High Pressure Res. (1996) 14, 235: Grenoble, 1998.
12. *JADE for XRD Pattern Processing, 7.0*; Materials Data, Inc.: Livermore, CA, 1995-2005.
13. Lundin, U.; Fast, L.; Nordström, L.; Johansson, B., Transition-metal dioxides with a bulk modulus comparable to diamond. *Physical Review B* 1998, 57, (9), 4979 - 4982.
14. Williams, D. B., *Transmission Electron Microscopy Basics I*. Plenum Press: New York, 1996.

15. Williams, D. B., *Transmission Electron Microscopy Diffraction II*. Plenum Press: New York, 1996.
16. West, A. R., *Basic Solid State Chemistry*. 2nd Edition ed.; John Wiley & Sons, Ltd.: West Sussex, 1999.
17. Materials Data, I. *JADE Pattern Processing Identification and Quantification*, Materials Data, Inc.: Livermore, CA, 1995-2005.
18. Rietveld, H. M., A Profile Refinement Method for Nuclear and Magnetic Structures. *Journal of Applied Crystallography* 1969, 2, 65-71.
19. Toby, B. H., EXPGUI, a graphical user interface for GSAS. *Journal of Applied Crystallography* 2001, 34, 210-213.
20. Coelho, A. A., Whole-profile structure solution from powder diffraction data using simulated annealing. *Applied Crystallography* 2000, 33, 899-908.
21. Le Bail, A. D. H.; Fourquet, J. L., Ab-initio structure determination of  $\text{LiSbWO}_6$  by X-ray powder diffraction. *Mat. Res. Bull.* 1988, 23, 447-452.
22. Shirley, R. *The CRYSFIRE System for Automatic Powder Indexing: User's Manual*, The Lattice Press  
31 Guildford Park Avenue: Guildford, Surrey GU2 7 NL, England, 2000.
23. Louër, D., Advances in powder diffraction analysis. *Acta Cryst. A* 1998, 54, 922-933.
24. Werner, P. E., On the Determination of Unit-Cell Dimensions from Inaccurate Powder Diffraction Data. *J. Appl. Cryst.* 1976, 9, 216-219.
25. Visser, J. W., A Fully Automatic Program for Finding the Unit Cell from Powder Data. *J. Appl. Cryst.* 1969, 2, 89-95.
26. Taupin, D., A Powder-Diagram Automatic-Indexing Routine. *J. Appl. Cryst.* 1973, 6, 380-385.
27. Kohlbeck, F. H., Indexing Program for Powder Patterns Especially Suitable for Triclinic, Monoclinic and Orthorhombic Lattices. *J. Appl. Cryst.* 1976, 9, 28-33.
28. Kohlbeck, F. H., Trial and error indexing program for powder patterns of monoclinic substances. *J. Appl. Cryst.* 1978, 11, 60-61.
29. Shirley, R. L., New powder indexing programs for any symmetry which combine grid-search with successive dichotomy. *Acta Cryst. A* 1978, 34, S382.

30. Laugier, J., *LMGP-Suite of Programs for the interpretation of X-ray Experiments*, ENSP/Laboratoire des Materiaux et du Genie Physique: Saint Martin d'Herès, France.
31. Spek, T. M., *ClePag 15*, 1.5; Adapted for CRYSFIRE by R. Shirley: 2002.

## CHAPTER 3

### LOW TEMPERATURE SYNTHESIS AND CHARACTERIZATION OF SOME $A^{IV}M^V_2O_7$ COMPOUNDS: $ZrP_2O_7$ , $ZrV_2O_7$ , $CeP_2O_7$ , AND $PbP_2O_7$

#### 3.1 Introduction

Low temperature synthesis processes include hydrolytic sol-gel, non-hydrolytic sol-gel, acid reflux, acid digestion, and mild hydrothermal or autoclave methods. They have been used extensively by researchers to prepare a variety of materials. All the methods mentioned above are used in the present research and some are described more fully in the sections that follow.

It is important to note that in solid state syntheses, the products are limited by the requirement for thermodynamic stability at high temperatures, while low temperature methods can be used to make materials that are only kinetically stable. The raw, initial product from low temperature methods is often an amorphous sol, gel, or powder, or a crystalline precursor (often a hydrate). The desired final crystalline product can sometimes be obtained by firing this initial product at temperatures much lower than used in solid state syntheses ( $< 1000^\circ\text{C}$ ) and with much shorter firing times (a few hours or several hours).

The final products of low temperature synthesis methods, as well as those obtained in most solid state methods for  $A^{IV}M^V_2O_7$  compounds and other low and negative thermal expansion families, are usually polycrystalline powders with very small crystallites, which cannot be characterized by single crystal X-ray diffraction (Section 2.1).

Many known low and negative thermal expansion compounds can be produced by low temperature methods. Moreover, the synthesis method and/or starting materials can impact the structure and/or the crystallization temperature of the desired product. Examples of solid state and low temperature methods for many  $A^{IV}M^V_2O_7$  compounds are discussed in Section 1.2.2, where the method of synthesis and/or starting materials sometimes resulted in a different precursor or in lower temperatures of crystallization for some compounds. The benefit of having a variety of synthesis methods from which to choose for some low positive and NTE materials is the potential for the production of new low positive, zero, or negative thermal expansion materials.

One focus of the research presented in this chapter involves the use of non-hydrolytic sol-gel methods (Section 3.1.1) and mild autoclave techniques and/or starting materials previously unexplored in the literature for some known  $A^{IV}M^V_2O_7$  compounds to determine whether or not successful preparation results in altering crystallization temperatures. Hydrolytic sol-gel techniques are briefly discussed in Section 3.1.1 for contrast to the non-hydrolytic sol-gel method.

Various synthesis methods for  $ZrP_2O_7$  and  $ZrV_2O_7$  have been discussed previously (Section 1.2.2), however, there have been no reports in the literature for the synthesis of  $ZrP_2O_7$  and  $ZrV_2O_7$  using the non-hydrolytic sol-gel method. The successful production of these compounds is described in Sections 3.2 and 3.3. In addition, the direct synthesis of  $ZrP_2O_7$  from separate zirconium and phosphorous containing reagents is described for the first time using mild autoclave conditions (Section 3.4).

Low temperature acid reflux was used to prepare  $CeP_2O_7$  (Section 3.5) and

PbP<sub>2</sub>O<sub>7</sub><sup>1</sup> (Section 3.6); other methods, such as acid digestion and mild autoclave routes for CeP<sub>2</sub>O<sub>7</sub> had limited success and will not be described.

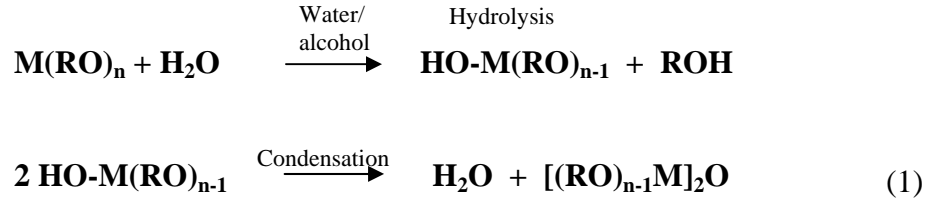
Another focus of the research presented in this chapter is the characterization of thermophysical and other properties for CeP<sub>2</sub>O<sub>7</sub> and PbP<sub>2</sub>O<sub>7</sub>. Using instrumental methods and data analyses described in Chapter 2, previously published crystallographic data for CeP<sub>2</sub>O<sub>7</sub> are found to have been in error (Section 3.5.2). In addition, thermal expansion data for CeP<sub>2</sub>O<sub>7</sub> and PbP<sub>2</sub>O<sub>7</sub>, and the results of high pressure studies on CeP<sub>2</sub>O<sub>7</sub>, are presented for the first time (Sections 3.5.2.3 and 3.6.2, and Section 3.5.2.2, respectively).

### ***3.1.1 Hydrolytic and Non-hydrolytic Sol-Gel Synthesis***

Hydrolytic sol-gel methods have been employed in the preparation of many metal oxide ceramics and glasses resulting in highly homogeneous products,<sup>2,3</sup> including several A<sup>IV</sup>M<sup>V</sup><sub>2</sub>O<sub>7</sub> compounds and representative solid solutions of this family (Sections 1.2.2 and 1.2.3).

Hydrolytic methods encompass two routes that depend on starting materials: an aqueous route and an organic route.<sup>4</sup> In the aqueous route, metal salts are dissolved in water (and hydrolyzed). Condensation can be initiated with the addition of a base to a low valence aquo-cation or with an acid added to a high valence oxy-anion.<sup>3,4</sup> In the organic route, metal alkoxides, M(RO)<sub>n</sub>, are usually dissolved in alcohol or some other organic solvent. Hydrolysis and condensation reactions occur with the introduction of water. With either route, the reaction leads to the formation of an amorphous sol or gel, a three-dimensional network of colloidal particles with metal-oxygen-metal (or M-O-M) linkages. The reactions can be accomplished at room temperature, with the ripening of

the sol-gel over a period of days, or above room temperature. A general scheme for the organic route is presented in scheme (1) and shows hydrolysis and condensation reactions:



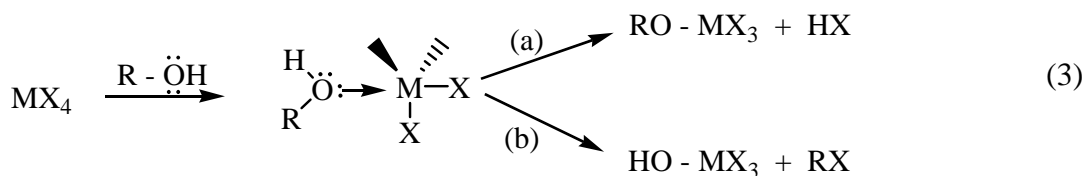
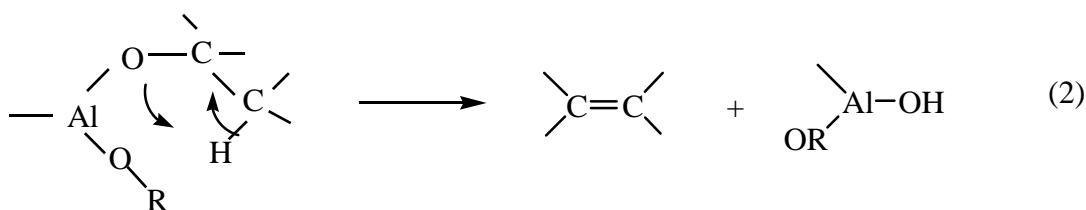
Crystalline phases are subsequently obtained by firing of the dried amorphous sols or gels. There are many variations on the organic hydrolytic sol-gel route that do not include the use of metal alkoxides, but the use of starting materials such as metal salt hydrates dissolved in alcohol along with a metal salt dissolved in water.<sup>2</sup>

Advantages of the hydrolytic method include the possibility of using a wide variety of starting materials, water soluble and organic solvent soluble, as well as the synthetic product sol-gel having the potential to serve as building blocks for multi-component composites or solid solutions. Disadvantages of hydrolytic routes include the difficulty of controlling rapid hydrolysis reactions with metal alkoxides, thus affecting the homogeneity of the sol-gel product. This can result in direct precipitation rather than the formation of gels.<sup>5</sup> Sometimes materials unobtainable by conventional ceramic methods can be realized with hydrolytic sol-gel techniques. Amorphous gels obtained are calcined resulting in inorganic oxide structures.

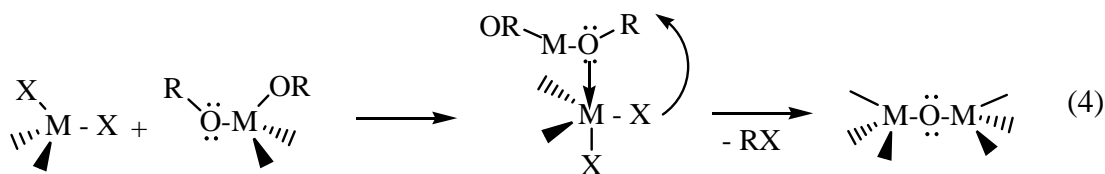
Non-hydrolytic sol-gel methods eliminate the hydrolysis reactions of the

hydrolytic sol-gel method, change the experimental conditions and reaction mechanisms, and can include catalysts in the formation of homogeneous sol-gels. There are two routes in the non-hydrolytic method: one involves hydroxylation and the other involves aprotic condensation reactions.

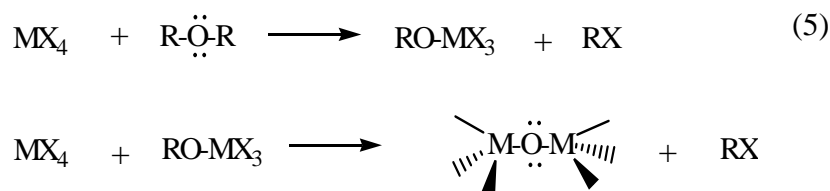
Hydroxylation involves the thermal decomposition of metal alkoxides with the



production of metal alkoxide hydroxide and an alkene, scheme (2), or the action of certain alcohols on metal halides, schemes 3 (a) and (b).<sup>6</sup> Paths (a) and (b) in scheme (3) both begin with a lone pair of electrons from oxygen coordinating to the metal center followed by cleavage of either the alkoxy group (a), or hydroxyl group (b). Whether (a) or (b) is the directed pathway depends upon the halide. For example, the use of chloride ion favors nucleophilic attack on the carbon group, path (b).



Aprotic condensation is represented by the pathway shown in scheme (4). In this scheme, the initial reaction between metal halides and metal alkoxides occurs at room temperature and involves the redistribution of halide and alkoxy ligands in a strongly exothermic reaction leading to the formation of a mixture of halide alkoxides. Some condensation reactions occur (the elimination of R – X in scheme (4)), but are very slow at room temperature. Continuation of direct condensation requires heating at temperatures between 80-150 °C. The rate of condensation reactions affects the homogeneity of the products (random mixtures of M-O-M linkages).



Scheme (5) shows a possible two step process using ether as the oxygen donor with metal halides. In the first step, oxygen coordinates with the metal center of the halide resulting in a mixed alkoxy metal halide and condensation with the loss of RX. In the second step, the mixed alkoxy metal halide reacts with another metal halide resulting in condensation and the creation of M-O-M links. According to Vioux, further condensations in scheme (5) proceed by the same pathway shown in scheme (4).<sup>6</sup> Ester elimination, RCOOR, is another type of aprotic condensation reaction that involves metal

or silicon carboxylates and metal alkoxides,  $M(OR)$ , as starting materials resulting in the formation of oxygen bridges between metal atoms in an M-O-M network.<sup>6</sup>

Amorphous gels or powders are obtained by low-temperature treatments of the contents in sealed vessels, and crystalline products are obtained often after heat treatments of the gels or powders at higher temperatures. Compounds prepared by the non-hydrolytic sol-gel technique include several mixed metal oxides, such as  $ZrTiO_4$ ,<sup>7</sup>  $SiO_2-ZrO_2$  and  $SiO_2-TiO_2$  glasses,<sup>8,9</sup> and  $\beta-Al_2TiO_5$  (a pseudo-brookite phase),<sup>10,11</sup>  $Nb_2O_5$ ,<sup>5</sup> and  $Al_6Si_2O_{13}$ ;<sup>12</sup> metal oxides, such as  $Al_2O_3$ ,<sup>6,13,14</sup>  $TiO_2$ ,<sup>13,15</sup>  $BPO_4$ ,<sup>16</sup> and, from the work of Arnal, et al.,  $MoO_3$ ,  $ZrO_2$ ,  $WO_3$ ,  $\alpha-Fe_2O_3$  and  $V_2O_5$ ,<sup>5</sup>  $WO_3$ ,<sup>17</sup> and  $SiO_4$ ;<sup>18</sup> a polymorph of  $ZrW_2O_8$ ;<sup>19</sup> and NASICON,  $Na_3Zr_2Si_2PO_{12}$ .<sup>20</sup>

One advantage of using non-hydrolytic sol-gel methods when compared to hydrolytic sol-gel routes is more control over the reaction by eliminating hydrolysis. However, solubility and reagent cost limit the utility of the method.

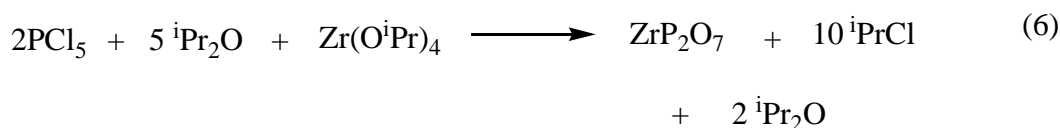
### **3.1.2 Autoclave Techniques**

Hydrothermal methods sometimes make use of expensive, high pressure apparatus to prepare compounds or single crystals.<sup>21</sup> Autoclave methods can be described as low to moderate pressure hydrothermal processes that utilize relatively inexpensive pressure vessels under autogenous pressure, for example, Paar bombs. Generally, the maximum processing temperature for mild autoclave methods using Paar bombs is 200 - 250°C.

## **3.2 Non-hydrolytic Sol-Gel Synthesis of $ZrP_2O_7$ (KMW02 and KMW04)**

This work was undertaken to see if  $\text{ZrP}_2\text{O}_7$  could be made at lower temperatures than those typically reported in the literature and to see if non-hydrolytic sol-gel synthesis might offer a general route to  $\text{A}^{\text{IV}}\text{M}^{\text{V}}_2\text{O}_7$  compounds (Section 1.2.2).

Samples were prepared by the method outlined by Vioux,<sup>6, 21</sup> Corriu,<sup>13, 22</sup> and used by Wilkinson and Lind,<sup>19</sup> and involved a variation of schemes (3), (4), and (5), Section 3.1.2, in which ether is an oxygen donor and different metals are used as starting materials. An idealized chemical reaction for the synthesis of  $\text{ZrP}_2\text{O}_7$  is illustrated in scheme (6).



### 3.2.1 Experimental

#KMW04: 1.117 g (2.88 mmol)  $\text{Zr}(\text{O}^i\text{Pr})_4 \cdot \text{}^i\text{PrOH}$  (Strem Chemicals) was reacted with 1.416 g (6.8 mmol)  $\text{PCl}_5$  (Strem Chemicals) and 14.2 mmol  $\text{}^i\text{Pr}_2\text{O}$  (anhydrous, Aldrich). Both  $\text{PCl}_5$  and  $\text{Zr}(\text{O}^i\text{Pr})_4 \cdot \text{}^i\text{PrOH}$  were handled in an argon atmosphere. The zirconium and phosphorous precursors were placed into a glass ampule and vial, respectively, and sealed. Tetrahydrofuran (anhydrous, Fisher), 8.0 mL, was transferred to the vial containing the zirconium precursor under nitrogen gas flow followed by the addition of 2.0 mL of  $\text{}^i\text{Pr}_2\text{O}$ .  $\text{CHCl}_3$  (anhydrous, Aldrich), 17.0 mL, was transferred to the vial containing  $\text{PCl}_5$  under nitrogen gas flow. The contents of the vials were stirred until dissolution and a clear, colorless solution was observed. Under nitrogen gas flow, the contents of the glass vial containing zirconium/THF/ $\text{}^i\text{Pr}_2\text{O}$  were withdrawn and injected

through the seal of the glass ampule containing  $\text{PCl}_5/\text{CHCl}_3$ . The glass ampule was observed to be warm to the touch and an ice bath was placed under it to cool the reaction mixture. The mixture was stirred for one hour. The contents of the glass ampule were frozen using liquid  $\text{N}_2$ . The ampule was evacuated, flame sealed, and then heated at  $110^\circ\text{C}$  for seven days.

After heating, the ampule, containing a clear gel-like product, was frozen in liquid  $\text{N}_2$  and opened. The sample was recovered using a glass frit funnel, washed with  $\text{CHCl}_3$ , and allowed to dry in air. The raw powder was subjected to the following series of heat treatments in a preheated furnace:  $600^\circ\text{C}$  for four hours and  $900^\circ\text{C}$  for 15 hours, resulting in a black granular powder, then  $950^\circ\text{C}$  for one hour (gray granular powder), and finally  $975^\circ\text{C}$  for 23 hours resulting in a white powder. Yield of raw powder, 0.9535 g.

Zirconium content in  $\text{Zr}(\text{O}^i\text{Pr})_4 \cdot ^i\text{PrOH}$  was determined by mass difference based on the residual metal dioxide after heating at  $1000^\circ\text{C}$  for four hours.

Laboratory powder XRD using a Scintag X1 diffractometer was used to characterize the crystalline products.

*KMW02* was prepared in the same manner as *KMW04*, with the same amounts of precursors and diisopropyl ether, except the volume of  $\text{CHCl}_3$  used was 15.0 mL instead of 17 mL. The raw product from the synthesis and the crystalline product after heat treatment to  $900^\circ\text{C}$  were used in solid state MAS  $^{31}\text{P}$ -NMR. The sample was subjected to a different series of heat treatments than those performed for *KMW04* ( $400^\circ\text{C}$  for 13 hours and  $900^\circ\text{C}$  for 16 hours).

### **3.2.2 Results and Discussion**

The raw products from the syntheses were amorphous white powders. Sample *KMW02* crystallized to  $\text{ZrP}_2\text{O}_7$  around  $900^\circ\text{C}$  after 16 hours; however, the powder diffraction pattern (not shown) for this sample indicates it was not fully crystallized when compared to that for *KMW04*, which resulted in  $\text{ZrP}_2\text{O}_7$  after heat treatment at  $975^\circ\text{C}$  for 23 hours.

JADE software (Section 2.5.1) was used to identify the powder pattern for sample *KMW04*, Figure 3.1, as that of room temperature cubic  $\text{ZrP}_2\text{O}_7$ . The inset in Figure 3.1 highlights the identification of some of the weak peaks associated with the superlattice of  $\text{ZrP}_2\text{O}_7$ .

Solid state MAS  $^{31}\text{P}$ -NMR was performed on both the synthetic product and the crystalline pyrophosphate from sample *KMW02*. In Figure 3.2, the spectrum of the

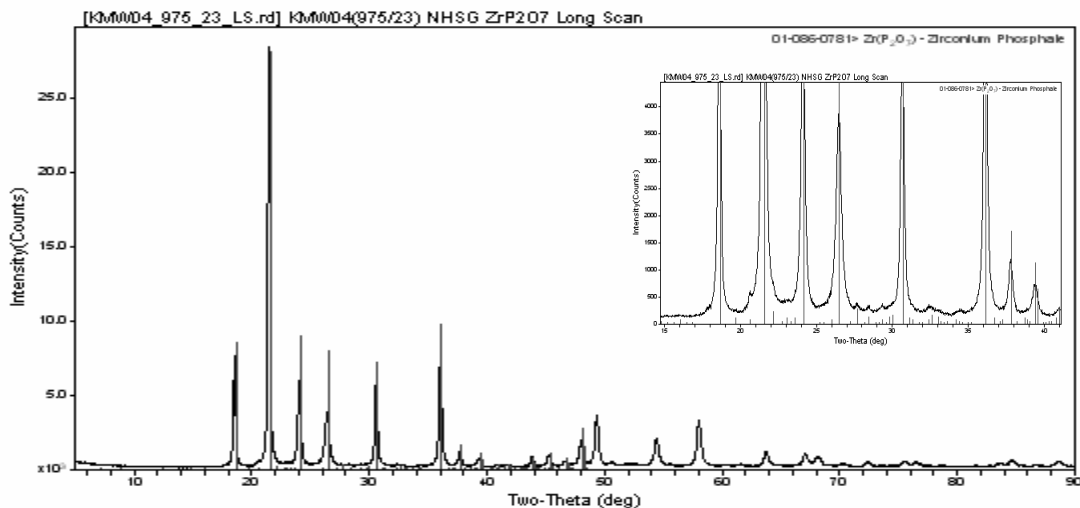


Figure 3.1: JADE identification of supercell, room temperature structure for  $\text{ZrP}_2\text{O}_7$  prepared by non-hydrolytic sol-gel methods (*KMW04*). Inset shows weak supercell peaks of powder pattern matching those in the PDF database for the compound.

synthetic product is shown with one large peak around -23 ppm and two smaller, broader peaks indicating at least three different phosphate environments. It is notable that none of these peaks occurs at a similar chemical shift to those seen in MAS  $^{31}\text{P}$ -NMR for fully crystallized  $\text{ZrP}_2\text{O}_7$ , shown in Figure 3.3, where experimental data was close match to that from the work of Korthius, et al., which reported at least eleven phosphate groups.<sup>23</sup>

In the non-hydrolytic sol-gel synthesis of  $\text{ZrP}_2\text{O}_7$  (*KMW04*), the product was observed to crystallize at  $975^\circ\text{C}$ , a temperature in the higher range of crystallization temperatures for  $\text{ZrP}_2\text{O}_7$  cited in published literature and synthesized by other methods. The observed crystallization temperature in this research is below the temperature of  $1200^\circ\text{C}$  cited by Harrison, et al., in the solid state synthesis of  $\text{ZrP}_2\text{O}_7$ ,<sup>24</sup> and higher than the range of temperatures observed by Clearfield and Stynes ( $230 - 920^\circ\text{C}$ ), where the concentration of phosphate ion was considered crucial to the crystallization temperature.<sup>25</sup> Not achieving low crystallization temperatures using non-hydrolytic

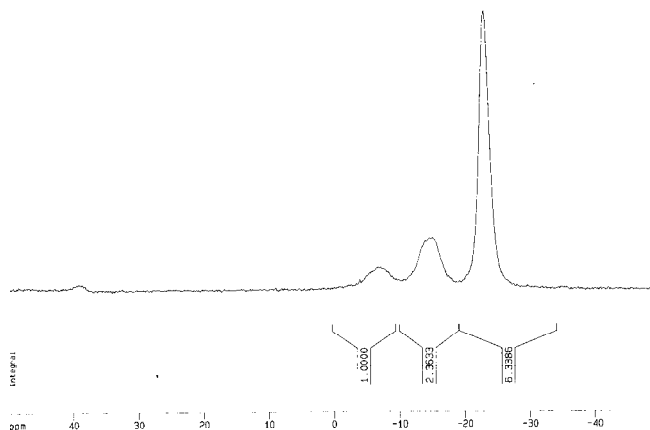


Figure 3.2: MAS  $^{31}\text{P}$ -NMR of *KMW02*, the synthetic product.

methods could indicate non-homogeneity of the sol-gel. Though heterogeneous sols or gels sometimes result in phase separation at low temperatures, no phase separation was observed in powder XRD after heat treatments. All samples were found to be amorphous or partially crystallized  $\text{ZrP}_2\text{O}_7$  up until 975 °C. According to Corriu, et al., homogeneity of resultant sol-gels depends on the relative rates of condensation of the metal alkoxide/metal halide intermediates in ligand exchange non-hydrolytic reactions.<sup>13</sup> The choice of precursors, therefore, could affect the homogeneity of the sol-gel, where condensation rates are not of the same order. Use of  $\text{PCl}_5$ , for example, and zirconium isopropoxide in these syntheses, rather than other phosphorus or zirconium sources, could have resulted in the observed high crystallization temperature for zirconium pyrophosphate.

Many published wet chemical, low temperature methods, some of which are also used in this research, involve the dehydration of the precursor  $\text{Zr}(\text{HPO}_4)_2 \cdot \text{H}_2\text{O}$ , synthesized from a-ZrP sol, to obtain zirconium pyrophosphate after firing. The non-hydrolytic sol-gel method resulting in the preparation of  $\text{ZrP}_2\text{O}_7$  eliminates the step

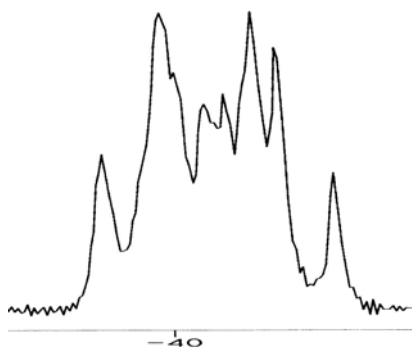


Figure 3.3: MAS  $^{31}\text{P}$ -NMR experimental results for crystalline  $\text{ZrP}_2\text{O}_7$  (KMW02), horizontal scale is in ppm.

involving the synthesis of the precursor, but does not result in a lower crystallization temperature for  $\text{ZrP}_2\text{O}_7$ , except when compared to solid state methods. The value of synthesizing  $\text{ZrP}_2\text{O}_7$  by non-hydrolytic sol-gel method is its inclusion into the category of compounds that can be obtained by the method and its potential use as a precursor for solid-solutions with other  $\text{A}^{\text{IV}}\text{M}^{\text{V}}_2\text{O}_7$  compounds or other compounds in composites that could be synthesized using the method.

### **3.3 Non-hydrolytic Sol-Gel Synthesis of $\text{ZrV}_2\text{O}_7$**

This work was undertaken to see if  $\text{ZrV}_2\text{O}_7$  could be made at lower temperatures than those typically reported in the literature and to see if non-hydrolytic sol-gel synthesis might offer a general route to  $\text{A}^{\text{IV}}\text{M}^{\text{V}}_2\text{O}_7$  compounds (Section 1.2.2).

Prior to preparing  $\text{ZrV}_2\text{O}_7$ , the preparation of  $\text{V}_2\text{O}_5$  by non-hydrolytic sol-gel method was examined. Three vanadium precursors were tested ( $\text{VCl}_4$ ,  $\text{VO}(\text{OC}_3\text{H}_7)_3$ , and  $\text{VOCl}_3$ ).

#### **3.3.1 Non-Hydrolytic Sol-Gel Synthesis of $\text{V}_2\text{O}_5$ (KMW11, KMW14, KMW15, and KMW19)**

##### **3.3.1.1 Experimental**

*KMW15*: Non-hydrolytic methods as used for the synthesis of  $\text{ZrP}_2\text{O}_7$  (Section 3.2.1) were used in the production of vanadium pentoxide. For *KMW15*,  $\text{VOCl}_3$  (Aldrich), 3.5180 g (20.3 mmol), was dissolved in 15.0 mL  $\text{CHCl}_3$  (anhydrous, Aldrich) in a sealed glass ampule.  $^{\text{I}}\text{Pr}_2\text{O}$  (anhydrous, Aldrich), 4.29 mL (31.2 mmol), was added.

No evolution of heat was observed while stirring for two hours. The glass ampule was evacuated, sealed, and heated at 135°C for seven days. A dark blue brittle film was obtained. The film was ground for powder XRD. Heat treatment at 500 °C for two hours resulted in a pale orange powder of V<sub>2</sub>O<sub>5</sub>. Yield raw film: 1.0044 g.

### 3.3.1.2 Results and Discussion

Vanadium precursors, VCl<sub>4</sub> and VO(OC<sub>3</sub>H<sub>7</sub>)<sub>3</sub>, were determined to be inadequate for obtaining V<sub>2</sub>O<sub>5</sub>. Successful synthesis of V<sub>2</sub>O<sub>5</sub> (*KMW15*) was achieved using non-hydrolytic methods with VOCl<sub>3</sub>; however, different heating temperatures of the samples may have made a difference in the type of raw product obtained. In the synthesis of V<sub>2</sub>O<sub>5</sub>, large blue crystals (*KMW11*) were obtained as raw, synthetic product using VOCl<sub>3</sub> in an ampule heated at 110°C for 7 days. Subsequently exposed to atmosphere during drying procedures, results from single crystal XRD on *KMW11* indicate the product was not crystalline in nature, but amorphous. *KMW14* and *KMW19*, remakes of *KMW11* and both heated at 110°C for 7 days, also provided blue crystals. Those obtained from *KMW14* were frozen immediately upon opening the glass ampule, rather than allowing the crystals to dry in air or using heat treatment to dry them further. The blue crystals were withdrawn from the clear, amber solvent in the ampule immediately upon opening using a Pasteur pipet and transferred onto a half glass tube covered with a filter paper over which argon gas (Ar gas was cooled with liquid N<sub>2</sub>) flowed in order to isolate and mount a crystal. With the help of Dr. Don Vanderveer in the GA Tech School of Chemistry and Biochemistry, single crystal XRD was performed within minutes of this process and the results suggested a small unit cell, probably orthorhombic, but with twinning. After

leaving the crystal in open air for several minutes, single crystal XRD revealed a loss of structure. *KMW19*, prepared with  $\text{VOCl}_3$ , excess ether, reduced volume of solvent  $\text{CHCl}_3$ , and heated at  $110^\circ\text{C}$  for seven days, resulted in dark blue crystals. An unidentified mixed phase crystalline material was observed for this sample (using powder XRD) after heating the crystals at  $300^\circ\text{C}$  for two hours.

Using  $\text{VOCl}_3$  in a subsequent synthesis attempt and heating the reaction ampule at  $135^\circ\text{C}$  for seven days (*KMW15*, Section 3.3.1.1) resulted in an amorphous, dark blue film deposited on the bottom and sides of the ampule, which was subsequently ground for heat treatments. Yellow/orange  $\text{V}_2\text{O}_5$  was obtained after heat treatment at  $500^\circ\text{C}$  for two hours. The key to this successful synthesis may have been the temperature at which the ampule was heated, which was above the boiling point of  $\text{VOCl}_3$ ,  $126.7^\circ\text{C}$ . Previous attempts, those resulting in blue crystals, were probably not at high enough temperatures for  $\text{VOCl}_3$  and diisopropyl ether condensation rates to be effective.

### **3.3.2 *Non-hydrolytic Sol-Gel Synthesis of $\text{ZrV}_2\text{O}_7$ (KMW23, KMW24, KMW25, KMW26, KMW27, KMW38)***

With the production of  $\text{V}_2\text{O}_5$  via the non-hydrolytic sol-gel method, the synthesis of  $\text{ZrV}_2\text{O}_7$  was examined using a similar method and starting materials.

#### **3.3.2.1 *Experimental***

*KMW23*: Non-hydrolytic methods used in the synthesis of  $\text{V}_2\text{O}_5$  were used (Section 3.3.1.1) in the synthesis of  $\text{ZrV}_2\text{O}_7$ .  $\text{Zr}(\text{O}^i\text{Pr})_4 \cdot ^i\text{PrOH}$  (Strem), 1.3840 g (4.23 mmol), was dissolved in 8.0 mL THF (anhydrous, Fisher) in a septa-sealed glass vial.

The vanadium precursor, 1.460 g (8.42 mmol)  $\text{VOCl}_3$  (Aldrich) was diluted with 10.0 mL  $\text{CHCl}_3$  (anhydrous, Aldrich) in a septa-sealed ampule and then transferred to the vial containing  $\text{Zr}(\text{O}^i\text{Pr})_4 \cdot ^i\text{PrOH}$  in THF. Anhydrous  $^i\text{Pr}_2\text{O}$  (Aldrich), 2.0 mL (14.2 mmol), was added to the vial containing  $\text{Zr}(\text{O}^i\text{Pr})_4 \cdot ^i\text{PrOH}$  in THF and  $\text{VOCl}_3$  in  $\text{CHCl}_3$ . No evolution of heat was observed while the contents of the reaction vessel were stirred for 1.5 hours. The fire-sealed glass ampule was placed into a preheated oven at  $135^\circ\text{C}$  for seven days. The raw product was a black powder. Heat treatments at  $300^\circ\text{C}$  for two hours and at  $100^\circ\text{C}$  increments starting at  $400^\circ\text{C}$  up to  $600^\circ\text{C}$ , each for one hour, resulted in golden yellow, crystalline  $\text{ZrV}_2\text{O}_7$  powder at  $600^\circ\text{C}$ , verified by powder XRD; however, a more crystalline compound was observed using powder XRD after heating at  $700^\circ\text{C}$  for one hour. Both the  $600^\circ\text{C}$  and  $700^\circ\text{C}$  powder patterns are matched to that of room temperature  $\text{ZrV}_2\text{O}_7$ . Yield raw powder: 1.1471 g. Percent mass loss (TG/DTA;  $25 - 738^\circ\text{C}$ ): 38.59%. Percent mass loss (heat treatments): 47.6%.

### 3.3.2.2 Results and Discussion

Powder XRD patterns for sample *KMW23* revealed the dominant crystalline phase to be  $\text{ZrV}_2\text{O}_7$  after heating at  $700^\circ\text{C}$  with a minor impurity phase identified using JADE and PDF database (Section 2.51) to be  $\text{V}_2\text{O}_5$ . The impurity was observed, however, at temperatures as low as  $300^\circ\text{C}$ . Figure 3.4 shows room temperature powder XRD patterns for the raw product and after each heat treatment ( $300 - 700^\circ\text{C}$ ). Onset of crystallization for *KMW23* was at  $500^\circ\text{C}$ ; the powder XRD pattern shows weak peaks along with a broad hump in the powder scan. At  $600^\circ\text{C}$ , the sample appeared to be well crystallized, but, when comparing this powder scan to that at  $700^\circ\text{C}$ , peak intensities increase and the

impurity peaks ( $V_2O_5$ ) decrease in intensity or disappear at the higher temperature.

Arrows in Figure 3.4 point to impurity peaks in the powder pattern for  $ZrV_2O_7$  after heating at  $700^\circ\text{C}$ .  $V_2O_5$  is not an unusual impurity in  $ZrV_2O_7$  preparations. Khosrovani, et al. reported  $V_2O_5$  impurity at room temperature and at  $450^\circ\text{C}$  in high resolution neutron diffraction experiments.<sup>26</sup>

Both the crystallization and degradation temperatures observed for the sample prepared in this study are considered to be within the range of synthesis and degradation temperatures reported in literature for  $ZrV_2O_7$ . In a 1976 work, Baran reports the solid state reaction between  $ZrO_2$  and  $V_2O_5$  at  $650^\circ\text{C}$  for 80 hours with intermittent grindings.<sup>27</sup> Using  $ZrOCl_2 \cdot 8H_2O$ , rather than  $ZrO_2$ , and  $NH_4VO_3$ , rather than  $V_2O_5$ ,

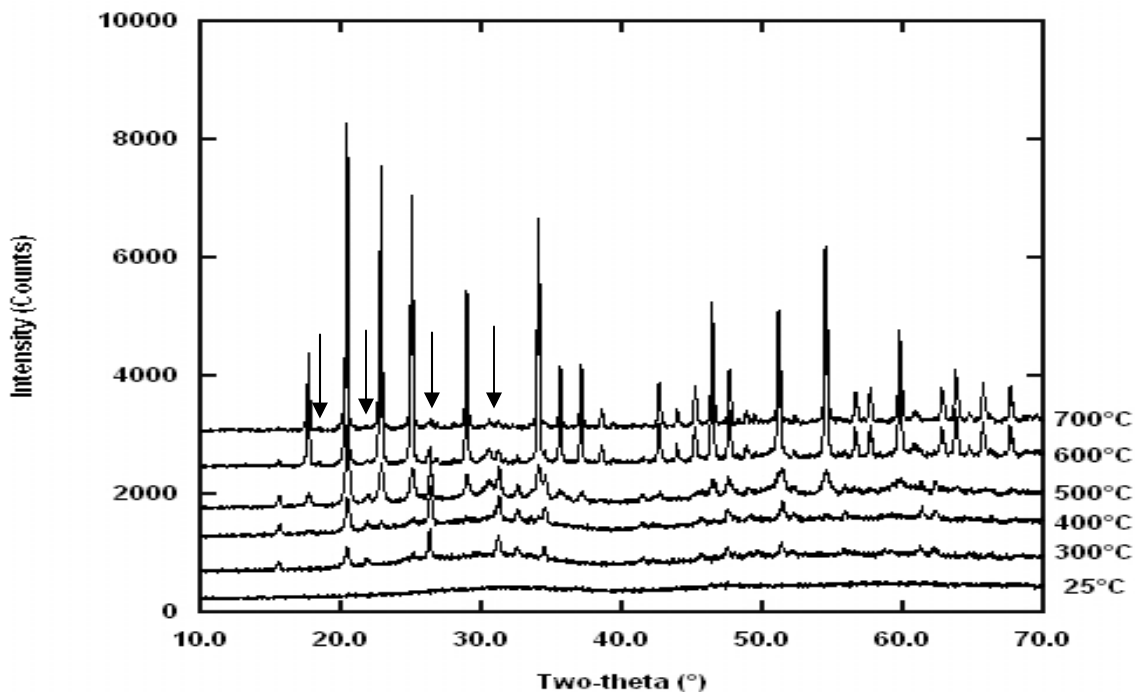


Figure 3.4: Powder XRD patterns for  $ZrV_2O_7$  (KMW23) at room temperature and after heating between  $300 - 700^\circ\text{C}$ . Some impurity peaks from  $V_2O_5$  are observed; arrows point to areas on the  $700^\circ\text{C}$  scan where impurity peaks decrease or disappear when compared to the  $600^\circ\text{C}$  scan.

another solid state synthesis yielded  $\text{ZrV}_2\text{O}_7$  after heating twice at  $750^\circ\text{C}$  for 24 hours with intermittent grinding, while aqueous preparation using the same starting materials resulted in a crystallization temperature of  $700^\circ\text{C}$  after four hours of heating.<sup>23</sup>

Degradation is observed by noting decreasing peak intensities and the appearance of  $\text{ZrO}_2$  impurity peaks along with  $\text{V}_2\text{O}_5$  after heating at  $800^\circ\text{C}$  (XRD pattern not shown). Buchanan and Wolter, in a 1983 publication, report the onset of degradation as low as 1020K, with the appearance of a liquid mixture of  $\text{V}_2\text{O}_5$  and solid  $\text{ZrO}_2$ ; the authors reported a temperature of  $840^\circ\text{C}$  for the total degradation of  $\text{ZrV}_2\text{O}_7$ .<sup>28</sup>

TG/DTA of the raw product was performed at a heating rate of  $10^\circ\text{C}/\text{minute}$  in nitrogen gas. The analysis reveals two major mass losses (see Figure 3.5): one at around

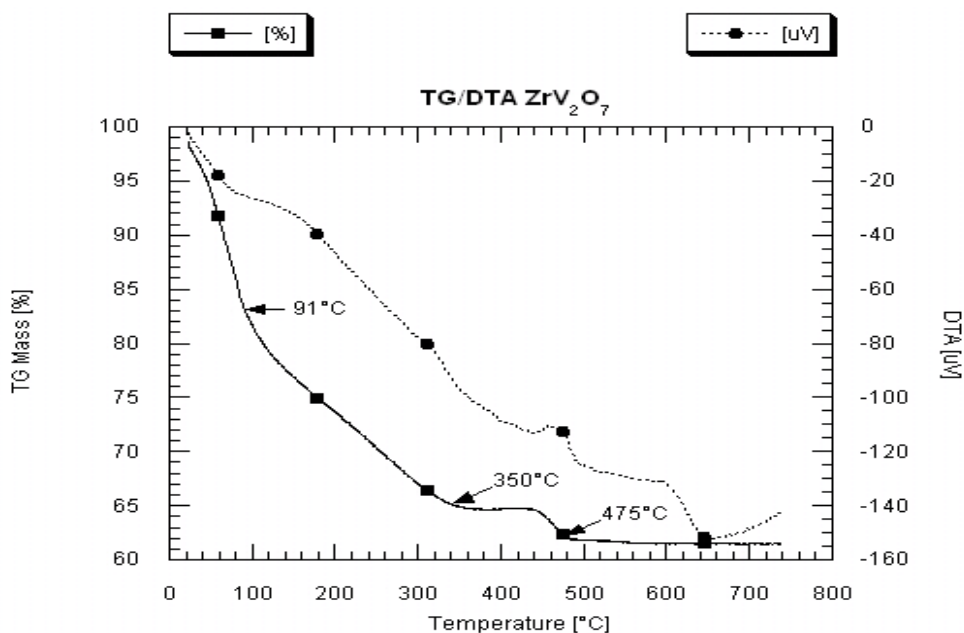


Figure 3.5: TG/DTA of raw product,  $\text{ZrV}_2\text{O}_7$ . Arrows indicate temperatures at which mass losses occur.

350°C corresponding to 35.1%, attributed to the evolution of residual organics, and one at approximately 475°C, where an additional 2.5% is lost. The later is associated with the appearance of more diffraction peaks and the reduction of the amorphous component in the powder pattern as shown in Figure 3.4 at 500°C.

### 3.4 Synthesis of $ZrP_2O_7$ Directly From Zirconium and Phosphorus Starting Materials Using Mild Autoclave Conditions (*KMW95 and KMW122*)

A few  $A^{IV}M^V_2O_7$  compounds have previously been synthesized by others with the help of mild autoclave methods. As mentioned in Section 1.2.2,  $ZrP_2O_7$  can be produced starting with an amorphous precursor gel, a-ZrP (a-zirconium phosphate). Starting materials for the a-ZrP gel included  $ZrCl_4$  dissolved in 2.0 M HCl and introduced into 1.25 M phosphoric acid. After standing overnight, the gel is filtered, washed, and air dried before mixing with concentrated  $H_3PO_4$  in a Paar bomb and heating at approximately 190°C for 4 - 6 days. This yielded the crystalline precursor,  $Zr(HPO_4)_2 \cdot H_2O$  ( $\alpha$ -ZrP).<sup>29</sup> Firing the precursor at 900°C produced the crystalline pyrophosphate. Mild autoclave methods have also been used to produce single crystals of  $ZrP_2O_7$  directly from amorphous a-ZrP gel and phosphoric acid with a ripening of the a-ZrP in concentrated  $H_3PO_4$  for 48 hours before transferring it to a Parr bomb.<sup>30</sup> Another example using mild autoclave techniques is  $\gamma$ - $GeP_2O_7$ , which was prepared by firing  $\alpha$ - $Ge(HPO_4)_2 \cdot H_2O$  that had been prepared by a mild autoclave method.<sup>31</sup>

In exploring mild autoclave synthesis methods and various starting chemicals, some interesting results were obtained that have not yet been reported in the literature for  $ZrP_2O_7$ .

### 3.4.1 Experimental

(*KMW95*) A Parr bomb was used, where 2.1878 g (6.398 mmol)  $\text{ZrO}(\text{NO}_3)_2 \cdot 6\text{H}_2\text{O}$  was placed into the Teflon<sup>®</sup> liner and 10.0 mL 10.0 M  $\text{H}_3\text{PO}_4$  was added with stirring (mole ratio P:Zr is 15.6:1). The Parr bomb was assembled and placed into a preheated 200°C oven for 96 hours. The product was filtered and washed with distilled water using four-50 mL portions until the pH of the filtrate was approximately pH 5. The white powder-like material was dried for a short time under water aspiration and then left to dry in air for 24 hours. Powder XRD of the autoclaved product confirmed it to be the cubic superlattice form of  $\text{ZrP}_2\text{O}_7$ . Mass of the autoclaved product  $\text{ZrP}_2\text{O}_7$ : 1.4966 g. *KMW122* was synthesized in the same manner.

### 3.4.2 Results and Discussion

Figure 3.6 shows the powder pattern of the product matched to the low temperature form of  $\text{ZrP}_2\text{O}_7$ , a cubic supercell. Both samples, *KMW95* and *KMW 122* were subjected to heat treatments to determine the stability of the samples. It was found using *ex situ* powder diffraction that the samples did not change after being heated up to 900°C.

As mentioned previously, mild autoclave methods have used to produce precursor material  $\text{Zr}(\text{HPO}_4)_2 \cdot \text{H}_2\text{O}$  and, recently, the preparation of single crystals of  $\text{ZrP}_2\text{O}_7$  from a-ZrP gel and phosphoric acid (Section 3.4).<sup>30</sup> The work presented here, however, is the first time that individual zirconium and phosphorus starting materials have been reported in the direct synthesis of  $\text{ZrP}_2\text{O}_7$  using mild autoclave methods.

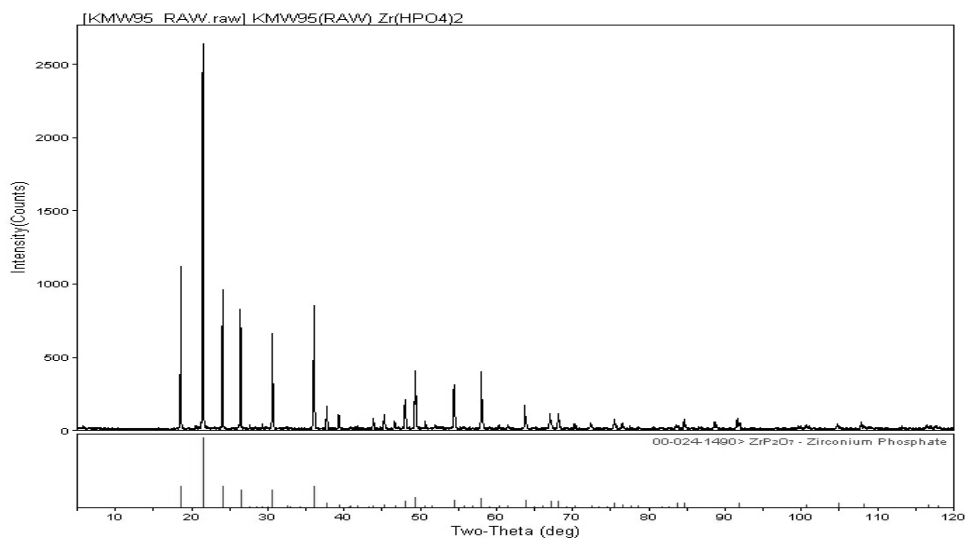


Figure 3.6: Powder pattern for *KMW95* matched to the cubic supercell structure for  $\text{ZrP}_2\text{O}_7$ .

### 3.5 Low Temperature Synthesis, Structural Studies, High Pressure Behavior, and Thermophysical Properties of $\text{CeP}_2\text{O}_7$

The first report of  $\text{CeP}_2\text{O}_7$  was in a 1960 article by Völlenkle, et al. It was synthesized from sodium pyrophosphate and cerium sulfate aqueous solutions. The amorphous yellow precipitate was dried at  $110^\circ\text{C}$ , and heated at  $900^\circ\text{C}$  resulting in crystalline  $\text{CeP}_2\text{O}_7$ , with some impurities present.<sup>32</sup> The compound was described as being isostructural with cubic  $\text{ZrP}_2\text{O}_7$  with a lattice constant of  $8.58 \text{ \AA}$ . A later paper by Botto and Baran report a similar synthesis of the compound, but cite a crystallization temperature of  $650^\circ\text{C}$  after 15 minutes of heating and a cubic superstructure for the compound with a lattice constant of  $a = 25.833 \pm 0.012 \text{ \AA}$ . Botto and Baran also report degradation of  $\text{CeP}_2\text{O}_7$  to  $\text{CeP}_3\text{O}_9$  and  $\text{CePO}_4$  with heat treatments above  $700^\circ\text{C}$ .<sup>33</sup>

Amorphous, microcrystalline, and fibrous cerium phosphates have been studied for many years due to their potential as ion-exchange materials. The first report of

microcrystalline cerium phosphate for this purpose was in a 1967 paper by König and Meyn, that described the combination of cerium (IV) salts and phosphoric acid resulting in  $\text{Ce}_2\text{O}(\text{HPO}_4)_3 \cdot \text{H}_2\text{O}$ .<sup>34</sup> Alberti et al. published the first report of  $\text{Ce}(\text{HPO}_4)_2 \cdot 1.33\text{H}_2\text{O}$ , a precursor to  $\text{CeP}_2\text{O}_7$ . In this 1972 work, Alberti et al. used cerium sulfate hydrate and 10.0 M phosphoric acid in an acid reflux method that yields the precursor compound. Subsequent heating of the precursor at 600°C resulted in crystalline  $\text{CeP}_2\text{O}_7$ . Alberti, et al. cite two phases, cerium dihydrogen phosphate,  $\text{Ce}(\text{HPO}_4)_2$ , and cerium pyrophosphate from results of TG analysis on the precursor material.<sup>35</sup> No further thermal studies were performed on the precursor material to identify the phases in that work, and nothing has been published on the thermal expansion of  $\text{CeP}_2\text{O}_7$ .

### ***3.5.1 Experimental***

Cerium pyrophosphate was synthesized using the method of Alberti, et al. Dozens of samples have been prepared as  $\text{CeP}_2\text{O}_7$  was found to degrade over a period of several months. The synthesis of a representative sample is presented: *KMW131*. A water cooled reflux apparatus was used with a 500 mL three-necked round bottom flask, fitted with stir bar, and set into a heating mantle. The necks of the flask were sealed with a cooling water condenser, a ground glass stopper, and one rubber septa through which a thermometer was inserted. Cerium sulfate hydrate was dissolved in freshly prepared, boiling 10M  $\text{H}_3\text{PO}_4$  (P:Ce molar ratio of 15:1) with stirring (boiling point observed at around 119°C). A precipitate forms in a few minutes from a clear, yellow solution and the heat was reduced. A reflux temperature of approximately 80°C was maintained over a period of 100 hours; the material was stirred occasionally throughout the reflux.

The product was a shiny yellow, wet solid. After filtering using a water aspirator, approximately 20 mL of anhydrous acetone was used to wash the product. Hot distilled water was used next in order to remove any by-products observable in the filtration flask as a white, waxy substance. Washing continued with 50-100 mL portions of ice cold distilled water. The filtrate was tested with pH paper, and ice cold distilled water washing was stopped after a pH of approximately 4 was noted. The product was permitted to dry under water aspiration for two hours during which time the solid paste-like material was stirred and chopped with a spatula. The air-dried precursor to  $\text{CeP}_2\text{O}_7$ ,  $\text{Ce}(\text{HPO}_4)_2 \cdot x\text{H}_2\text{O}$ , was stored over a saturated (75%) solution of NaCl in a desiccator for approximately seven days.

Treatments of the precursor involved heating in a ceramic crucible at 200°C for 20 hours, 400°C for 4 hours, and 600°C for 16 hours to obtain the off-white crystalline powder,  $\text{CeP}_2\text{O}_7$ . All precursor materials and final crystalline products prepared in this fashion were initially characterized by lab powder XRD using a Scintag diffractometer instrument. In addition to lab powder XRD, other characterization methods included high resolution synchrotron powder XRD, high temperature synchrotron and lab powder XRD, high pressure synchrotron powder XRD, and TG/DTA.

### ***3.5.2 Results and Discussion***

#### ***3.5.2.1 Structural Studies***

Lab powder XRD scans of room temperature  $\text{CeP}_2\text{O}_7$  raised questions as to its reported symmetry and structure.<sup>32, 33</sup> Scans taken over 12-14 hours were initially

modeled using the Rietveld method with the high temperature  $\text{ZrP}_2\text{O}_7$  structure, space group  $P\bar{3}$ . However, a closer inspection of some peaks, Figure 3.7 (a), indicated something other than a cubic structure. In (a), the lab powder XRD pattern shows some indication of peak splitting for peaks at approximately 2.37 Å and 2.47 Å. This is not consistent with cubic symmetry. Peaks at lower angles did not show obvious splittings.

High resolution synchrotron powder XRD (Section 2.1.3) was performed on one sample (*KMW131*) of  $\text{CeP}_2\text{O}_7$  at room temperature using beam line 32ID at the Advanced Photon Source (APS) and the results confirmed the initial observations from lab powder data. Figure 3.7 (b) is a zoom image of the synchrotron scan for the same two peaks at the same d-spacing as shown in (a). The high resolution scan (b) shows distinct and well-defined peak splitting. The high resolution synchrotron powder scan ( $\lambda = 0.49615$  Å), in

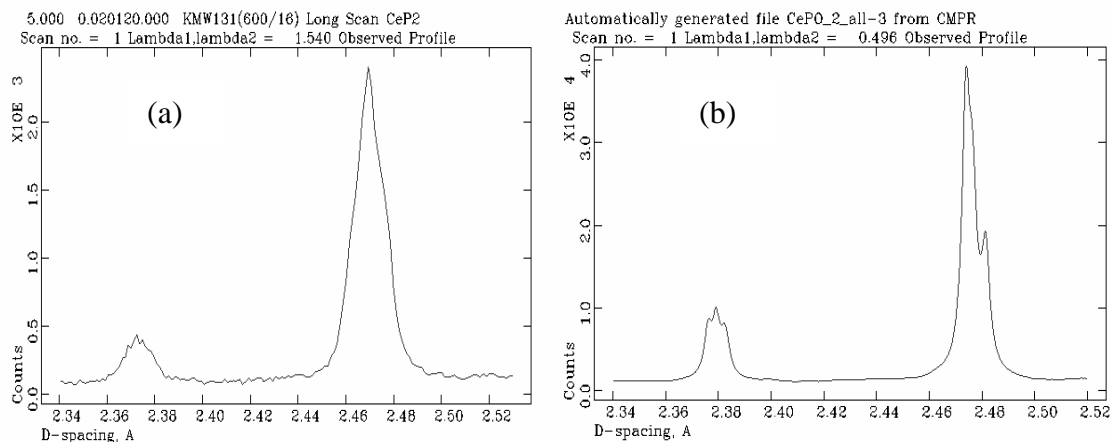


Figure 3.7: Zoom images of GSAS RAWPLOT scans showing d-spacing of 2.34-2.52 Å for room temperature  $\text{CeP}_2\text{O}_7$ ; (a) lab powder XRD and (b) high resolution synchrotron powder XRD.

fact, revealed the presence of peak splitting for all peaks in the pattern over 2 - 40 two-

theta ( $^{\circ}$ ) range (not shown); however low angle, low intensity peaks associated with some superlattice structures in the  $A^{IV}M^V_2O_7$  family were not observed. The number of components in the split peaks suggested a low symmetry and the absence of low angle low intensity peaks suggested the compound did not have a superlattice.

The literature on members of the  $A^{IV}M^V_2O_7$  family of compounds indicates that some compounds have superlattices at room temperature and some have symmetries lower than cubic. Evidence for cubic superlattices have been reported for  $UP_2O_7$ ,<sup>36, 37</sup>  $TiP_2O_7$ ,<sup>38-40</sup>  $ReP_2O_7$ ,<sup>41</sup>,  $HfV_2O_7$ ,<sup>27, 42</sup>  $PbP_2O_7$ ,<sup>32</sup> and  $ZrV_2O_7$ .<sup>26, 43, 44</sup> MAS  $^{31}P$ -NMR for room temperature  $ZrP_2O_7$  reveals a superlattice and the presence of many crystallographically distinct P groups, eleven from the work of Korthius, et al. (cubic) and thirteen from the work of King, et al (orthorhombic).<sup>30, 36, 45, 46</sup> More than 35 unique P-groups were found for room temperature monoclinic  $\gamma$ - $GeP_2O_7$ .<sup>31</sup>  $SnP_2O_7$  has also been reported to have a room temperature supercell structure (orthorhombic or monoclinic)<sup>47, 48</sup>.  $SiP_2O_7$  exists in five polymorphs: a cubic superlattice,<sup>49</sup> two monoclinic, hexagonal, and tetragonal forms, the later four do not have supercells;<sup>50</sup> in addition,  $ThP_2O_7$  exists in two non-supercell forms: orthorhombic and cubic.<sup>51, 52</sup>

MAS  $^{31}P$ -NMR (Section 2.4) spectra for room temperature  $CeP_2O_7$  (Figure 3.8) showed a single, broad peak centered at a chemical shift of approximately -44 ppm with what appeared to be some splitting indicating the presence of more than one phosphate environment. However, the spectrum was much simpler than that of  $ZrP_2O_7$  (Figure 3.3). Compounds with cubic symmetry in  $P$  a  $\bar{3}$  space group were expected to have a single, narrow peak representing one distinct P group. Superlattices were expected to show several crystallographically unique P groups, depending upon symmetry.<sup>23, 48</sup>

Finding a unit cell and space group that can adequately describe the structure of  $\text{CeP}_2\text{O}_7$  involved peak fitting of high resolution synchrotron powder XRD data using JADE (Section 2.5.1). The peak positions were then used as input for the CRYSFIRE (Section 2.5.3) indexing software. This resulted in hundreds of potential unit cells. One such cell was a triclinic unit cell,  $a = 6.061 \text{ \AA}$ ,  $b = 8.55 \text{ \AA}$ ,  $c = 6.070 \text{ \AA}$ ;  $\alpha = 90.16^\circ$ ,  $\beta = 90.15^\circ$ ,  $\gamma = 90.00^\circ$  and a figure of merit (FOM) of 44.41, the highest FOM obtained during indexing.

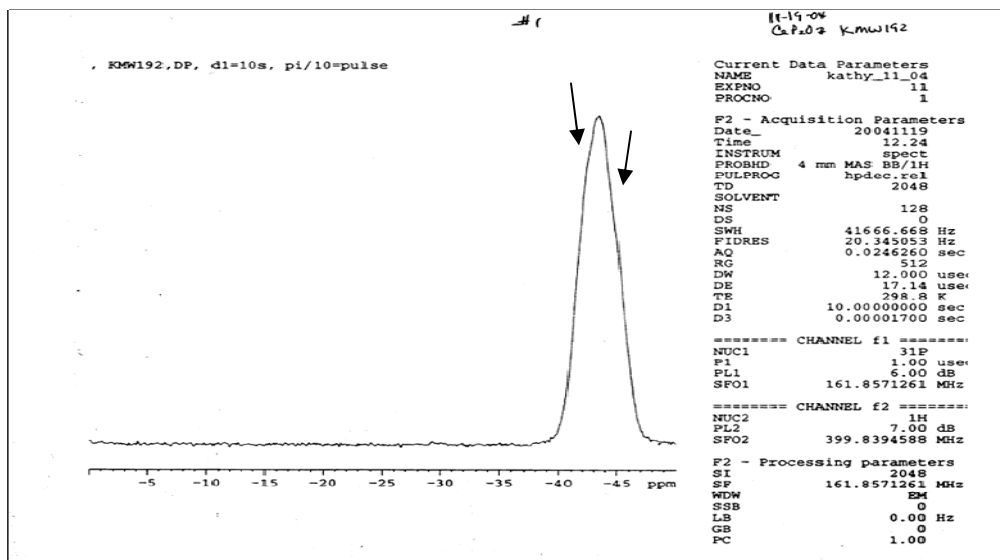


Figure 3.8: Room temperature MAS  $^{31}\text{P}$ -NMR for  $\text{CeP}_2\text{O}_7$ . Arrows point to two areas of overlap indicating possibly more than one closely related P group.

The high resolution synchrotron data were fit using the Le Bail method and this triclinic unit cell. While the main peaks were reproduced, the model did not account for the many split peaks across the range of the scan. However, using the triclinic subcell found initially with the LePage transformation algorithm from CHECKCELL (Section

2.5.3), a likely quasi-cubic triclinic subcell was found. The unit cell was refined using the LeBail method in GSAS (Section 2.5.2). Refined lattice constants were  $a = 8.5673(4) \text{ \AA}$ ,  $b = 8.5823(3) \text{ \AA}$ ,  $c = 8.5865(4) \text{ \AA}$ ;  $\alpha = 89.93(0)^\circ$ ,  $\beta = 90.18(0)^\circ$ ,  $\gamma = 90.09(0)^\circ$ . All the major peaks including splittings could be reproduced in this refinement (wRp = 8.31%; reduced  $\chi^2 = 145.1$ ). Figure 3.9 shows the refined experimental data from high resolution synchrotron powder XRD. Several low intensity peaks, inset in Figure 3.9, were not explained by this model indicating the presence of an impurity phase(s) or a possible superlattice for room temperature  $\text{CeP}_2\text{O}_7$ . Impurities could consist of a mixture of degradation products as a result of firing, but analyses for impurities of cerium

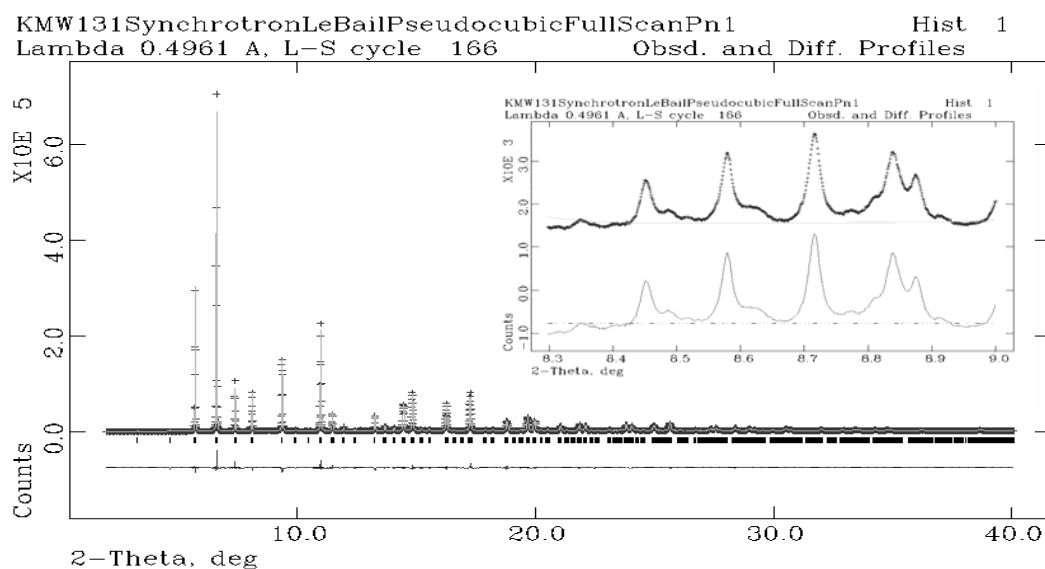


Figure 3.9: GSAS LeBail fit to high resolution synchrotron data for  $\text{CeP}_2\text{O}_7$  using quasi-cubic unit cell. Lower curve under vertically oriented symmetry tick marks is the difference curve; inset shows experimental data (top curve) and difference curve (lower curve) of representative low intensity peaks not accounted for by this model.

phosphates, including known degradation products  $\text{CePO}_4$  and  $\text{CeP}_3\text{O}_9$ , did not result in an identification of a phase or phases for the low intensity peaks in the scan. However, as previously pointed out, the absence of weak, low angle peaks characteristic of superlattice structures suggests a simple unit cell. Based on this and MAS  $^{31}\text{P}$ -NMR data, the presence of a superlattice seemed unlikely.

Using the quasi-cubic unit cell, a structure refinement was attempted. Starting atom positions in space group  $P\bar{1}$  were determined by applying all of the symmetry operations in space group  $P\bar{3}$  to the atomic coordinates for the high temperature cubic  $\text{ZrP}_2\text{O}_7$  structure. Table 3.1 shows the symmetry operations, cubic  $\text{ZrP}_2\text{O}_7$  atom positions, and calculated starting atom positions for triclinic  $\text{CeP}_2\text{O}_7$ .

Refinement was attempted using TOPAS (Section 2.52). Initially, the coordinates were left fixed at the positions determined by transformation from  $P\bar{3}$  and the lattice constants optimized by a simulated annealing type procedure. The lattice constants were randomly perturbed by a small amount and then refined to convergence. The process of perturbation and refinement was repeated many times and the best fit from this procedure was taken to be the optimized unit cell. This resulted in the following lattice constants:  $a = 8.56805(4) \text{ \AA}$ ,  $b = 8.58472(8) \text{ \AA}$ ,  $c = 8.58210(7) \text{ \AA}$ ;  $\alpha = 89.92817(56)^\circ$ ,  $\beta = 89.90956(62)^\circ$ ,  $\gamma = 89.82725(54)^\circ$ . Next, the lattice constants were fixed and the coordinates optimized, by a simulated annealing type process. Small random perturbations were applied to all the coordinates, within the range of  $\pm 0.03$ , and they were then refined to convergence. This process was repeated many times and the best fit retained. During the structure refinement, constraints were placed on the thermal factors for all like atoms, Ce, P, and O, and soft restraints were placed on P – O bond lengths,

while no restraints were placed on bond angles. The final refinement statistics were  $wRp = 10.475\%$  (weighted R factor) and r-Bragg value = 3.05%.

Table 3.1 P a -3 Symmetry Operations,  $ZrP_2O_7$  Fractional Atom Coordinates, and Transformed Atom Coordinates for  $CeP_2O_7$

Symmetry Operations			Atom	x	y	z	
x,y,z	-x+1/2,-y,z+1/2	-x,y+1/2,-z+1/2	Ce1	0.0000	0.0000	0.0000	
x+1/2,-y+1/2,-z	z,x,y	y,z,x	Ce2	0.5000	0.5000	0.0000	
z+1/2,-x+1/2,-y	-y,z+1/2,-x+1/2	-z+1/2,-x,y+1/2	Ce3	0.0000	0.5000	0.5000	
y+1/2,-z+1/2,-x	-z,x+1/2,-y+1/2	-y+1/2,-z,x+1/2	Ce4	0.5000	0.0000	0.5000	
-x,-y,-z	x+1/2,y,-z+1/2	x,-y+1/2,z+1/2	P1	0.3933	0.3933	0.3933	
-x+1/2,y+1/2,z	-z,-x,-y	-y,-z,-x	P2	0.8933	0.1067	-0.3933	
-z+1/2,x+1/2,y	y,-z+1/2,x+1/2	z+1/2,x,-y+1/2	P3	-0.3933	-0.3933	-0.3933	
-y+1/2,z+1/2,x	z,-x+1/2,y+1/2	y+1/2,z,-x+1/2	P4	0.1067	0.8933	0.3933	
			P5	0.1067	-0.3933	0.8933	
			P6	-0.3933	0.8933	0.1067	
			P7	0.8933	0.3933	0.1067	
			P8	0.3933	0.1067	0.8933	
<b>ZrP<sub>2</sub>O<sub>7</sub> fractional atom coordinates</b>							
Atom	x	y	z				
Zr1	0.0000	0.0000	0.0000	O1	0.0000	-0.5000	1.0000
P1	0.3933	0.3933	0.3933	O2	-0.5000	1.0000	0.0000
O3	0.4430	0.2230	0.4380	O3	1.0000	0.0000	-0.5000
O4	0.5000	0.5000	0.5000	O4	-0.5000	-0.5000	-0.5000
				O5	0.4430	0.2230	0.4380
				O6	0.0570	-0.2230	0.9380
				O7	-0.4430	0.7230	0.0620
				O8	0.9430	0.2770	-0.4380
				O9	0.4380	0.4430	0.2230
				O10	0.9380	0.0570	-0.2230
				O11	0.0620	-0.4430	0.7230
				O12	-0.4380	0.9430	0.2770
				O13	0.2230	0.4380	0.4430
				O14	-0.2230	0.9380	0.4430
				O15	0.7230	0.0620	-0.4430
				O16	0.2270	-0.4380	0.9430
				O17	-0.4430	-0.2230	-0.4380
				O18	0.9430	0.2230	0.0620
				O19	0.4430	0.2770	0.9380
				O20	0.0570	0.7230	0.4380
				O21	-0.4380	-0.4430	-0.2230
				O22	0.0620	0.9430	0.2230
				O23	0.9380	0.4430	0.2770
				O24	0.4380	0.0570	0.7230
				O25	-0.2230	-0.4380	-0.4430
				O26	0.2230	0.0620	0.9430
				O27	0.2770	0.9380	0.4430
				O28	0.7230	0.4380	0.0570

Table 3.2 Refined Fractional Coordinates and Equivalent Isotropic Displacement Parameters for CeP<sub>2</sub>O<sub>7</sub>

<b>Atom</b>	<b>x</b>	<b>y</b>	<b>z</b>	<b>Beq</b>
Ce1	-0.001(1)	0.000(2)	0.001(2)	1.7(3)
Ce2	0.500(1)	-0.001(2)	0.500(2)	
Ce3	0.000(1)	0.500(2)	0.500(2)	
Ce4	0.498(1)	0.500(2)	0.000(2)	
P1	0.418(1)	0.392(2)	0.399(2)	1.6(3)
P2	0.053(2)	-0.412(2)	0.874(1)	
P3	-0.384(1)	0.904(2)	0.098(2)	
P4	0.893(2)	0.106(2)	-0.379(2)	
P5	-0.370(1)	-0.394(2)	-0.390(2)	
P6	0.887(2)	0.400(2)	0.088(2)	
P7	0.406(2)	0.113(2)	0.892(1)	
P8	0.079(2)	0.924(1)	0.425(2)	
O1	0.432(4)	0.228(2)	0.437(4)	3.0(3)
O2	0.088(4)	-0.241(2)	0.930(3)	
O3	-0.478(3)	0.747(3)	0.079(3)	
O4	0.984(4)	0.241(5)	-0.466(3)	
O5	0.390(3)	0.436(4)	0.231(2)	
O6	0.966(3)	0.026(3)	-0.247(3)	
O7	0.137(3)	-0.423(4)	0.715(3)	
O8	-0.436(3)	0.928(4)	0.259(2)	
O9	0.240(2)	0.434(3)	0.432(4)	
O10	-0.235(2)	0.956(4)	0.037(5)	
O11	0.761(3)	0.034(4)	-0.475(4)	
O12	0.252(2)	-0.407(3)	0.928(4)	
O13	-0.448(3)	-0.246(3)	-0.447(4)	
O14	0.946(4)	0.236(2)	0.098(4)	
O15	0.444(3)	0.289(2)	0.930(4)	
O16	0.117(3)	0.745(2)	0.379(3)	
O17	-0.479(3)	-0.446(4)	-0.251(4)	
O18	0.112(3)	0.945(4)	0.235(3)	
O19	0.931(3)	0.463(4)	0.257(2)	
O20	0.443(4)	0.068(5)	0.733(2)	
O21	-0.250(4)	-0.446(3)	-0.498(3)	
O22	0.242(2)	0.063(3)	0.957(3)	
O23	0.274(2)	0.914(3)	0.425(4)	
O24	0.764(4)	0.488(3)	0.005(6)	
O25	0.561(3)	0.505(3)	0.483(2)	
O26	0.037(3)	0.527(3)	0.031(2)	
O27	0.550(3)	0.045(3)	-0.023(3)	
O28	0.010(2)	0.061(2)	0.495(3)	

Table 3.2 lists refined fractional atom coordinates for CeP<sub>2</sub>O<sub>7</sub> along with the equivalent thermal parameters, Beq (= 8π<sup>2</sup> Uiso). The thermal parameters are reasonable for Ce, P, and O. Table 3.3 lists refined bond lengths and bond angles for CeO<sub>6</sub> octahedra, with Ce – O bond lengths ranging from 1.969(26) Å to 2.339(24) Å. For Ce<sup>4+</sup> with coordination number 6, Ce-O bond distances have been reported to range between 2.026 Å and 2.588 Å in cerium oxides.<sup>53</sup> In monazite (CePO<sub>4</sub>), Ce – O bond lengths are reported between 2.455(2) Å and 2.776(3) Å, but in monazite, cerium is in a 3+ oxidation state.<sup>54</sup> However, in UP<sub>2</sub>O<sub>7</sub>, where the ionic radius of U<sup>4+</sup> (0.890 Å) is similar to that of Ce<sup>4+</sup> (0.870 Å), U – O bond lengths are reported to be 2.243(7) Å.<sup>37</sup> The shorter Ce – O

Table 3.3 Refined Ce:O Bond Distances (Å) and Bond Angles (°) from TOPAS Refinement for CeP<sub>2</sub>O<sub>7</sub>

bond distance		bond angle		bond angle		bond angle	
Ce(1):O(10)	2.061(24)						
Ce(1):O(6)	2.155(32)	O(10)-Ce(1)-O(6)	92.3(14)	O(6)-Ce(1)-O(22)	176.0(11)	O(22)-Ce(1)-O(18)	161.08(93)
Ce(1):O(22)	2.181(24)	O(10)-Ce(1)-O(22)	85.98(84)	O(6)-Ce(1)-O(14)	104.43(87)	O(22)-Ce(1)-O(2)	82.0(11)
Ce(1):O(14)	2.241(27)	O(10)-Ce(1)-O(14)	91.7(12)	O(6)-Ce(1)-O(18)	78.3(10)	O(14)-Ce(1)-O(18)	104.0(12)
Ce(1):O(18)	2.281(26)	O(10)-Ce(1)-O(18)	86.71(95)	O(6)-Ce(1)-O(2)	170.1(13)	O(14)-Ce(1)-O(2)	82.84(81)
Ce(1):O(2)	2.286(26)	O(10)-Ce(1)-O(2)	84.6(11)	O(22)-Ce(1)-O(14)	85.2(11)	O(18)-Ce(1)-O(2)	101.3(12)
Ce(2):O(1)	2.122(23)						
Ce(2):O(20)	2.143(26)	O(1)-Ce(2)-O(20)	85.2(10)	O(20)-Ce(2)-O(23)	89.54(97)	O(23)-Ce(2)-O(8)	178.9(17)
Ce(2):O(23)	2.172(22)	O(1)-Ce(2)-O(23)	99.8(11)	O(20)-Ce(2)-O(13)	96.9(14)	O(23)-Ce(2)-O(11)	162.5(13)
Ce(2):O(13)	2.194(27)	O(1)-Ce(2)-O(13)	85.4(11)	O(20)-Ce(2)-O(8)	81.3(13)	O(13)-Ce(2)-O(8)	94.7(13)
Ce(2):O(8)	2.222(24)	O(1)-Ce(2)-O(8)	83.2(13)	O(20)-Ce(2)-O(11)	84.8(12)	O(13)-Ce(2)-O(11)	95.7(14)
Ce(2):O(11)	2.272(29)	O(1)-Ce(2)-O(11)	83.14(82)	O(23)-Ce(2)-O(13)	174.8(10)	O(8)-Ce(2)-O(11)	99.8(13)
Ce(3):O(19)	2.191(24)						
Ce(3):O(21)	2.195(36)	O(19)-Ce(2)-O(21)	76.87(79)	O(21)-Ce(2)-O(9)	87.7(12)	O(9)-Ce(2)-O(7)	116.0(11)
Ce(3):O(9)	2.208(24)	O(19)-Ce(2)-O(9)	164.6(13)	O(21)-Ce(2)-O(4)	98.3(12)	O(9)-Ce(2)-O(16)	74.79(80)
Ce(3):O(4)	2.247(47)	O(19)-Ce(2)-O(4)	80.9(11)	O(21)-Ce(2)-O(7)	79.0(11)	O(4)-Ce(2)-O(7)	161.6(11)
Ce(3):O(7)	2.287(27)	O(19)-Ce(2)-O(7)	102.47(87)	O(21)-Ce(2)-O(16)	153.42(95)	O(4)-Ce(2)-O(16)	102.3(10)
Ce(3):O(16)	2.553(24)	O(19)-Ce(2)-O(16)	83.43(81)	O(9)-Ce(2)-O(4)	87.7(12)	O(7)-Ce(2)-O(16)	80.9(11)
Ce(4):O(15)	1.969(26)						
Ce(4):O(17)	2.218(34)	O(15)-Ce(4)-O(15)	85.1(11)	O(17)-Ce(4)-O(3)	171.4(13)	O(3)-Ce(4)-O(24)	86.61(75)
Ce(4):O(3)	2.235(28)	O(15)-Ce(4)-O(17)	95.1(12)	O(17)-Ce(4)-O(5)	160.5(11)	O(3)-Ce(4)-O(12)	80.80(79)
Ce(4):O(5)	2.255(24)	O(15)-Ce(4)-O(5)	89.95(82)	O(17)-Ce(4)-O(24)	86.80(79)	O(5)-Ce(4)-O(24)	101.8(10)
Ce(4):O(24)	2.279(33)	O(15)-Ce(4)-O(24)	112.55(83)	O(17)-Ce(4)-O(12)	86.77(79)	O(5)-Ce(4)-O(12)	75.5(11)
Ce(4):O(12)	2.339(24)	O(15)-Ce(4)-O(12)	157.1(13)	O(3)-Ce(4)-O(5)	87.1(15)	O(24)-Ce(4)-O(12)	90.9(12)

bond lengths, therefore, were not expected. CeO<sub>6</sub> octahedra bond angles exhibit distortion (Table 3.3), where angles should be close to 90° for equatorial bonds and close to 180° for axial bonds in an ideal octahedron. Equatorial O – Ce – O bond angles (Table 3.3)

Table 3.4 Refined P-O Bond Distances (Å) and Bond Angles (°) for CeP<sub>2</sub>O<sub>7</sub> from TOPAS

	distance		bond angle		bond angle		bond angle		bond angle
P(1):O(1)	1.449(23)								
P(1):O(5)	1.511(25)	O(1)-P(1)-O(5)	117.9(21)	O(5)-P(1)-O(9)	104.8(18)	P(1)-O(9)-P(5)	119.5(13)		
P(1):O(9)	1.595(26)	O(1)-P(1)-O(9)	87.3(12)	O(5)-P(1)-O(25)	111.8(15)	P(1)-O(25)-P(5)	113.3(13)		
P(1):O(25)	1.721(29)	O(1)-P(1)-O(25)	118.9(13)	P(1)-O(5)-P(5)	108.8(11)				
P(1):P(5)	3.152(13)	P(1)-O(1)-P(5)	11.91(73)	O(9)-P(1)-O(25)	113.7(16)				
P(2):O(26)	1.457(21)								
P(2):O(7)	1.545(26)	O(26)-P(2)-O(7)	147.1(17)	O(7)-P(2)-O(2)	94.0(15)	P(2)-O(2)-P(6)	140.4(12)		
P(2):O(2)	1.575(26)	O(26)-P(2)-O(2)	104.0(14)	O(7)-P(2)-O(12)	77.6(11)	O(2)-P(2)-O(24)	109.1(13)		
P(2):O(12)	1.770(26)	O(26)-P(2)-O(12)	73.1(13)	P(2)-O(7)-P(6)	115.4(10)	P(2)-O(12)-P(6)	31.07(94)		
P(2):P(6)	2.830(15)	P(2)-O(26)-P(6)	109.1(11)	O(7)-P(2)-O(24)	137.6(12)	O(12)-P(2)-O(24)	137.2(12)		
P(2):O(24)	2.855(38)	O(26)-P(2)-O(24)	30.08(30)	O(2)-P(2)-O(12)	81.7(15)	P(2)-O(24)-P(6)	56.0(13)		
P(3):O(10)	1.454(28)								
P(3):O(8)	1.472(24)	O(10)-P(3)-O(8)	124.0(21)	O(8)-P(3)-O(3)	132.7(20)	P(3)-O(3)-P(7)	106.3(12)		
P(3):O(3)	1.582(28)	O(10)-P(3)-O(3)	93.6(17)	O(8)-P(3)-O(27)	112.0(15)	P(3)-O(27)-P(7)	97.3(14)		
P(3):O(27)	1.687(31)	O(10)-P(3)-O(27)	112.4(12)	P(3)-O(8)-P(7)	98.18(98)				
P(3):P(7)	3.092(13)	P(3)-O(10)-P(7)	16.48(86)	O(3)-P(3)-O(27)	81.5(15)				
P(4):O(6)	1.463(31)								
P(4):O(28)	1.528(25)	O(6)-P(4)-O(28)	98.7(13)	O(28)-P(4)-O(11)	123.2(14)	P(4)-O(11)-P(8)	19.38(81)		
P(4):O(11)	1.532(33)	O(6)-P(4)-O(11)	89.8(17)	O(28)-P(4)-O(4)	61.6(16)	P(4)-O(4)-P(8)	87.8(12)		
P(4):O(4)	1.586(42)	O(6)-P(4)-O(4)	113.8(19)	P(4)-O(28)-P(8)	82.4(14)				
P(4):P(8)	2.794(18)	P(4)-O(6)-P(8)	80.9(14)	O(11)-P(4)-O(4)	119.6(17)				
P(5):O(21)	1.448(34)								
P(5):O(25)	1.510(26)	O(21)-P(5)-O(25)	69.0(14)	O(25)-P(5)-O(13)	111.3(18)	P(5)-O(13)-P(1)	13.6(10)		
P(5):O(13)	1.514(28)	O(21)-P(5)-O(13)	94.6(16)	O(25)-P(5)-O(17)	98.9(16)	P(5)-O(17)-P(1)	82.2(14)		
P(5):O(17)	1.574(32)	O(21)-P(5)-O(17)	102.7(14)	P(5)-O(25)-P(1)	93.1(12)				
P(5):P(1)	3.152(20)	P(5)-O(21)-P(1)	86.0(13)	O(13)-P(5)-O(17)	144.5(20)				
P(6):O(24)	1.475(38)								
P(6):O(14)	1.494(27)	O(24)-P(6)-O(14)	138.3(21)	O(14)-P(6)-O(19)	115.8(22)	P(6)-O(194)-P(2)	113.9(15)		
P(6):O(19)	1.596(28)	O(24)-P(6)-O(19)	100.7(15)	O(14)-P(6)-O(26)	110.7(15)	P(6)-O(26)-P(2)	75.9(16)		
P(6):O(26)	1.752(27)	O(24)-P(6)-O(26)	82.4(12)	P(6)-O(14)-P(2)	106.2(13)				
P(6):P(2)	2.830(21)	P(6)-O(24)-P(2)	25.43(67)	O(19)-P(6)-O(26)	94.2(15)				
P(7):O(20)	1.453(25)								
P(7):O(27)	1.550(28)	O(20)-P(7)-O(27)	99.9(16)	O(27)-P(7)-O(15)	113.9(22)	P(7)-O(15)-P(3)	18.0(11)		
P(7):O(15)	1.574(26)	O(20)-P(7)-O(15)	95.6(17)	O(27)-P(7)-O(22)	116.2(15)	P(7)-O(22)-P(3)	104.9(16)		
P(7):O(22)	1.578(26)	O(20)-P(7)-O(22)	112.2(14)	P(7)-O(27)-P(3)	108.4(13)				
P(7):P(3)	3.092(18)	P(7)-O(20)-P(3)	99.1(11)	O(15)-P(7)-O(22)	116.6(17)				
P(8):O(28)	1.445(23)								
P(8):O(16)	1.615(24)	O(28)-P(8)-O(16)	162.3(15)	O(16)-P(8)-O(18)	112.9(16)	P(8)-O(18)-P(4)	141.9(11)	O(23)-P(8)-O(6)	109.0(15)
P(8):O(18)	1.661(27)	O(28)-P(8)-O(18)	80.2(10)	O(16)-P(8)-O(23)	75.72(94)	O(18)-P(8)-O(4)	104.9(13)	O(4)-P(8)-O(11)	11.2(10)
P(8):O(23)	1.669(19)	O(28)-P(8)-O(23)	80.8(10)	P(8)-O(16)-P(4)	128.9(12)	O(18)-P(8)-O(11)	157.2(15)	O(4)-P(8)-O(6)	122.9(12)
P(8):P(4)	2.794(19)	P(8)-O(28)-P(4)	126.8(14)	O(16)-P(8)-O(4)	108.7(13)	O(18)-P(8)-O(6)	28.11(31)	P(8)-O(4)-P(4)	155.8(13)
P(8):O(4)	2.988(45)	O(28)-P(8)-O(4)	31.62(34)	O(16)-P(8)-O(11)	30.37(31)	O(23)-P(8)-O(4)	20.54(90)	O(11)-P(8)-O(6)	42.1(11)
P(8):O(11)	3.003(31)	O(28)-P(8)-O(11)	51.69(67)	O(16)-P(8)-O(6)	51.25(60)	P(8)-O(23)-P(4)	173.5(12)	P(8)-O(11)-P(4)	123.2(12)
P(8):O(6)	3.103(32)	O(28)-P(8)-O(6)	51.07(88)	O(18)-P(8)-O(23)	116.9(15)	O(23)-P(8)-O(11)	113.4(13)	P(8)-O(6)-P(4)	42.9(10)

range from  $74.79(80)^\circ$  in O(9) – Ce(2) – O(16) to  $112.54(83)^\circ$  in O(15) – Ce(4) – O(24). Axial Ce – O bonds were observed ranging from  $153.42(95)^\circ$  for O(21) – Ce(2) – O(16) to  $178.9(17)^\circ$  for O(23) – Ce(2) – O(8).

In Table 3.4, shorter P – O bond lengths were associated with internal P – O bond distances in PO<sub>4</sub> tetrahedra. P – O bond lengths, ranging from 1.448(34) Å to 1.770(26) Å, were somewhat larger range than expected based on those reported for pyrophosphates: 1.471(5) Å – 1.539(4) Å<sup>55</sup> and 1.481(3) Å – 1.584(3) Å<sup>30</sup> for ZrP<sub>2</sub>O<sub>7</sub>; 1.43(1) Å – 1.59(1) Å for UP<sub>2</sub>O<sub>7</sub>;<sup>37</sup> and 1.50(1) Å to 1.60(1) Å for TiP<sub>2</sub>O<sub>7</sub>.<sup>38</sup> The lower range value of 1.448(34) Å was noted to be slightly larger than the lower range value for UP<sub>2</sub>O<sub>7</sub>, 1.43(1) Å. P – O – P distances range from 2.794(18) Å to 3.152(20) Å (see Table 3.4) with an average distance of 2.967 Å. This can be compared to the low range P – O – P distances of 3.06 Å for TiP<sub>2</sub>O<sub>7</sub><sup>38</sup> and 3.18 Å for UP<sub>2</sub>O<sub>7</sub>.<sup>37</sup> P – O – P bond angles show considerable distortion from what would be expected for a simple cubic structure, where P – O – P angles average 180°. Bond angles as small as  $13.6(10)^\circ$  and  $16.48(86)^\circ$  indicated unrealistic P – O – P angles. Table 3.5 shows Ce – O – P bond angles that range from  $125.63(63)^\circ$  to  $178.87(56)^\circ$ , which appear reasonable.

In general, the distances and angles seem to suggest that the structure resulting from the refinement is of low quality. There are shorter than expected Ce – O bond lengths, larger than expected P – O bond distances, and large distortions in O – Ce – O and P – O – P bond angles. No conclusion was made about the structure based on the model from this refinement. However, the quality of the profile fit suggests that this structure is triclinic.

Figures 3.10 (a) and (b) are graphical representations useful in visualizing the

Table 3.5 Refined Ce - O - P Bond Angles (°) for CeP<sub>2</sub>O<sub>7</sub> from TOPAS

bond angles		bond angles	
Ce(2)-O(1)-P(1)	168.2(22)	Ce(2)-O(13)-P(5)	163.60(50)
Ce(1)-O(2)-P(2)	130.03(59)	Ce(1)-O(14)-P(6)	153.80(58)
Ce(4)-O(3)-P(3)	152.93(77)	Ce(4)-O(15)-P(7)	173.64(49)
Ce(3)-O(4)-P(4)	157.06(84)	Ce(3)-O(16)-P(8)	154.01(71)
Ce(4)-O(5)-P(1)	162.24(76)	Ce(4)-O(17)-P(5)	147.97(45)
Ce(1)-O(6)-P(4)	149.99(65)	Ce(1)-O(18)-P(8)	164.58(74)
Ce(3)-O(7)-P(2)	166.39(79)	Ce(3)-O(19)-P(6)	168.61(57)
Ce(2)-O(8)-P(3)	171.88(68)	Ce(2)-O(20)-P(7)	178.87(56)
Ce(3)-O(9)-P(1)	140.20(79)	Ce(3)-O(21)-P(5)	152.62(93)
Ce(1)-O(10)-P(3)	139.81(84)	Ce(1)-O(22)-P(7)	168.92(45)
Ce(2)-O(11)-P(4)	167.72(67)	Ce(2)-O(23)-P(8)	139.42(82)
Ce(4)-O(12)-P(2)	125.63(63)	Ce(4)-O(24)-P(6)	138.12(56)

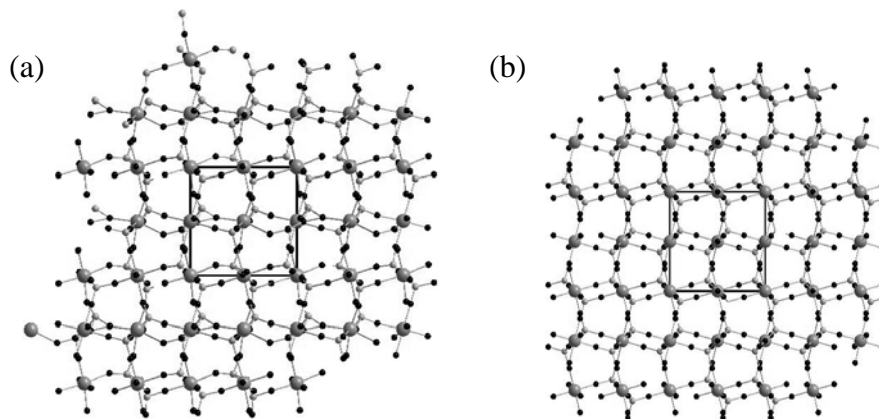


Figure 3.10: (a) Graphic represents the refined structure of CeP<sub>2</sub>O<sub>7</sub> in P 1 using refined atom positions and filling atoms around the unit cell for comparison to (b), representation of a cubic structure in P a -3 modeled with Ce, P, and O using ZrP<sub>2</sub>O<sub>7</sub> as a model. For (a) and (b), Ce is large medium gray, P is small light gray, and O is black.

framework of the refined structure in P 1. The unit cells are highlighted by squares in the centers. The triclinic structure in (a) is very closely related to the cubic structure, shown

in (b), with cerium atoms occupying the corners and face centers of the unit cell.

Comparing the two images, the slight distortion of the network in (a) illustrates quasi-cubic, i.e., nearly cubic symmetry, with P – O – P bonds bent away from 180°. In (b), the P – O – P bonds are constrained by symmetry to be 180°.

### 3.5.2.2 High Pressure Synchrotron Powder XRD

High pressure synchrotron powder XRD experimental conditions were described fully in Section 2.14. A high pressure synchrotron study was performed on a sample of  $\text{CeP}_2\text{O}_7$  (*KMW230*) using methanol/ethanol pressure transmission medium over the pressure range 0.00 GPa to 10.4 GPa. The data were corrected due to an error in

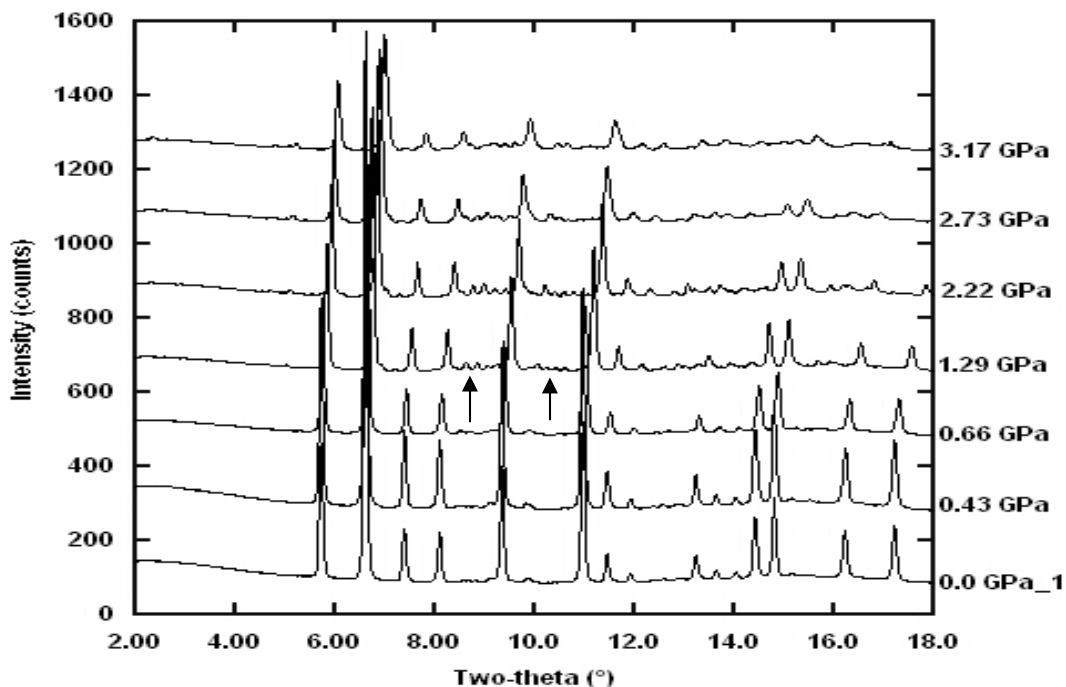


Figure 3.11: Compiled plots of high pressure synchrotron study on  $\text{CeP}_2\text{O}_7$  from the initial “as closed” pressure of 0.00 GPa\_1 to 3.17 GPa. Peak intensities are incremented by 200 counts additively. Appearance of small peaks denoted by arrows at 1.29 GPa.

calibration on the read head of the image plate detector.

Figure 3.11 shows compiled high pressure synchrotron XRD scans from the initial “as-closed” pressure of 0.00 GPa (denoted 0.0 GPa\_1) up to 3.17 GPa. In general, the intensity of peaks decreased and broadened with increasing pressure and peak positions shift to higher two-theta ( $^{\circ}$ ) values, which indicated a reduction in unit cell volume. Peak broadening could be due to strain associated with the changes in the hydrostaticity within the HDAC or further distortion of the unit cell away from cubic.

Some changes in the powder patterns were observed at 1.29 GPa in Figure 3.11 (denoted by arrows) with the appearance of small peaks in the two-theta ( $^{\circ}$ ) ranges 8.5 – 9.3 and 10.2 – 10.7. Examination of individual powder XRD scans at lower pressures, 0.0 GPa and 0.43 GPa, revealed a small increase in the background in the two-theta ( $^{\circ}$ ) range

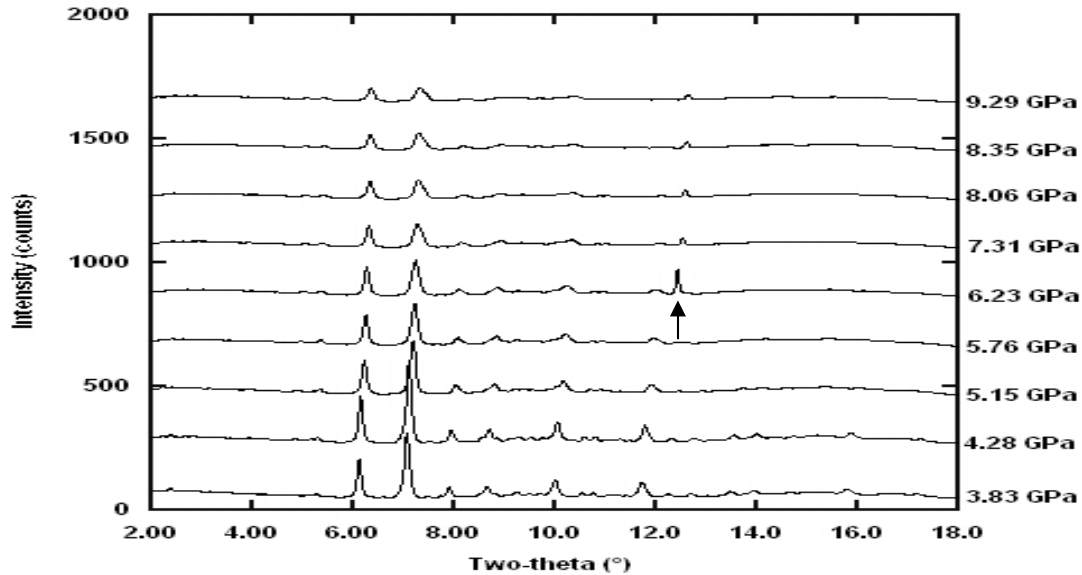


Figure 3.12: Compiled scans of synchrotron powder patterns for increasing pressures. Peak intensity decreases with increasing pressure. Some new peaks disappear; one peak appears at around 12.4 two-theta ( $^{\circ}$ ) at 6.23 GPa, indicated by arrow, is attributed to ruby diffraction. Peak intensities are incremented by 200 counts additively.

8.4 – 9.0, not definitive peaks, and no peaks were found in the two-theta ( $^{\circ}$ ) range 10.0 – 10.6. These observations suggest a phase change at low pressures.

Figure 3.12 shows scans from 3.83 GPa up to 9.29 GPa. As pressure increases, decreasing peak intensities and more peak broadening were observed, which may be associated with partial amorphization of the sample as well as peak positions shifting

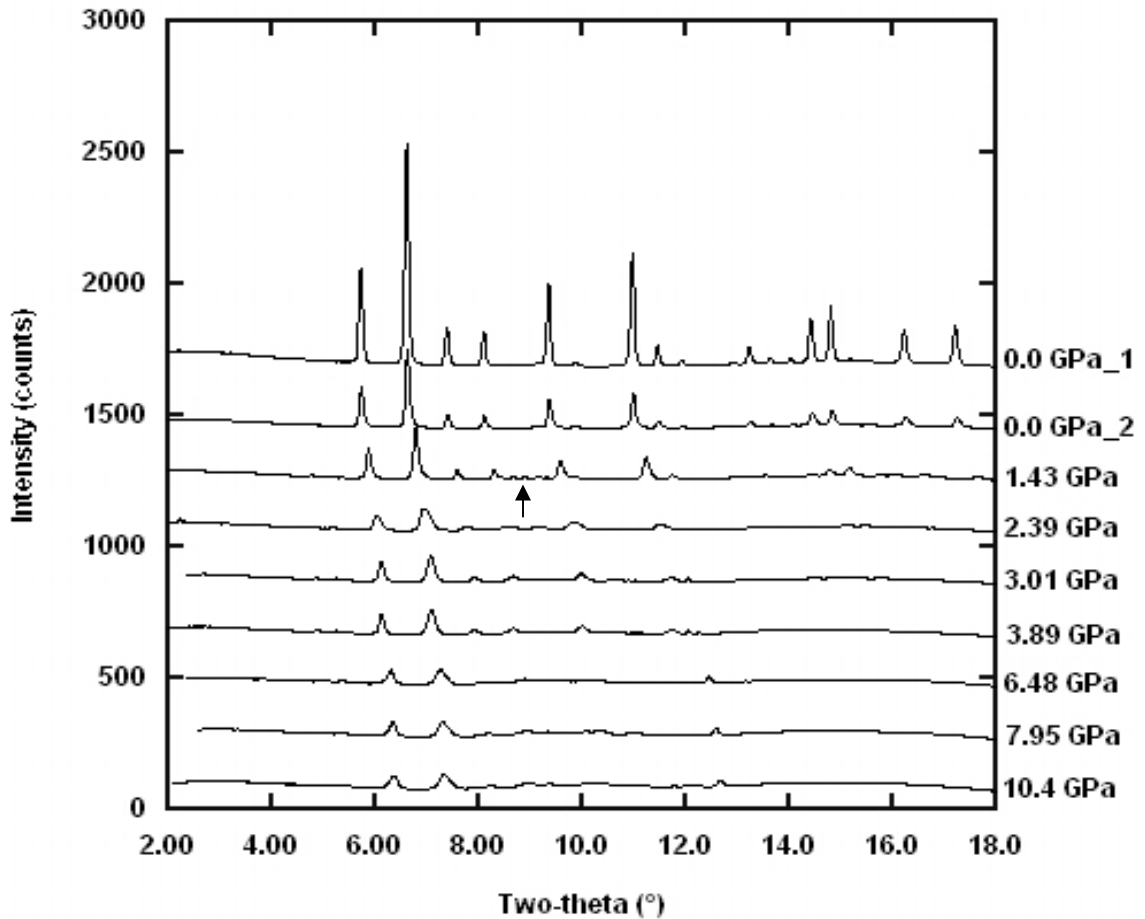


Figure 3.13: Compiled scans of synchrotron powder patterns from the maximum pressure attained, 10.4 GPa, to ambient pressure, designated as 0.0 GPa\_2. The initial “as-closed” scan, labeled 0.0 GPa\_1 is included for comparison. The arrow indicates the appearance of small peaks in the two-theta ( $^{\circ}$ ) range 8.3 – 9.4, which do not appear at the lower pressure (0.0 GPa\_2). Peak intensities are incremented by 200 counts additively.

to higher two-theta ( $^{\circ}$ ) values. The appearance of a single, sharp peak at 6.23 GPa ( $\sim 12.4$  two-theta ( $^{\circ}$ )), was attributed to diffraction from something other than the sample.

The behavior of the sample under decreasing pressures is shown in Figure 3.13, which includes the maximum pressure attained, 10.4 GPa, and the final ambient pressure designated 0.0 GPa\_2. The initial as-closed scan, designated 0.0 GPa\_1, is included for comparison. In general, all peaks shifted to lower two-theta ( $^{\circ}$ ) values, indicating increasing unit cell volume. Comparison of the scans at ambient pressures, 0.0 GPa\_2 and 0.0 GPa\_1, indicated peaks returning to their original positions. However, some peaks at 0.0 GPa\_2 remained broad (at higher two-theta angles) and all were observed to have lower intensity than peaks in the pattern at 0.0 GPa\_1. Partial amorphization of the

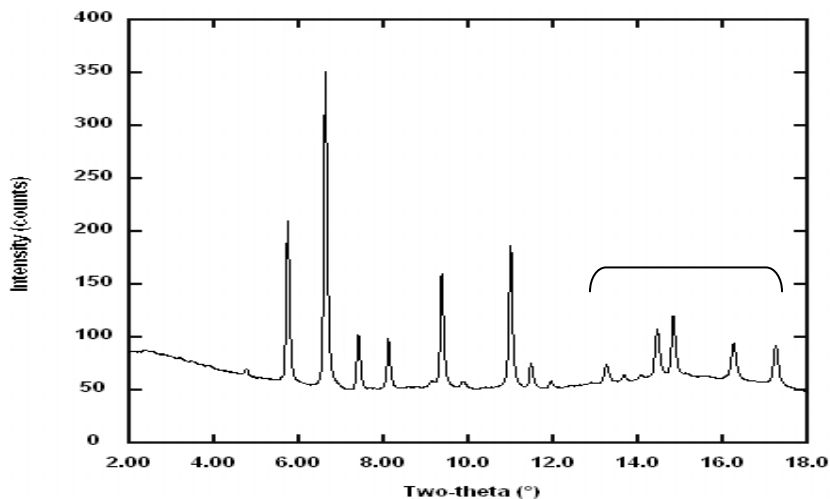


Figure 3.14: Powder XRD scan at final pressure, 0.00 GPa\_2, showing retention of amorphous component (bracketed) that developed at around 2.73 – 3.17 GPa (increasing pressure).

sample appeared to begin between 2.73 GPa and 3.17 GPa under increasing pressure (Figure 3.11) and the sample never recovered complete crystallinity. Figure 3.14 shows

the powder XRD scan at 0.00 GPa<sub>2</sub> indicating the retention of an amorphous component in the sample, the broad hump under higher angle peaks, that is not readily apparent in Figure 3.13.

Interestingly, small peaks appeared at 1.43 GPa in the two-theta (°) range 8.3 – 9.4, indicated by an arrow in Figure 3.13. This pressure and the two-theta (°) range were similar to that observed for the powder XRD scan in Figure 3.11 at 1.29 GPa, which showed increasing intensities of small peaks in the two-theta (°) range 8.5 - 9.3. Notable for their absence at 1.43 GPa, however, were the small peaks previously observed in the

Table 3.6 Pressure (GPa), Refined Lattice Constants (Å), Cell Volumes (Å<sup>3</sup>), and Ruby Peak Widths (nm) for CeP<sub>2</sub>O<sub>7</sub>

Pressure	Lattice Constant	$\sigma$ - LC	FWHM	$\sigma$ - FWHM	Volume	$\sigma$ - V	Ruby Peak Width	$\sigma$ - Ruby
0.0000	8.58086	0.00064	0.08430	0.00020	631.8187	0.14137	-	-
0.4325	8.57781	0.00052	0.07220	0.00030	631.1452	0.11478	0.7538	0.00088
0.6604	8.53509	0.00069	0.07850	0.00020	621.7622	0.15079	0.7777	0.00081
1.2906	8.42169	0.00103	0.07490	0.00020	597.3072	0.21916	0.7621	0.00062
2.2229	8.29057	0.00155	0.07706	0.00030	569.8403	0.31961	0.7989	0.00085
2.7268	8.22354	0.00221	0.09310	0.00090	556.1301	0.44836	0.7623	0.00074
3.1716	8.11263	0.00383	0.08970	0.00040	533.9308	0.75621	0.7179	0.00064
3.8293	8.03658	0.00320	0.09080	0.00040	519.0555	0.62003	0.7417	0.00096
4.2810	7.99471	0.00295	0.08870	0.00050	510.9850	0.56565	0.7350	0.00062
5.1515	7.90909	0.00374	0.10270	0.00070	494.7429	0.70185	0.7301	0.00063
5.7625	7.88202	0.00468	0.10490	0.00080	489.6803	0.87225	0.7392	0.00063
6.2266	7.89884	0.01161	0.10820	0.00100	492.8219	2.17310	0.7667	0.00076
7.3126	7.84979	0.01028	0.11530	0.00140	483.6978	1.90034	0.7581	0.00066
8.0636	7.84616	0.01144	0.12600	0.00010	483.0271	2.11282	0.7581	0.00065
8.3465	7.83250	0.01043	0.13300	0.00020	480.5087	1.91958	0.7976	0.00103
9.2911	7.81139	0.01171	0.13300	0.00010	476.6339	2.14356	0.8503	0.00166
10.3813	7.79134	0.00928	0.16200	0.00020	472.9731	1.69003	0.8298	0.00105
7.9538	7.87002	0.01115	0.15100	0.00030	487.4471	2.07180	0.7587	0.00054
6.4847	7.93108	0.01130	0.13800	0.00030	498.8810	2.13238	0.9821	0.20540
3.8870	8.02179	0.00598	0.10700	0.00020	516.1951	1.15442	1.1807	0.01214
3.0137	8.03441	0.00506	0.10600	0.00010	518.6352	0.97990	1.1863	0.00430
2.3890	8.20660	0.01203	anomalous refinement		552.7004	2.43060	1.2068	0.06601
1.4320	8.39640	0.00185	0.09900	0.00040	591.9423	0.39127	1.2870	0.00675
0.0000	8.56657	0.00098	0.08300	0.00020	628.6674	0.21576	1.1969	0.00142

two-theta (°) range 10.2 – 10.7 at 1.29 GPa (see Figure 3.11). In Figure 3.13, the preceding scan at 2.39 GPa is possibly too high a pressure, and the succeeding scan at

GPa<sub>2</sub> is too low a pressure, for peaks in both two-theta (°) ranges to reappear under pressure reduction. These observations seem to support the earlier suggestion of a possible phase transition at low pressures, and that it might be reversible at similarly low decreasing pressures.

In order to obtain approximate information of how lattice constants change with pressure, Rietveld analysis of the synchrotron scans from the high pressure study were accomplished using TOPAS (Section 2.5.2) and the high temperature cubic form of ZrP<sub>2</sub>O<sub>7</sub> as the model. Cell volumes were obtained from the Rietveld refinement. Other values were refined using a standard least squares method and included FWHM of the first major peak in powder XRD scans at approximately 6.25 two-theta (°) and ruby fluorescence peak widths (see Section 2.14) for all pressures. Table 3.6 shows refined values and standard errors. The anomalous refinement referred to in Table 3.6 is for FWHM values only at 2.389 GPa.

Figure 3.15 shows refined lattice constant and FWHM versus increasing pressure (see Table 3.6). The curve representing lattice constants versus pressure (solid curve) decreased relatively smoothly, but there were some areas in the curve that showed both definite and subtle changes in slope. Of note was a subtle change in slope occurring between 0.66 GPa and 2.22 GPa, indicated in Figure 3.15 with a bold, dashed straight line, that includes the pressure 1.29 GPa, the pressure at which small peaks were observed to appear in the powder XRD scan (Figure 3.11). Based on the evidence from powder XRD scans at 1.29 GPa, 2.22 GPa, 1.43 GPa (decreasing pressure, Figure 3.13), and the slight change in slope of the lattice constant versus pressure curve at low pressures, a phase change in the sample is likely. At 5.15 GPa in Figure 3.15, the lattice constant

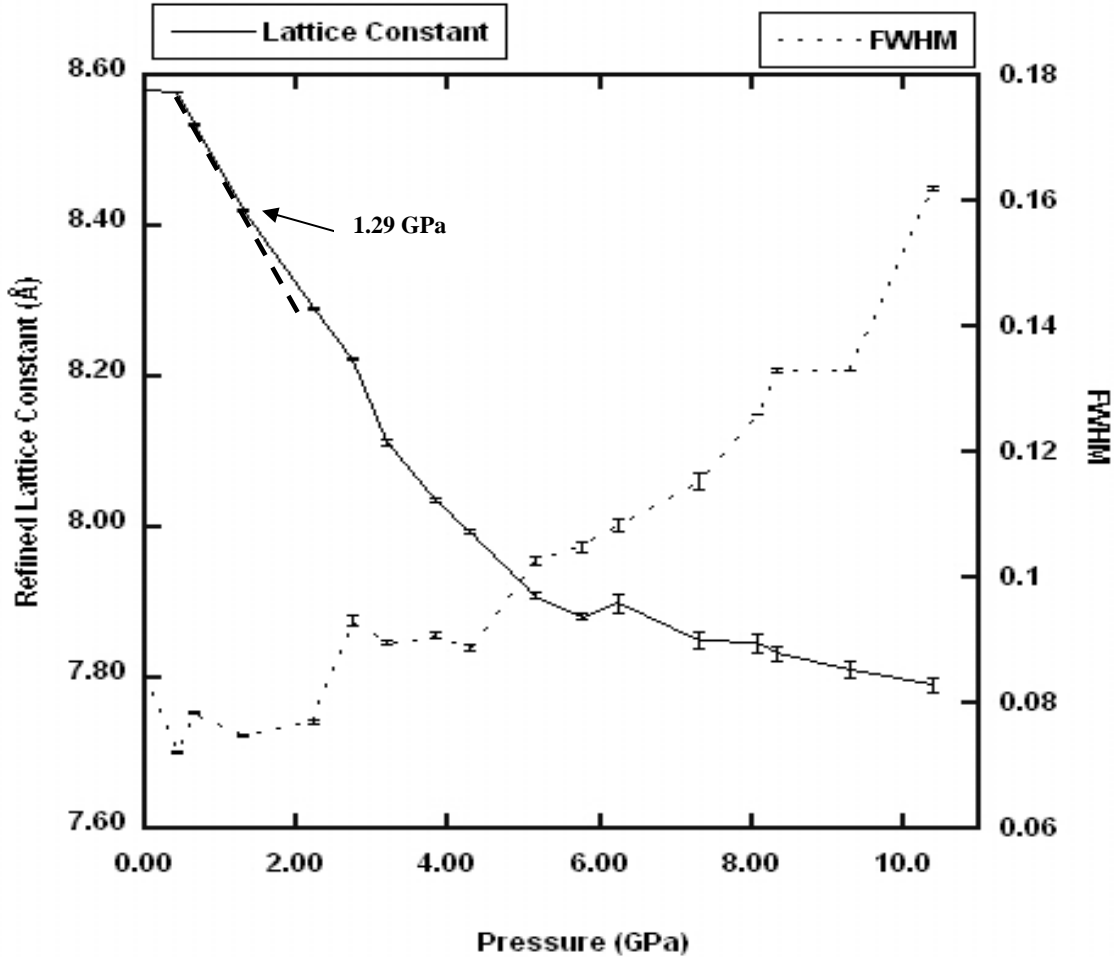


Figure 3.15: Plots of refined lattice constant and FWHM versus pressure for  $\text{CeP}_2\text{O}_7$ . Lattice constant v. pressure curve shows steadily decreasing lattice constants. One subtle change in slope (indicated by bold, dashed line) at 1.29 GPa may indicate a pressure-induced phase change. Error bars are included.

versus pressure curve flattens out. This suggests another possible phase change, though no extra peaks were observed in the powder XRD scans in the pressure range 5.15 GPa – 10.4 GPa.

It is important to note that phase changes in NTE materials at low pressures are not desirable. Use of such materials in the production of composites, for example, often

results in the elimination or reduction of NTE.<sup>56</sup> Some  $A^{IV}M^V_2O_7$  materials exhibit low pressure-induced phase changes at ambient temperature. Cubic  $ZrV_2O_7$  transitions to a pseudo-tetragonal structure between 1.38 - 1.58 GPa;  $HfV_2O_7$  transitions at around  $3.7 \pm 0.3$  GPa to an undetermined structure. On the other hand,  $ZrP_2O_7$  and  $TiP_2O_7$  exhibit no pressure-induced phase changes at ambient temperature.<sup>57, 58</sup>

The FWHM versus pressure curve (dashed curve) in Figure 3.15 did not show any major jumps.

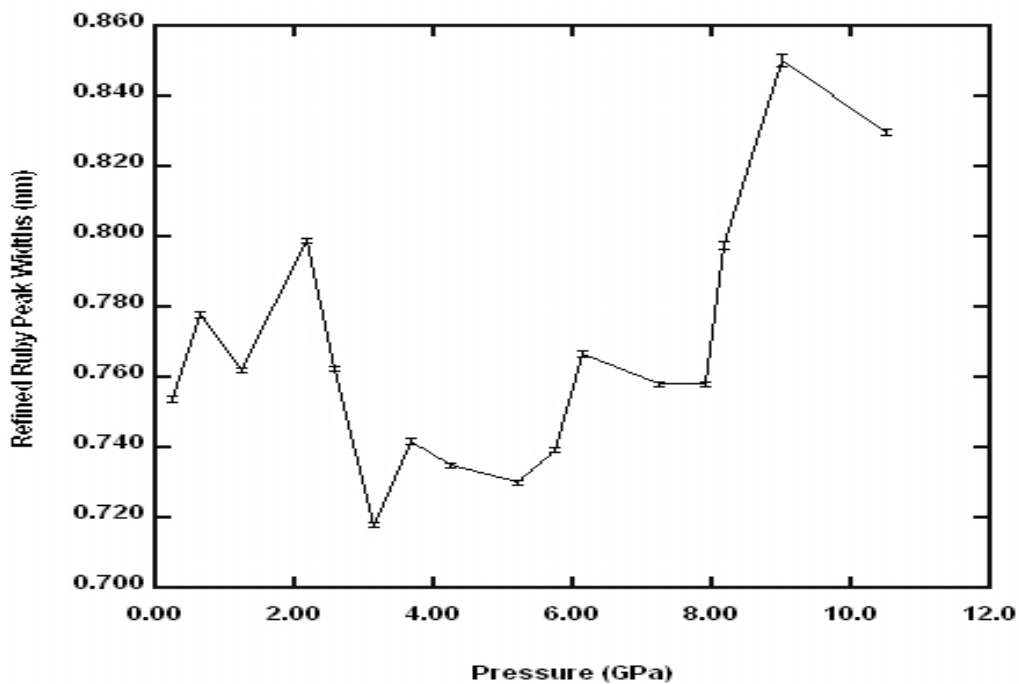


Figure 3.16: Plot of refined peak width for ruby spectra versus pressure. Data reflects measurements prior to scanning of sample. Error bars are included.

Ruby fluorescence peak width versus pressure (Table 3.6) is shown in Figure 3.16. It is known from published works that when pressure gradients and shear stress increase, ruby peak widths increase.<sup>59</sup> Maintaining the fluidity of the methanol/ethanol

transmission medium would likely result in no peak broadening for the ruby, and data shown in Figure 3.16 suggested the methanol/ethanol transmission medium was adequate at pressures less than 8.0 GPa.

Bulk moduli,  $B_0$ , for  $\text{CeP}_2\text{O}_7$  in methanol/ethanol were determined from the slopes of straight lines fit to the data in Figure 3.17. Two bulk moduli were estimated since it was apparent one straight line fit to all data points would be inadequate.  $B_0$  below 4.23 GPa was estimated to be 18.37 GPa, while  $B_0$  between 5.15 GPa and 10.4 GPa was

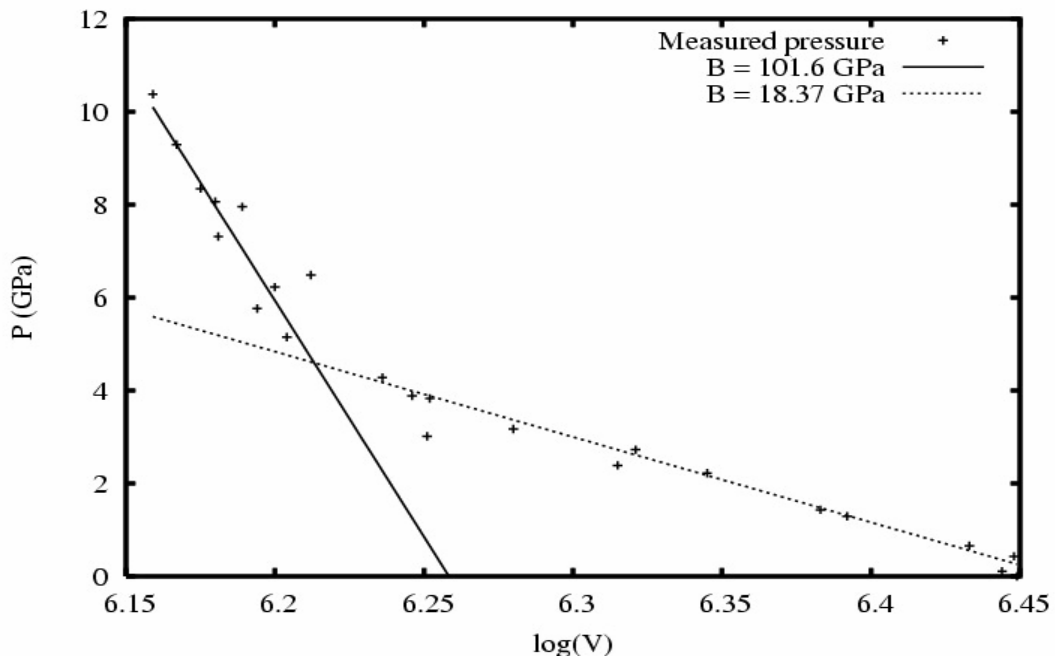


Figure 3.17: Plot of pressure versus the log of volume. Straight lines are fit to two sets of data that reflect obvious differences in decreasing cell volume. The bulk modulus for each straight line fit is shown in the legend.

estimated to be 101.6 GPa.

Low bulk moduli (soft material) are not unusual for NTE materials, probably due

to their flexible, low density frameworks (Section 1.1.1).<sup>56</sup> The  $B_0$  value for  $\text{CeP}_2\text{O}_7$  of 18.37 GPa is not unrealistic when compared to those for other  $\text{A}^{\text{IV}}\text{M}^{\text{V}}_2\text{O}_7$  materials. For example, bulk moduli for  $\text{TiP}_2\text{O}_7$  and  $\text{ZrP}_2\text{O}_7$  were reported to be 42(3) GPa and 39(1) GPa, respectively, while  $\alpha$ - and  $\beta$ - $\text{ZrV}_2\text{O}_7$  (cubic and pseudo-tetragonal, respectively) have bulk moduli of 17.0(7) GPa and 20.8 (10) GPa, respectively.<sup>58</sup>  $\text{HfV}_2\text{O}_7$  has a  $B_0$  of 12.8 ( $\pm 0.04$ ) GPa.<sup>57</sup> In contrast, diamond has a reported bulk modulus of 452 GPa.<sup>60</sup> The estimated bulk modulus of 101.6 GPa for  $\text{CeP}_2\text{O}_7$  above 4.28 GPa was probably due to increasing density of the sample at increasing pressures.

### 3.5.2.3 Thermophysical Properties

In a 1972 work, Alberti, et al. described the mass loss on heating  $\text{Ce}(\text{HPO}_4)_2 \cdot 1.33\text{H}_2\text{O}$ , to give crystalline  $\text{CeP}_2\text{O}_7$ , as resulting from the loss of interstitial and bound water.<sup>35</sup> Differential thermal analysis (DTA) was not performed by Alberti, et al. TG/DTA was accomplished on a sample of  $\text{Ce}(\text{HPO}_4)_2 \cdot x\text{H}_2\text{O}$  (*KMW42*) which indicated similar TG mass losses as those reported by Alberti, et al., but also revealed endotherms related to changes in the precursor during the process producing  $\text{CeP}_2\text{O}_7$ .

Figure 3.18 shows TG/DTA curves for  $\text{Ce}(\text{HPO}_4)_2 \cdot x\text{H}_2\text{O}$ . Numbers 1-4 along the TG (%) curve indicate the major regions of mass loss, and temperatures along the DTA curve are given for the major endotherms. The compound lost approximately 1.875 moles of water up to 95°C represented by region 1 and in region 2, an additional 0.365 moles of water at around 235°C. Around 368°C, 1.08 moles of water were lost. Mass loss at temperatures above 800°C (region 4) was associated with the loss of approximately 0.25 moles of  $\text{O}_2$ . *Ex situ* lab powder XRD scans on another sample of *KMW42* indicated the

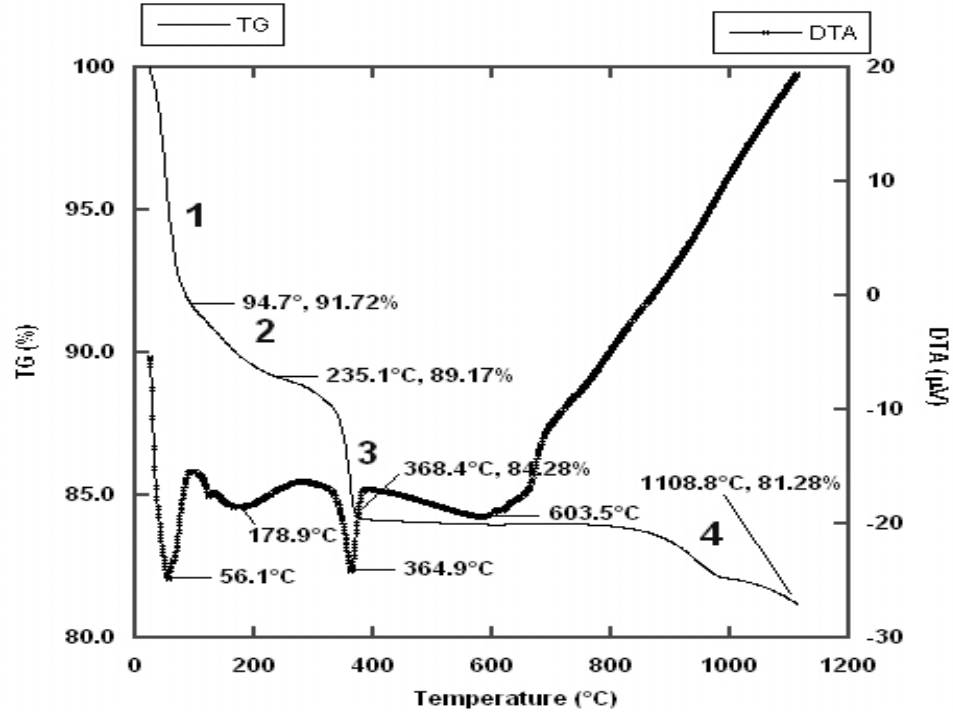
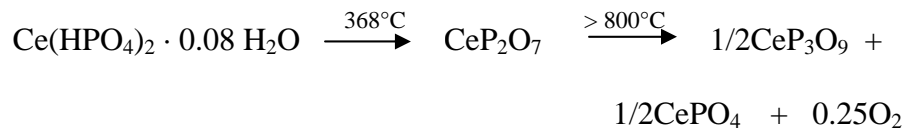


Figure 3.18: TG/DTA of  $\text{Ce}(\text{HPO}_4)_2 \cdot 2.1\text{H}_2\text{O}$ . Heating ramp rate was  $10^\circ\text{C}$  per minute in argon gas; 25-1109°C. Regions 1 – 4 indicate percent mass loss used in calculations.

appearance of degradation products  $\text{CeP}_3\text{O}_9$  and  $\text{CePO}_4$  at temperatures greater than  $750^\circ\text{C}$ . Endotherms appearing in temperature ranges associated with regions 1 - 3 in Figure 3.18 ( $56.1^\circ\text{C}$ ,  $178.9^\circ\text{C}$ , and  $364.9^\circ\text{C}$ ) and mass loss in region 4 suggested the following dehydration process and chemical changes for the precursor:



*Ex situ* lab powder XRD was not accomplished on the TG/DTA sample to confirm the phases suggested at temperatures above 800°C. The sample size used in the TG/DTA was approximately 14 mg and was too small to examine using powder XRD.

In order to determine the actual identity of phases suggested by the TG/DTA analysis, an *in situ* high temperature synchrotron powder XRD dehydration study (the experiment was described in Section 2.1.3) was performed on a sample of cerium dihydrogen phosphate hydrate (KMW232). Figure 3.19 shows a contour plot of the synchrotron data and identification of the phases arising during the dehydration process using JADE and the PDF to match to individual scans at all temperatures explored (25 – 800°C followed by cooling to room temperature). The contour plot represents time elapsed in the dehydration study versus two-theta (°) as synchrotron powder scans are collected continuously at intervals of approximately five minutes. Temperatures are estimated coincident to the time shown on the contour plot by recorded temperatures at the time of the scan and by extrapolating missing temperatures from recorded values. The plot shows intensity of peaks from the top down (as if looking down the z-axis in three-dimensions).

Only two pure phases were found to form (Figure 3.19) that matched JADE PDF cards for  $\text{Ce}(\text{HPO}_4)_2 \cdot 1.33\text{H}_2\text{O}$  and  $\text{Ce}(\text{HPO}_4)_2 \cdot 0.33\text{H}_2\text{O}$  at temperatures below ~ 54°C and 94°C, respectively. The other portions of the contour plot reveal different mixed phases as temperature increases. For example,  $\text{Ce}(\text{HPO}_4)_2$  does not appear as a single phase but appears in trace amounts with  $\text{Ce}(\text{HPO}_4)_2 \cdot 0.33\text{H}_2\text{O}$  between approximately 94 - 280°C and as a coexisting phase with  $\text{CeP}_2\text{O}_7$  (~ 280 – 410°C).  $\text{CeP}_2\text{O}_7$  does not appear as a pure phase between approximately 410 - 625°C, but as a dominant phase along with

trace phases of  $\text{CePO}_4$  and  $\text{CeP}_3\text{O}_9$ . Above  $625^\circ\text{C}$ , two phases of  $\text{CePO}_4$  (one phase was identified as monazite) and  $\text{CeP}_3\text{O}_9$  are dominant along with  $\text{CeP}_2\text{O}_7$ .

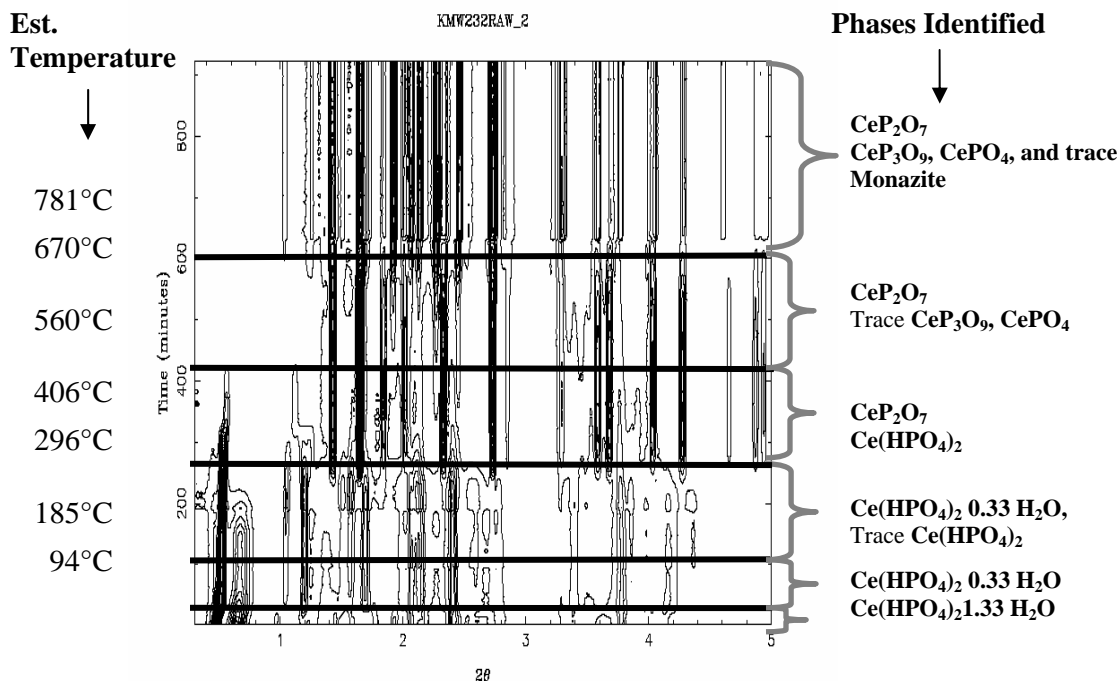


Figure 3.19: Contour plot of *in situ* high temperature synchrotron powder XRD scans for  $\text{Ce}(\text{HPO}_4)_2 \cdot 1.6 \text{H}_2\text{O}$ ; capillary,  $1.3^\circ\text{C}/\text{minute}$  heating ramp rate in argon gas. Estimated temperatures are taken from observed temperatures, ramp rate, and scan times. The Phases Identified column refers to analyses of individual scans at each temperature using powder diffraction database files in JADE. Lines across the plot indicate blocks of contour scans where apparent phase changes occur.

The mixture of phases above approximately  $94^\circ\text{C}$  was probably due to the extremely slow heating ramp rate and rapidity of scans used in this study ( $\sim 1.3^\circ\text{C}/\text{minute}$  and one scan every five minutes); however, all phases have been identified, confirming the process of dehydration of the precursor compound reported by Alberti, et al.,

confirming the degradation products suggested by TG/DTA, and, significantly, revealing no unidentified intermediate phases in the crystallization of  $\text{CeP}_2\text{O}_7$ .

A high temperature *in situ* synchrotron powder XRD thermal expansion study between room temperature and  $750^\circ\text{C}$  was performed on a sample of crystalline  $\text{CeP}_2\text{O}_7$  (KMW232). Full scans at each temperature were not performed in the study; rather,

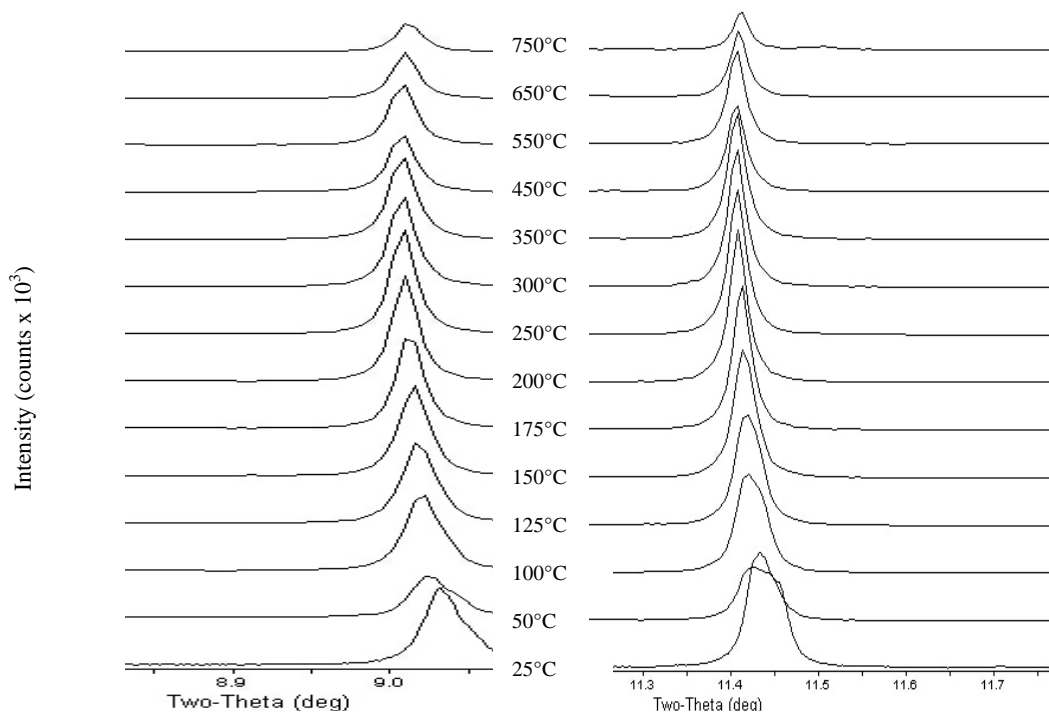


Figure 3.20: Third and fifth major low angle peaks from synchrotron thermal expansion study for all temperatures explored. Low temperature scans show decreasing two-theta ( $^\circ$ ) values; higher temperature scans show increasing two-theta ( $^\circ$ ) values.

regions around major peaks were scanned. Two full scans were conducted, however, at room temperature and at  $300^\circ\text{C}$ .

The third and fifth low angle peaks (at  $\sim 9.03$  and  $11.44$  two-theta ( $^\circ$ ), respectively;  $\lambda = 0.605122 \text{ \AA}$ ) of all synchrotron scans between room temperature and

Table 3.7 Refined Lattice Constants (Å) and Temperature (°C) for CeP<sub>2</sub>O<sub>7</sub> Thermal Expansion Study (ORNL Data)

Temperature (°C)	Refined Lattice Constant (Å)
25	8.57307(15)
55	8.57444(15)
85	8.57625(14)
115	8.57809(14)
145	8.58115(13)
175	8.58615(10)
205	8.58793(11)
235	8.58883(11)
265	8.58976(10)
295	8.59038(11)
325	8.59078(11)
355	8.59113(11)
385	8.59120(11)
415	8.59120(11)
445	8.59127(11)
475	8.59087(11)
505	8.59079(11)
535	8.59037(11)
565	8.59013(11)
595	8.58978(11)
625	8.58908(11)
655	8.58880(11)
685	8.58825(11)
715	8.58735(11)
745	8.58671(12)
775	8.58594(17)
805	8.58545(26)

750°C are shown in Figure 3.20. The behavior of the two peaks with increasing temperature was found to be representative of that for the remaining peaks (not shown). Broad peak shapes and splitting, characteristic of a non-cubic structure, for both peaks at low temperatures were observed. Peaks narrow considerably and intensity increases

around 200°C, suggesting a temperature-induced structural phase transition. This is confirmed by Rietveld refinements using synchrotron scans encompassing the 2-theta range 6.5 to 27.0 (°). Cubic  $ZrP_2O_7$  was used as a model in space group  $P a \bar{3}$  for the refinements. Results showed the high temperature form of  $CeP_2O_7$  was isostructural with this cubic model up to 750°C and non-cubic at temperatures lower than 200°C. Peaks were observed to shift to lower 2-theta (°) values with increasing temperature (see Figure

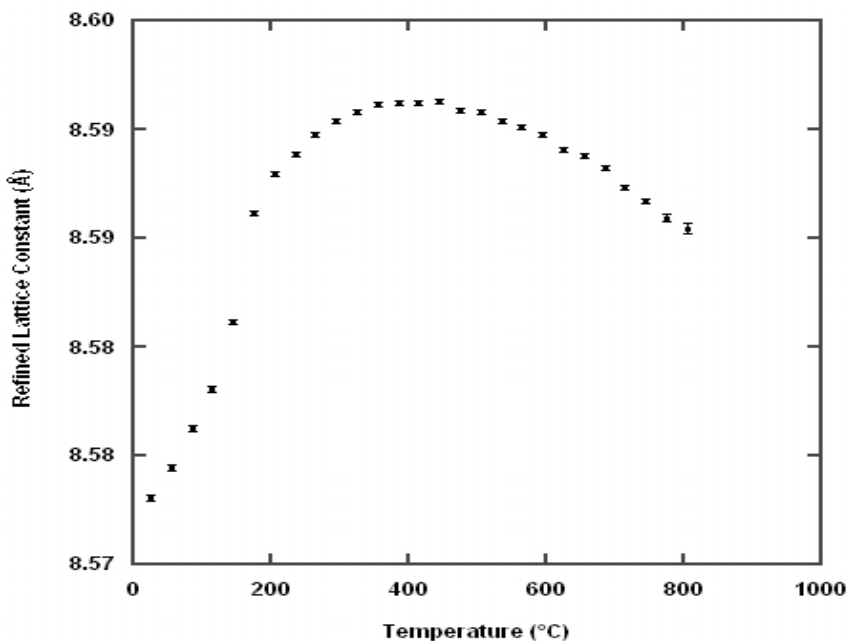


Figure 3.21: Refined lattice constant versus temperature for  $CeP_2O_7$  showing thermal expansion behavior between room temperature and 805°C; error bars are included. Data obtained at Oak Ridge National Labs (ORNL).

3.20), between room temperature and approximately 450°C, indicating positive thermal expansion. At temperatures greater than 450°C, peak positions shifted to higher two-theta (°) values indicating negative thermal expansion.

Cryogenic synchrotron powder XRD was performed on  $\text{CeP}_2\text{O}_7$  in the temperature range 14K to 300K. While no phase changes were observed, the peaks showed slightly larger splittings at 80K and 14K than at higher temperatures (not shown).

In order to calculate coefficients of thermal expansion (CTE), high temperature *in situ* lab powder XRD was performed using a Panalytical X'Pert Pro diffractometer at Oak Ridge National Labs (Section 2.1.1). The temperature range of the study was from room temperature to 805°C, with scans taken of the sample (*KMW232*) at 30°C increments in the range 13 – 140 two-theta (°). Slight impurity phases of  $\text{Ce}^{3+}$  phosphates were observed at two temperatures, 775°C and 805°C.

Refined cubic lattice constant versus temperature from the data obtained are shown in Figure 3.21 and listed in Table 3.7. A CTE value of 10.1 ppm  $\text{K}^{-1}$  was calculated for the temperature range 25 - 205°C. Between 205 - 445°C, a CTE of 2.1 ppm  $\text{K}^{-1}$  was estimated, indicating a transition from high positive to low positive expansion as temperature increases. NTE was observed between 445 – 805°C with a CTE of -1.6 ppm  $\text{K}^{-1}$ . The shift from high positive to low positive thermal expansion occurs in the temperature range between 175 to 205°C, which correlates to the temperature-induced structural phase transition from non-cubic to cubic symmetry observed in the synchrotron study (see Figure 3.20).

Relative to the suggestion by Sleight in his 1998 work,<sup>61</sup> that a trend toward more negative thermal expansion should be observed as  $\text{A}^{4+}$  ionic radii increase in  $\text{A}^{\text{IV}}\text{M}^{\text{V}}_2\text{O}_7$  compounds (Section 1.2.1), the TE behavior of  $\text{CeP}_2\text{O}_7$  ( $\text{Ce}^{4+}$  radius = 0.870 Å) is found to fit between that of lower ionic radius  $\text{Zr}^{4+}$  ( $\text{Zr}^{4+}$  ionic radius = 0.720 Å) and higher ionic radius  $\text{U}^{4+}$  ( $\text{U}^{4+}$  ionic radius = 0.890 Å). Figure 3.22 is a modified version of

Sleight's original figure, enabling the thermal expansion curve for  $\text{CeP}_2\text{O}_7$  to be placed within it to approximate scale.  $\text{CeP}_2\text{O}_7$  exhibited high thermal expansion and a phase

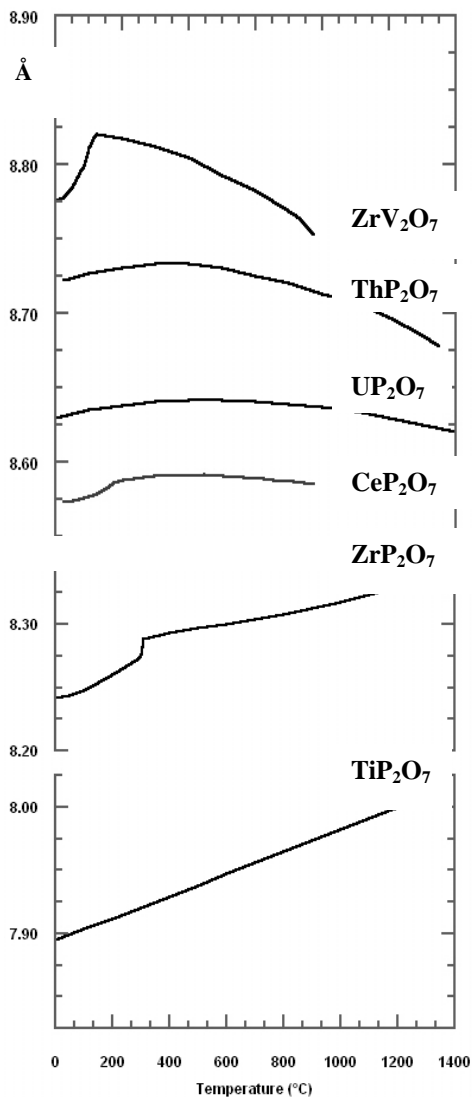


Figure 3.22: Modified figure from Sleight<sup>61</sup> with TE curve of  $\text{CeP}_2\text{O}_7$  fit to approximate scale.

transition to low thermal expansion ( $\sim 200^\circ\text{C}$ ) like that observed for  $\text{ZrP}_2\text{O}_7$ , though at a lower temperature, and low positive and NTE like that of  $\text{UP}_2\text{O}_7$ . From these data, it can

be concluded  $\text{CeP}_2\text{O}_7$  fits the trend suggested by Sleight with characteristics intermediate between those of  $\text{ZrP}_2\text{O}_7$  and  $\text{UP}_2\text{O}_7$ .

### 3.6 Synthesis and Thermophysical Properties of $\text{PbP}_2\text{O}_7$ (KMW311)

Lead pyrophosphate is another  $\text{A}^{\text{IV}}\text{M}^{\text{V}}_2\text{O}_7$  compound for which thermal expansion data is not available in the literature. The compound has previously been synthesized by a few different methods. The method reported by Peyronel involved the preparation of a sol using  $\text{PbO}_2$  and  $\text{H}_3\text{PO}_4$  with firing the mixture at  $300^\circ\text{C}$ .  $\text{PbO}_2$  impurities were removed by decanting the product with water.<sup>62</sup> Chernorukov, Frydrych and Lohoff, and Bruque, et al. reported the synthesis of  $\text{PbP}_2\text{O}_7$  using lead acetate under reflux using different concentrations of phosphoric acid.<sup>1, 63, 64</sup> The structure of  $\text{PbP}_2\text{O}_7$  has been reported as cubic or quasi-cubic with  $a = 8.01 \pm 0.01 \text{ \AA}$  (Peyronnel, 1942), and as a cubic superlattice with  $a = 24.10 \pm 0.003 \text{ \AA}$  (Völlenkle, et al., 1963).<sup>32, 62</sup>

#### 3.6.1 Experimental

$\text{PbP}_2\text{O}_7$  was synthesized using low temperature reflux in a variation on the works of Bruque, et al.<sup>64</sup> and Chernorukov.<sup>1</sup> Preparation included the recrystallization of lead acetate using hot glacial acetic acid, forming long, translucent crystals that were stored in the argon atmosphere of a glove box. A 0.2 M solution of lead acetate was prepared by quickly transferring recrystallized lead acetate (8.8674 g, 20 mmol) via a solid transfer funnel into a 100 mL volumetric flask containing several mL of glacial acetic acid with swirling, and then filling the flask to volume. The contents were heated between  $80 - 100^\circ\text{C}$  with stirring until the lead acetate dissolved leaving a clear, pale yellow solution.

50 mL of the 0.2 M solution of warm lead acetate was added to a three-neck round bottom flask set up for reflux with a cold water condenser. 100 mL of a freshly prepared 5.0 M phosphoric acid solution was transferred to the flask with stirring, immediately followed by the addition of 12 mL distilled water. The result was a white, cloudy mixture, which was allowed to reflux between 85 – 90°C for thirty-seven hours. The resulting white material was washed with ethanol, cold glacial acetic acid, and anhydrous acetone on a glass frit funnel under water aspiration. The wet powder was permitted to dry under water aspiration for two hours and then covered with a watch glass for overnight drying. 2.9761 g of  $\text{Pb}(\text{HPO}_4)_2 \cdot \text{H}_2\text{O}$  were produced. Heat treatments were accomplished using a tube furnace under oxygen flow at 320°C and in air in a box furnace beginning at 300°C in 10°C increments up until 360°C, each heat treatment was 24 hours in duration.  $\text{PbP}_2\text{O}_7$  was found to crystallize at 320°C after heating in the tube furnace and was found to degrade to  $\text{Pb}(\text{PO}_3)_2$  upon heating above 350°C after heating in a normal furnace.

Lab powder XRD confirmed the product of the reflux was  $\text{Pb}(\text{HPO}_4) \cdot \text{H}_2\text{O}$  and the crystallized product was  $\text{PbP}_2\text{O}_7$ . Rietveld refinement was performed on a laboratory powder XRD scan using the cubic  $\text{ZrP}_2\text{O}_7$  model; fitted  $wRp = 7.87\%$ , reduced  $\chi^2 = 1.904$ .

### **3.6.2 Results and Discussion**

Rietveld refinement was performed over the entire two-theta (°) range (13.0 – 140.0) of the room temperature powder pattern for  $\text{PbP}_2\text{O}_7$  obtained at Oak Ridge National Laboratory. Refined fractional atom coordinates are shown in Table 3.8, and

refined bond distances and angles are shown in Table 3.9. Shown in Figure 3.23 is a zoom image of the refined data in the two-theta ( $^{\circ}$ ) range 15.0 – 56.0. Of significance in this range were several peaks that did not belong to the simple cubic cell, indicated by arrows in Figure 3.23. These peaks could not be matched to possible impurity phases using the PDF file.

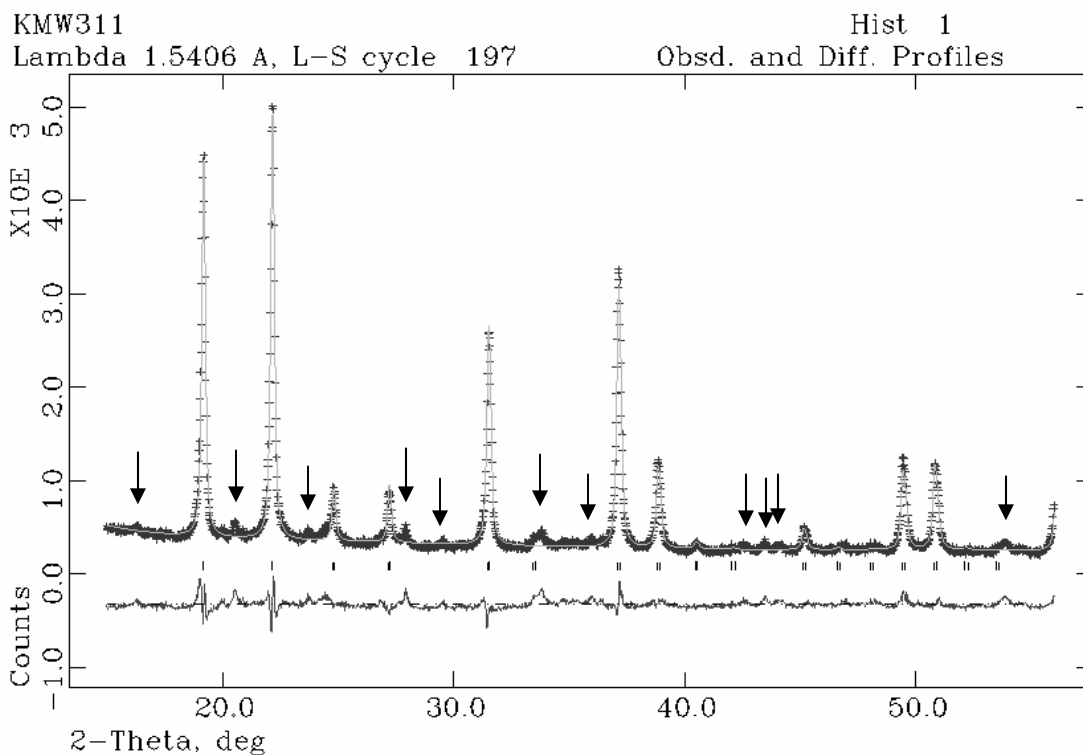


Figure 3.23: Zoom image of two-theta ( $^{\circ}$ ) range 15.0 – 56.0. Crosses on peaks represent experimental data. Outline of peak shapes represent refined data. Vertical lines are reflections for  $P\bar{3}$  space group. Lower curve is difference pattern between refined and experimental data. Arrows indicate un-modeled peaks.

In Table 3.8, Uiso thermal factors for O3 and O4 uncharacteristically high values. On the other hand, Table 3.9 lists Pb – O bond distances found to be within acceptable values. For example, the Pb1 – O3 length of 2.156(9) Å is within the range found in

Table 3.8 Fractional Coordinates for PbP<sub>2</sub>O<sub>7</sub> from Rietveld Refinement; ZrP<sub>2</sub>O<sub>7</sub> Model

Atom	x	y	z	Uiso
Pb1	0.000000	0.000000	0.000000	3.533
σ				0.051
P2	0.395190	0.395190	0.395190	4.930
σ	0.000520	0.000520	0.000520	0.340
O3	0.446202	0.234004	0.380071	13.870
σ	0.001332	0.001022	0.001600	0.573
O4	0.500000	0.500000	0.500000	13.870
σ				0.573

literature which give Pb – O distances of 1.954(15) Å– 2.310(21) Å).<sup>64</sup> However, the P3 – O3 distance of 1.363(9) was observed to be smaller than what would be expected for P – O links (1.44 Å – 1.66 Å). This observation, along with extra peaks in the powder pattern, suggested the cubic ZrP<sub>2</sub>O<sub>7</sub> model used in the refinement is inadequate to describe the structure of PbP<sub>2</sub>O<sub>7</sub>.

A lab powder diffraction thermal expansion study (Section 2.1.1) was performed on a sample of PbP<sub>2</sub>O<sub>7</sub> at Oak Ridge National Labs. Data were analyzed using X'Pert High Score Plus Rietveld program and a cubic ZrP<sub>2</sub>O<sub>7</sub> model. The thermal expansion curve for PbP<sub>2</sub>O<sub>7</sub> is shown in Figure 3.24 and refined lattice constant values in Table3.10. The compound exhibited high positive expansion behavior over the temperature range studied.

The CTE for PbP<sub>2</sub>O<sub>7</sub>, in the temperature range 25 – 340°C, was estimated to be 11.9 ppm K<sup>-1</sup>, which was between that of ZrP<sub>2</sub>O<sub>7</sub>, CTE (25 – 293°C) = 13.7 ppm K<sup>-1</sup> (from data supplied by J. S. O. Evans) and that of CeP<sub>2</sub>O<sub>7</sub>, CTE (25 – 205°C) = 10.1 ppm K<sup>-1</sup>. Comparing the thermal behavior of PbP<sub>2</sub>O<sub>7</sub> (Pb<sup>4+</sup> ionic radius = 0.775 Å) to that of

Table 3.9 Bond Distances and Angles from Refinement of PbP<sub>2</sub>O<sub>7</sub>

<b>Vector</b>	<b>Length</b>	<b>Optr Cell</b>	<b>Neighbor atom coordinates</b>		
PB1_P2	3.3902(18)	4-1 0 0	-0.10481	0.39519	0.10481
PB1_P2	3.3902(18)	5 0-1 0	0.10481	-0.10481	0.39519
PB1_P2	3.3902(18)	6 0 0-1	0.39519	0.10481	-0.10481
PB1_P2	3.3902(18)	7 0-1 0	-0.39519	-0.10481	0.10481
PB1_P2	3.3902(18)	8 0 0-1	0.10481	-0.39519	-0.10481
PB1_P2	3.3902(18)	9-1 0 0	-0.10481	0.10481	-0.39519
PB1_O3	2.156(9)	4-1 0 0	-0.05380	0.23400	0.11993
PB1_O3	2.156(9)	5 0-1 0	0.11993	-0.05380	0.23400
PB1_O3	2.156(9)	6 0 0-1	0.23400	0.11993	-0.05380
PB1_O3	2.156(9)	-4 1 0 0	0.05380	-0.23400	-0.11993
PB1_O3	2.156(9)	-5 0 1 0	-0.11993	0.05380	-0.23400
PB1_O3	2.156(9)	-6 0 0 1	-0.23400	-0.11993	0.05380
<b>Angle</b>					
O3_PB1_O3	82.8(5)	4-1 0 0	5 0-1 0		
O3_PB1_O3	82.8(5)	4-1 0 0	6 0 0-1		
O3_PB1_O3	179.980(0)	4-1 0 0	-4 1 0 0		
O3_PB1_O3	97.2(5)	4-1 0 0	-5 0 1 0		
O3_PB1_O3	97.2(5)	4-1 0 0	-6 0 0 1		
O3_PB1_O3	82.8(5)	5 0-1 0	6 0 0-1		
O3_PB1_O3	97.2(5)	5 0-1 0	-4 1 0 0		
O3_PB1_O3	179.980(0)	5 0-1 0	-5 0 1 0		
O3_PB1_O3	97.2(5)	5 0-1 0	-6 0 0 1		
O3_PB1_O3	97.2(5)	6 0 0-1	-4 1 0 0		
O3_PB1_O3	97.2(5)	6 0 0-1	-5 0 1 0		
O3_PB1_O3	179.980(0)	6 0 0-1	-6 0 0 1		
O3_PB1_O3	82.8(5)	-4 1 0 0	-5 0 1 0		
O3_PB1_O3	82.8(5)	-4 1 0 0	-6 0 0 1		
O3_PB1_O3	82.8(5)	-5 0 1 0	-6 0 0 1		
<b>Vector</b>					
P2_PB1	3.3902(18)	4 0 0 0	0.50000	0.00000	0.50000
P2_PB1	3.3902(18)	5 0 0 0	0.50000	0.50000	0.00000
P2_PB1	3.3902(18)	6 0 0 0	0.00000	0.50000	0.50000
P2_P2	2.916(14)	-1 1 1 1	0.60481	0.60481	0.60481
P2_O3	1.363(9)	1 0 0 0	0.44620	0.23400	0.38007
P2_O3	1.363(9)	2 0 0 0	0.38007	0.44620	0.23400
P2_O3	1.363(9)	3 0 0 0	0.23400	0.38007	0.44620
P2_O4	1.458(7)	1 0 0 0	0.50000	0.50000	0.50000
<b>Angle</b>					
O3_P2_O3	103.2(7)	1 0 0 0	2 0 0 0		
O3_P2_O3	103.2(7)	1 0 0 0	3 0 0 0		
O3_P2_O4	115.2(6)	1 0 0 0	1 0 0 0		
O3_P2_O3	103.2(7)	2 0 0 0	3 0 0 0		
O3_P2_O4	115.2(6)	2 0 0 0	1 0 0 0		
O3_P2_O4	115.2(6)	3 0 0 0	1 0 0 0		
<b>Vector</b>					
O3_PB1	2.156(9)	4 0 0 0	0.50000	0.00000	0.50000
O3_P2	1.363(9)	1 0 0 0	0.39519	0.39519	0.39519
O3_O3	2.136(14)	2 0 0 0	0.38007	0.44620	0.23400
O3_O3	2.136(14)	3 0 0 0	0.23400	0.38007	0.44620
<b>Angle</b>					
PB1_O3_P2	148.0(9)	4 0 0 0	1 0 0 0		
<b>Vector</b>					
O4_P2	1.458(7)	1 0 0 0	0.39519	0.39519	0.39519
O4_P2	1.458(7)	-1 1 1 1	0.60481	0.60481	0.60481
<b>Angle</b>					
P2_O4_P2	180.000(0)	1 0 0 0	-1 1 1 1		

Table 3.10 Temperature (°C) and Refined Lattice Constants (Å) for PbP<sub>2</sub>O<sub>7</sub>

<b>Temperature</b>	<b>Lattice Constant</b>
25	8.0322(1)
55	8.0348(1)
85	8.0376(1)
115	8.0403(1)
145	8.0432(1)
175	8.0460(1)
205	8.0491(1)
235	8.0520(1)
265	8.0547(1)
295	8.0574(1)
325	8.0605(1)
340	8.0624(1)

ZrP<sub>2</sub>O<sub>7</sub> (Zr<sup>4+</sup> ionic radius 0.720 Å) and CeP<sub>2</sub>O<sub>7</sub> (Ce<sup>4+</sup> ionic radius 0.870 Å) using Figures 3.22 and 3.24, it was observed that PbP<sub>2</sub>O<sub>7</sub> does not exhibit structural phase changes like that for zirconium and cerium pyrophosphates (~290°C and ~200°C, respectively). The compound displayed thermal behavior more like that observed for TiP<sub>2</sub>O<sub>7</sub> (Ti<sup>4+</sup> ionic radius = 0.605 Å) showing linear thermal expansion in the temperature range studied. TiP<sub>2</sub>O<sub>7</sub> has a supercell<sup>40</sup> and the compound does not exhibit a phase transition between room temperature and 1000°C (Figure 3.22). The refined room temperature lattice constant for PbP<sub>2</sub>O<sub>7</sub>, 8.03 Å, is small compared to that for ZrP<sub>2</sub>O<sub>7</sub> (8.24 Å) and CeP<sub>2</sub>O<sub>7</sub> (~ 8.58 Å), and is comparable to that of TiP<sub>2</sub>O<sub>7</sub> (~7.90 Å). Considering the ionic radius of Pb<sup>4+</sup>, the lattice constant for PbP<sub>2</sub>O<sub>7</sub> was expected to have a value between that of ZrP<sub>2</sub>O<sub>7</sub> and CeP<sub>2</sub>O<sub>7</sub>.

Further studies would be required to determine an adequate unit cell and the origin of the small lattice constant for PbP<sub>2</sub>O<sub>7</sub>. Based on the lattice constant, rather than

on the size of the  $\text{Pb}^{4+}$  cation, it can be concluded that the thermal behavior of  $\text{PbP}_2\text{O}_7$  is more like  $\text{TiP}_2\text{O}_7$  than its  $\text{A}^{\text{IV}}$  cation neighbors.

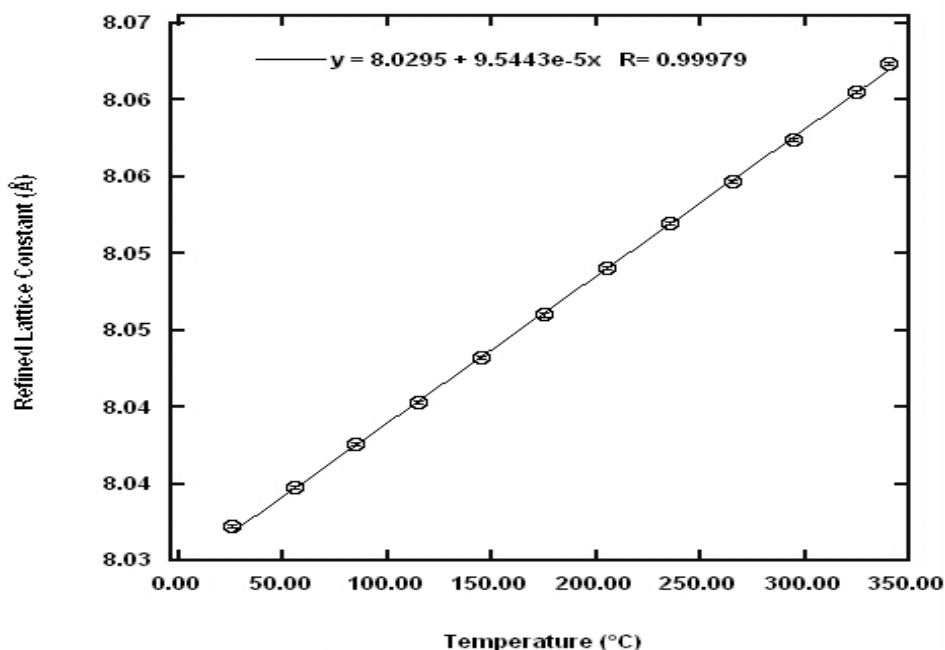


Figure 3.24: Lattice constant versus temperature curve for  $\text{PbP}_2\text{O}_7$  from *in situ* thermal expansion study at ORNL (25 – 340°C). A linear curve is fit to the data points showing a high degree of linearity based on the R value of 0.99979. Error bars are included. All sigma values are 0.0001 for lattice constants.

### 3.7 Conclusion

Non-hydrolytic sol-gel methods provided an alternative route in the synthesis of  $\text{ZrP}_2\text{O}_7$  and  $\text{ZrV}_2\text{O}_7$ . While temperatures of crystallization for the compounds did not show improvement compared to other synthesis methods, the method could be a potential avenue for use in the preparation of solid solutions, for example, using  $\text{ZrP}_2\text{O}_7$  or  $\text{ZrV}_2\text{O}_7$  as parent compounds.

Direct synthesis from simple starting materials using mild autoclave techniques was shown to eliminate the step of preparing a-ZrP gel as a precursor and resulted in the direct synthesis of crystalline  $\text{ZrP}_2\text{O}_7$ . This method appears to be an attractive alternative for the synthesis other low positive and negative thermal expansion materials.

Evidence obtained from structural studies demonstrated room temperature  $\text{CeP}_2\text{O}_7$  was not a simple cubic or a cubic superlattice as cited in literature. Triclinic symmetry with quasi-cubic lattice constants seems likely. The structure was refined using the Rietveld method; however, a high quality model was not established.

Two pressure-induced phase transitions seem likely at approximately 1.29 GPa and at approximately 5.15 GPa for  $\text{CeP}_2\text{O}_7$ . The onset of amorphization began at moderate pressures, and, though the material regained most of its crystalline nature on decompression, it never achieved the state of crystallinity observed in the initial experimental sample. The material was found to be soft at low pressures, with a bulk modulus estimated to be 18.37 GPa; at above ~5 GPa, the bulk modulus was approximately 101.6 GPa.

Thermal studies on  $\text{CeP}_2\text{O}_7$  showed a temperature-induced structural phase transition from non-cubic to cubic symmetry at around 200°C. The thermal expansion behavior of the compound fit the trend of  $\text{A}^{\text{IV}}\text{M}^{\text{V}}_2\text{O}_7$  compounds of increasing NTE with increasing  $\text{A}^{\text{IV}}$  ionic radii, exhibiting both high positive expansion at lower temperatures, like that observed for  $\text{ZrP}_2\text{O}_7$ , and negative thermal expansion at higher temperatures, like that observed for  $\text{UP}_2\text{O}_7$ .

Due to its low degradation temperature, thermal studies on  $\text{PbP}_2\text{O}_7$  encompassed a limited temperature range (25 – 340°C). The expansion behavior of the compound was

found to be linear with a high positive CTE in the temperature range studied, and much like that of  $\text{TiP}_2\text{O}_7$ . It was observed to have an unexpectedly small room temperature lattice constant. It appeared further study was needed to determine the cause of the small lattice constant and an adequate structure for  $\text{PbP}_2\text{O}_7$ .

### 3.8 References

1. Chernorukov, N. G., Thermal Stability of Lead(IV) Acid Phosphates and Arsenates. *Inorganic Materials* 1977, 13, 1371-1374.
2. Livage, J. B. F.; Chatry, M.; Coury, L., Sol-Gel Synthesis and NMR Characterization of Ceramics. *Ceramics International* 1997, 23, 13-18.
3. Brinker, C. J.; Scherer, G. W., *SOL-GEL SCIENCE: The Physics and Chemistry of Sol-Gel Processing*. Academic Press: 1990.
4. Livage, J., Sol-gel synthesis of heterogeneous catalysts from aqueous solutions. *Catalysis Today* 1998, 41, 3-19.
5. Arnal, P.; Corriu, R. J. P.; Leclercq, D.; Mutin, P. H.; Vioux, A., Preparation of transition metal oxides by a nonhydrolytic sol-gel Process. *Mat. Res. Soc. Symp. Proc.* 1994, 346, 339-344.
6. Vioux, A., Nonhydrolytic Sol-Gel Routes to Oxides. *Chem. Mater.* 1997, 9, 2292-2299.
7. Andrianainarivelo, M.; Corriu, R. J. P.; Leclercq, D.; Mutin, P. H.; Vioux, A., Non-hydrolytic sol-gel process: zirconium titanate gels. *J. Mater. Chem.* 1997, 7, 279-284.
8. Andrianainarivelo, M.; Corriu, R.; Leclercq, D.; Mutin, P. H.; Vioux, A., Mixed Oxides  $\text{SiO}_2\text{-ZrO}_2$  and  $\text{SiO}_2\text{-TiO}_2$  by a non-hydrolytic sol-gel route. *J. Mater. Chem.* 1996, 6, 1665-1671.
9. Lafond, V.; Mutin, P. H.; Vioux, A., Non-hydrolytic sol-gel routes based on alkyl halide elimination: toward better mixed oxide catalysts and new supports Application to the preparation of a  $\text{SiO}_2\text{-TiO}_2$  epoxidation catalyst. *Journal of Molecular Catalysis A: Chemical* 2002, 182-183, 81-88.
10. Andrianainarivelo, M.; Corriu, R. J. P.; Leclercq, D.; Mutin, P. H.; Vioux, A., Nonhydrolytic Sol-Gel Process: Aluminum Titanate Gels. *Chem. Mater.* 1997, 9, 1098-1102.
11. Andrianainarivelo, M.; Corriu, R. J. P.; Leclercq, D.; Mutin, P.; Vioux, A., Nonhydrolytic Sol-Gel Process: Aluminium and Zirconium Titanate Gels. *J. Sol-Gel Sci. Technol.* 1997, 8, 89-93.
12. Acosta, S.; Corriu, R. J. P.; Leclercq, D.; Mutin, P. H.; Vioux, A., Monophasic pre-mullite gels prepared by a nonhydrolytic process. *Mat. Res. Soc. Symp. Proc.* 1994, 346, 345-350.

13. Corriu, R.; Leclercq, D.; Lefevre, P.; Mutin, p. H.; Vioux, A., Preparation of Monolithic Binary Oxide gels by a Nonhydrolytic Sol-gel process. *Chem. Mater.* 1992, 4, 961-963.
14. Acosta, S.; Corriu, R. J. P.; Leclercq, D.; Lefevre, P.; Mutin, P. H.; Vioux, A., Preparation of alumina gels by anon-hydrolytic sol-gel processing method. *Journal of Non-Crystalline Solids* 1994, 170, 234-242.
15. Arnal, P.; Corriu, R. J. P.; Leclercq, D.; Mutin, P. H.; Vioux, A., Preparation of anatase, brookite and rutile at low temperatures by non-hydrolytic sol-gel methods. *J. Mater. Chem.* 1996, 6, 1925-1932.
16. Gerrard, W.; Griffey, P. F., A Novel Preparation of Boron Phosphate. *Chemistry and Industry* January 10th, 1959, 1959, p 55.
17. Yamaguchi, O. T. D.; Kawabata, H.; Shimizu, K., Formation and Transformation of WO<sub>3</sub> Prepared from Alkoxide. *J. Am. Ceram. Soc.* 1987, 70, (5), C-94-C-96.
18. Gerrard, W. K.; Kilburn, D., Correlation between Reactivity of the 1-Carbon Atom in Alcohols, and Certain Properties of Alkoxysilanes. *Journal of the Chemical Society* 1956, 1536-1539.
19. Wilkinson, A. P.; Lind, C.; Pattanaik, S., A New Polymorph of ZrW<sub>2</sub>O<sub>8</sub> Prepared using Nonhydrolytic Sol-Gel Chemistry. *Chem. Mater.* 1999, 11, 101-108.
20. Di Vona, M. L.; Traversa, E.; Licoccia, S., Nonhydrolytic Synthesis of NASICON of Composition Na<sub>3</sub>Zr<sub>2</sub>Si<sub>2</sub>PO<sub>12</sub>. *Chemistry of Materials* 2001, 13, 141-144.
21. Barz, R. U.; Grassl, M.; Gille, P., Growth of Gallium Orthophosphate Single Crystals under Hydrothermal Synthesis. *Cryst. Res. Technol.* 1999, 34, (9), 1121-1127.
22. Corriu, R. J. P.; Leclercq, D.; Lefevre, P.; Mutin, P. H.; Vioux, A., Preparation of Monolithic Metal Oxide Gels by a Non-hydrolytic Sol-Gel Process. *J. Mater. Chem.* 1992, 2, 673-674.
23. Korthuis, V.; Khosrovani, N.; Sleight, A. W.; Roberts, N.; Dupree, R.; Warren, W. W., Negative Thermal Expansion and Phase Transitions in the ZrV<sub>2-x</sub>P<sub>x</sub>O<sub>7</sub> Series. *Chem. Mater.* 1995, 7, 412-417.
24. Harrison, D. E.; McKinstry, H. A.; Hummel, F. A., High-Temperature Zirconium Phosphates. *J. Am. Ceram. Soc.* 1954, 37, 277-280.
25. Clearfield, A.; Stynes, J., The Preparation of Crystalline Zirconium Phosphate and Some Observations on its Ion Exchange Behaviour. *J. Inorg. Nucl. Chem.* 1964, 26, 117-129.

26. Khosrovani, N.; Sleight, A. W.; Vogt, T., Structure of  $ZrV_2O_7$  from -263 to 470 °C. *J. Solid State Chem.* 1997, 132, 355-360.
27. Baran, E. J., The unit cell of hafnium divanadate. *J. Less Common Met.* 1976, 46, 343-345.
28. Buchanan, R. C.; Wolter, G. W., Properties of Hot-Pressed Zirconium Pyrovanadate Ceramics. *J. Electrochem. Soc.* 1983, 130, 1905-1910.
29. Krogh Anderson, A. M.; Norby, P.; Hanson, J. C.; Vogt, T., Preparation and Characterization of a New 3-Dimensional Zirconium Hydrogen Phosphate,  $\tau$ - $Zr(HPO_4)_2$ ; Determination of the Complete Crystal Structure by Combining Synchrotron X-ray Crystal Diffraction and Neutron Powder Diffraction. *Inorg. Chem.* 1998, 37, 876-881.
30. Birkedal, H.; Krogh Andersen, A. M.; Arakcheeva, A.; Chapuis, G.; Norby, P.; Pattison, P., The Room-Temperature Superstructure of  $ZrP_2O_7$  is Orthorhombic: There Are No Unusual 180° P - O - P Bond Angles. *Inorg. Chem.* 2006, 45, 4346-4351.
31. Losilla, E. R.; Cabeza, A.; Bruque, S.; Aranda, M. A. G.; Sanz, J.; Iglesias, J. E.; Alonso, J. A., Syntheses, Structures, and Thermal Expansion of Germanium Pyrophosphates. *J. Solid State Chem.* 2001, 156, 213-219.
32. Völlenkne, H.; Wittmann, A.; Nowotny, H., Über Diphosphate vom Typ  $Me(IV)P_2O_7$ . *Monatshefte für Chemie* 1963, 94, 956-963.
33. Botto, V. I. L.; Baran, E. J., Kristallographische Daten, IR-Spektrum und thermisches Verhalten von Cer(IV)-Diphosphat. *Z. anorg. allg. Chem.* 1977, 430, 283-288.
34. König, K. H.; Meyn, E., Amorphe und Kristalline Cer(IV)-Phosphate als Ionenaustauscher -1. *J. Inorg. Nucl. Chem.* 1967, 29, 1153-1160.
35. Alberti, G.; Costantino, U.; Zsinka, L., Crystalline Insoluble Acid Salts of Tetravalent Metals - XII. *Inorg. nucl. Chem.* 1972, 34, 3549-3560.
36. Hagman, L. O.; Kierkegaard, P., Note on the Structures of  $M^{IV}P_2O_7$  ( $M^{IV} = Ge, Zr, \text{ and } U$ ). *Acta Chem. Scand.* 1969, 23, 327-328.
37. Cabeza, A.; Aranda, M.; Cantero, F.; Lozano, D.; Martínez-Lara, M.; Bruque, S., Synthesis, Structure, and Characterization of Uranium(IV) Phenyl Phosphonate,  $U(O_3PC_6H_5)_2$ , and Uranium(IV) Pyro Phosphate,  $UP_2O_7$ . *Journal of Solid State Chemistry* 1996, 121, 181-189.
38. Sanz, J.; Iglesias, J. E.; Soria, J.; Losilla, E. R.; Aranda, M. A. G.; Bruque, S., Structural Disorder in the Cubic  $3 \times 3 \times 3$  Superstructure of  $TiP_2O_7$ . XRD and NMR Study. *Chem. Mater.* 1997, 9, 996-1003.

39. Helluy, X.; Marichal, C.; Sebald, A., Through-Bond Indirect and Through-Space Direct Dipolar Coupling  $^{31}\text{P}$  MAS NMR Constraints for Spectral Assignment in the Cubic  $3 \times 3 \times 3$  Superstructure of  $\text{TiP}_2\text{O}_7$ . *J. Phys. Chem. B* 2000, 104, 2836-2845.
40. Norberg, S. T.; Svensson, G.; Albertsson, J., A  $\text{TiP}_2\text{O}_7$  superstructure. *Acta Cryst. Section C* 2001, 57, 225-227.
41. Banks, E.; Sacks, R.,  $\text{ReP}_2\text{O}_7$ : A New Isomorph of  $\text{ZrP}_2\text{O}_7$ . *Mat. Res. Bull.* 1982, 17, 1053-1055.
42. Turquat, C.; Muller, C.; Nigrelli, E.; Leroux, C.; Soubeyroux, J.-L.; Nihoul, G., Structural investigation of temperature-induced phase transitions in  $\text{HfV}_2\text{O}_7$ . *The European Physical Journal Applied Physics* 2000, 10, 15-27.
43. Evans, J. S. O.; Hanson, J. C.; Sleight, A. W., Room-Temperature Superstructure of  $\text{ZrV}_2\text{O}_7$ . *Acta Cryst.* 1998, B54, 705-713.
44. Withers, R. L.; Evans, J. S. O.; Hanson, J.; Sleight, A. W., An *in Situ* Temperature-Dependent Electron and X-ray Diffraction Study of Structural Phase Transitions in  $\text{ZrV}_2\text{O}_7$ . *J. Solid State Chem.* 1998, 137, 161-167.
45. Khosrovani, N.; Korthuis, V.; Sleight, A. W.; Vogt, T., Unusual  $180^\circ$  P-O-P Bond Angles in  $\text{ZrP}_2\text{O}_7$ . *Inorg. Chem.* 1996, 35, 485-489.
46. King, I. J.; Fayon, F.; Massiot, D.; Harris, R. K.; Evans, J. S. O., A space group assignment of  $\text{ZrP}_2\text{O}_7$  obtained by  $^{31}\text{P}$  solid state NMR. *Chem. Commun.* 2001, 1766-1767.
47. Gover, R. K. B.; Withers, N. D.; Allen, S.; Withers, R. L.; Evans, J. S. O., Structure and Phase Transitions of  $\text{SnP}_2\text{O}_7$ . *Journal of Solid State Chemistry* 2002, 166, 42-48.
48. Fayon, F.; King, I. J.; Harris, R. K.; Gover, R. K. B.; Evans, J. S. O.; D., M., Characterization of the room-temperature structure of  $\text{SnP}_2\text{O}_7$  by  $^{31}\text{P}$  through space and through bond NMR correlation spectroscopy. *Chem. Mater.* 2003, 15, 2234-2239.
49. Tillmans, E.; Gebert, W.; Baur, W. H., Computer Simulations of Crystal Structures Applied to the Solution of the Superstructure of Cubic Silicodiphosphate. *J. Solid State Chem.* 1973, 7, 69-84.
50. Hartmann, P.; Jana, C.; Vogel, J.; Jager, C.,  $^{31}\text{P}$  MAS and 2D exchange NMR of crystalline silicon phosphates. *Chemical Physical Letters* 1996, 258, 107-112.
51. Burdese, A.; Lucco Borlera, M., Sul sistema tra i pirofosfati di uranio e torio. *Ann. Chim. (Rome)* 1963, 53, 333-343.

52. Laud, K.; Hummel, F. A., The system  $\text{ThO}_2\text{-P}_2\text{O}_5$ . *J. Am. Ceram. Soc.* 1971, 54, 296-298.
53. Roulhac, P. L.; Palenik, G. J., Bond Valence Sum in Coordination Chemistry. The Calculation of the Oxidation State of Cerium in Complexes Containing Cerium Bonded Only to Oxygen. *Inorg. Chem.* 2003, 42, (1), 118-121.
54. Ni, Y.; Hughes, J., Crystal chemistry of the monazite and xenotime structures. *American Mineralogist* 1995, 80, 21-26.
55. Krogh Andersen, A. M.; Norby, P., *Ab initio* structure determination and Rietveld refinement of a high-temperature phase of zirconium hydrogen phosphate and a new polymorph of zirconium pyrophosphate from *in situ* temperature-resolved powder diffraction data. *Acta Crystallogr., Section B* 2000, B56, 618-625.
56. Varga, T.; Wilkinson, A. P., *In situ* high-pressure synchrotron x-ray diffraction study of  $\text{Sc}_2\text{W}_3\text{O}_{12}$  at up to 10 GPa. *Physical Review B* 2005, 71, 214106-1 - 214106-8.
57. Hemamala, U. L. C.; El-Ghoussein., F.; Goedken, A. M.; Chen, B.; Leroux, C.; Kruger, M. B., High-pressure x-ray diffraction and Raman spectroscopy of  $\text{HfV}_2\text{O}_7$ . *Physical Review B* 2004, 70, 214114-1 - 214114-4.
58. Carlson, S.; Krogh Andersen, A. M., High-pressure properties of  $\text{TiP}_2\text{O}_7$ ,  $\text{ZrP}_2\text{O}_7$  and  $\text{ZrV}_2\text{O}_7$ . *J. Appl. Cryst.* 2001, 34, 7-12.
59. Shen, Y.; Kumar, R.; Pravica, M.; Nicol, M., Characteristics of silicone fluid as a pressure transmitting medium in diamond anvil cells. *Review of Scientific Instruments* 2004, 75, (11), 4450-4454.
60. Lundin, U.; Fast, L.; Nordström, L.; Johansson, B., Transition-metal dioxides with a bulk modulus comparable to diamond. *Physical Review B* 1998, 57, (9), 4979 - 4982.
61. Sleight, A. W., Isotropic Negative Thermal Expansion. *Annual Review of Materials Science* 1998, 28, 29-43.
62. Peyronel, G., Esistenza, proprietà e struttura cristallina del  $\text{Pb}^{\text{IV}}\text{P}_2\text{O}_7$ . *Gazz. Chem. Ital.* 1942, 72, 254-262.
63. Frydrych, R.; Lohoff, K., Darstellung und Eigenschaften von Blei(IV)-phosphat-Gelen und kristallinem Blei(IV)-hydrogenphosphat-monohydrat. *Chem. Ber.* 1969, 102, 4070-4079.
64. Bruque, S.; Mag, A.; Losilla, E.R.; Oliverapastor, P.; Mairelestorres, P., Synthesis Optimization and Crystal-Structures of Layered Metal(IV) Hydrogen Phosphates,

$\alpha$ -M (HPO<sub>4</sub>)<sub>2</sub> · H<sub>2</sub>O (M = Ti, Sn, Pb). *Inorganic Chemistry* 1995, 34, (4), 893-899.

## CHAPTER 4

### SYNTHESIS AND CHARACTERIZATION OF SOME $M^{III}M^V P_4 O_{14}$ , STRUCTURAL RELATIVES OF $ZrP_2 O_7$

#### 4.1 Introduction

Cation substitution is one possible method for controlling thermal expansion (Section 1.1.2). The flexible structure of the  $A^{IV}M^V_2O_7$  family can accommodate  $4^+$ -cations with large variations in size, from Si to Th (Section 1.2) and is an ideal candidate for cation substitution. Lattice constants vary in a nearly linear fashion with the radii of  $A^{IV}$ .

Structurally similar to  $ZrP_2O_7$ ,  $M^{III}M^V$ -pyrophosphates ( $M^{III}M^V P_4 O_{14}$ ) are produced by the substitution of  $M^{III}M^V$  cation pairs for  $Zr^{4+}$  in  $ZrP_2O_7$ . Linear trends in lattice constants would be expected in a series of  $M^{III}M^V$ -pyrophosphate compounds based on the size of  $M^{III}$  and  $M^V$  cation pairs ( $M^{III}O_6$  and  $M^VO_6$  octahedra).

Figure 4.1 shows lattice constants versus temperature for  $ZrP_2O_7$ . There is a phase transition at around 290°C. Below 290°C,  $ZrP_2O_7$  exhibits high positive thermal expansion ( $\alpha_{avg} = 13.7 \text{ ppm K}^{-1}$ ; 25 - 293°C) and long-range order associated with a superlattice structure (see Section 1.2). In this structure, P – O – P bonds are bent away from 180° in an ordered fashion, and represent a more thermodynamically stable structure at low temperatures as P – O – P bonds avoid unfavorable 180° angles. Above 290°C,  $ZrP_2O_7$  transitions to a simple cubic structure with some disordered oxygen positions. Associated P – O – P bond angles are constrained by symmetry to have unfavorable P – O – P bonds that average 180° (less thermodynamically stable). The structure shows intermediate thermal expansion ( $\alpha_{avg} = 5.5 \text{ ppm K}^{-1}$ ; 293 - 463°C).

The presence of superstructures in some  $A^{IV}M^V_2O_7$  compounds (Section 1.2.1) does not necessarily lead to an observable temperature-induced order/disorder phase transition. Though  $UP_2O_7$  and  $ZrV_2O_7$  have been reported to go from cubic superlattices to simple cubic structures around  $150^\circ\text{C}$  and  $100^\circ\text{C}$ , respectively,  $TiP_2O_7$  has a superlattice structure at room temperature and does not exhibit a phase transition in the temperature range from  $25 - 1200^\circ\text{C}$  (Section 3.5.2.1 and Figure 3.22).<sup>2-4</sup>  $\gamma\text{-GeP}_2\text{O}_7$ , a monoclinic superlattice (Section 3.5.2.1), does not exhibit a phase transition when heated from room temperature to  $1000\text{K}$ .<sup>5</sup>  $\text{SnP}_2\text{O}_7$ , on the other hand, possesses a quasi-cubic orthorhombic or monoclinic superstructure at room temperature and undergoes two phase transitions upon heating, to triclinic and rhombohedral subcell structures at  $560\text{K}$  and  $830\text{K}$ , respectively.<sup>6</sup>

Based on the varied structures and thermal behaviors of  $A^{IV}M^V_2O_7$  compounds, possible long-range and short-range ordering and the presence or absence of temperature-induced phase transitions are all considered possible for  $M^{III}M^V$ -pyrophosphates. The effect of  $M^{III}$  and  $M^V$  substitution for  $Zr^{4+}$  in  $ZrP_2O_7$ , including order/disorder among  $M^{III}O_6$  and  $M^VO_6$  octahedra, as well as ordering of  $P_2O_7^{4-}$  units, needs to be considered.

Verbaere, et al. reported the first synthesis of single crystal, mixed valence antimony phosphates that were closely related to cubic  $ZrP_2O_7$ .<sup>7</sup>  $\alpha$ - and  $\beta$ - $\text{Sb}^{III}\text{Sb}^V\text{P}_4\text{O}_{14}$  were synthesized in solid state reactions using  $\text{Sb}_2\text{O}_5 \cdot n\text{H}_2\text{O}$  and excess  $\text{NH}_4\text{H}_2\text{PO}_4$ .  $\alpha$ - $\text{Sb}^{III}\text{Sb}^V\text{P}_4\text{O}_{14}$  was crystallized after heating at  $923\text{K}$  and was found to have a monoclinic space group of  $P2_1/c$ . The  $\beta$ -form crystallized at  $773\text{K}$  and belongs to the space group  $\text{Pna}2_1$ . In the Verbaere et al. study, distortion of the  $\text{Sb}^{III}O_6$  octahedra in both the  $\alpha$ - and  $\beta$ -types was reported, a result of the lone pair of electrons in the  $5s^2$

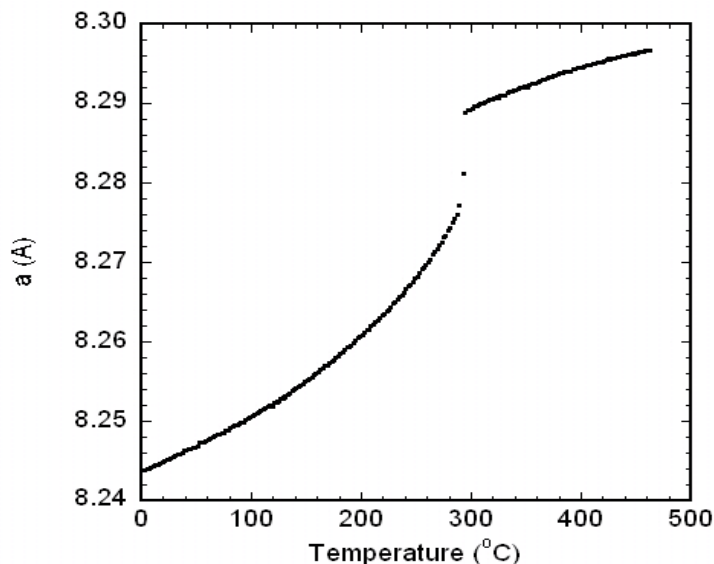


Figure 4.1: Plot of refined lattice constant versus temperature from data supplied by J. S. O. Evans for  $\text{ZrP}_2\text{O}_7$  showing the long-range to short range order phase transition around  $290^\circ\text{C}$ .

orbital of  $\text{Sb}^{3+}$ .  $\text{Sb}^{\text{V}}\text{O}_6$  octahedra, on the other hand, showed expected  $\text{Sb}^{\text{V}} - \text{O}$  bond distances. Verbaere, et al. reported each  $\text{SbO}_6$  octahedron (either  $\text{Sb}^{\text{III}}\text{O}_6$  or  $\text{Sb}^{\text{V}}\text{O}_6$ ) was in a corner-sharing arrangement with  $\text{P}_2\text{O}_7^{4-}$  groups (Section 1.2). The different symmetries for  $\alpha$ - and  $\beta$ - $\text{Sb}^{\text{III}}\text{Sb}^{\text{V}}\text{P}_4\text{O}_{14}$  are due to the different linkages in neighboring octahedra. In  $\beta$ - $\text{Sb}^{\text{III}}\text{Sb}^{\text{V}}\text{P}_4\text{O}_{14}$ , like in  $\text{ZrP}_2\text{O}_7$ , each octahedron is connected in the same way to twelve surrounding octahedra. In  $\alpha$ - $\text{Sb}^{\text{III}}\text{Sb}^{\text{V}}\text{P}_4\text{O}_{14}$ , there are three different types of linkages from one octahedron to twelve surrounding octahedra, resulting in lower symmetry.

Oyetola, et al., in a 1991 work, reported the synthesis of several additional  $\text{M}^{\text{III}}\text{M}'^{\text{V}}$ -pyrophosphates ( $\text{M}^{\text{III}} = \text{Sb, Bi, Nd, Eu}$ ;  $\text{M}^{\text{V}} = \text{Sb}$ , and  $\text{M}'^{\text{V}} = \text{Nb, Ta}$ ). Syntheses were accomplished like those in Verbaere's 1988 work. The structure of  $\text{BiSbP}_4\text{O}_{14}$  was reported as orthorhombic, while  $\text{BiTaP}_4\text{O}_{14}$  was reported in two forms: monoclinic and cubic. Other compounds ( $\text{SbTaP}_4\text{O}_{14}$ ,  $\text{BiNbP}_4\text{O}_{14}$ ,  $\text{NdTaP}_4\text{O}_{14}$ ,  $\text{EuNbP}_4\text{O}_{14}$ , and

EuTaP<sub>4</sub>O<sub>14</sub>) were found to have cubic structures like that of high temperature ZrP<sub>2</sub>O<sub>7</sub> or a quasi-cubic structure (EuNbP<sub>4</sub>O<sub>14</sub>). Thus, distortion of M<sup>III</sup>O<sub>6</sub> octahedra was observed resulting in lower symmetry for some compounds and long-range ordering was not reported. However, no thermal characterization was performed by Verbaere, et al. or Oyetola, et al.<sup>8</sup>

Using a different approach to the syntheses of M<sup>III</sup>M<sup>V</sup>-pyrophosphates, Varga, et al. prepared relatively pure microcrystalline compounds (M<sup>III</sup> = Al, Fe, Ga, In, Y, Nd, and Bi; M<sup>V</sup> = Nb, Ta) and performed thermal expansion studies on some of them.<sup>1</sup> The synthesis method consisted of a hydrolytic sol-gel process (Sections 3.1.2 and 4.2.1) with rapid quenching after firing. Varga et al. found no evidence for order-disorder phase transitions for the compounds in thermal studies carried out in the temperature range ~25 – 600°C; however, the authors suggested possible long-range ordering for InNbP<sub>4</sub>O<sub>14</sub> and AlTaP<sub>4</sub>O<sub>14</sub> structures based on a comparable lattice constant for AlTaP<sub>4</sub>O<sub>14</sub> to that of TiP<sub>2</sub>O<sub>7</sub> and similar CTEs for both compounds to that of the low temperature form of ZrP<sub>2</sub>O<sub>7</sub>. The lattice constant and CTE for YNbP<sub>4</sub>O<sub>14</sub> were found to be similar to that of the high temperature form of ZrP<sub>2</sub>O<sub>7</sub>.

In this chapter, the preparation of additional M<sup>III</sup>M<sup>V</sup>P<sub>4</sub>O<sub>14</sub> compounds and thermal expansion studies are presented. Powder XRD provides evidence for possible supercell reflections in some M<sup>III</sup>M<sup>V</sup>P<sub>4</sub>O<sub>14</sub> compounds, and TEM/ED supports the observation of superlattice reflections from the powder XRD data for one of the compounds. With data from seventeen M<sup>III</sup>M<sup>V</sup>-pyrophosphate samples, trends in lattice constants and CTEs versus average ionic radii are discussed.

## 4.2 Synthesis and Thermal Properties of Some $M^{III}M^V P_4 O_{14}$ Compounds (*KMW255*, *KMW256*, *KMW257*, *KMW262*, *KMW263*, *KMW287*, and *KMW296*)

### 4.2.1 Experimental

A hydrolytic sol-gel method from Varga, et al.<sup>1</sup> was used to prepare ( $M^{III} = Al, Ga, Sc, (Y_{1-x}In_x), Yb, Er, Dy, Gd; M^V = Nb$ ).  $BiTaP_4O_{14}$  was synthesized using the method of Verbaere, et al. (Section 4.1).<sup>7</sup> A typical synthesis consisted of mixing Nb-isopropoxide in an ethanol/acac (2,4-pentanedione) solution (stored and weighed in an argon atmosphere) into a metal salt/ethanol solution. An aqueous solution of  $NH_4H_2PO_4$  (or in some cases,  $(NH_4)_2HPO_4$ ) was then transferred slowly to the mixture while stirring. The resulting thick mixture was stirred for approximately 30 minutes and then dried overnight in a 100°C oven. The molar ratios of  $M^{III}:M^V:P$  were 1:1:4. Organics were driven off by heating the sample for 4 hours at 350°C. Crystallization temperatures varied between 700 - 1000°C, depending on the  $M^{III}M^V$  cation constituents, and the duration of firing varied between 1.5 to 24 hours. The crystallized products were quenched to room temperature rapidly.

Lab powder XRD, using a Scintag X1 diffractometer, was used to identify the compounds. The PDF database in JADE<sup>9</sup> (Section 2.51) was used to match powder patterns to related structures and to identify impurities.

Thermal expansion data were obtained with a Panalytical X'Pert Pro diffractometer, an Anton Paar XKD 900 furnace, and an X'Celerator detector (Section 2.1.1) at Oak Ridge National Labs, Oak Ridge, TN with the help of Dr. Andrew Payzant.

The temperature range for the thermal expansion studies was 25 - 900°C. XRD data were analyzed using the Rietveld method within GSAS<sup>10</sup> (Section 2.5.2). The model used was that of cubic ZrP<sub>2</sub>O<sub>7</sub> in space group P a  $\bar{3}$ . Several samples produced and characterized by others in the group are presented in this chapter for completeness.

TEM/ED (Section 2.2) was performed on samples at the High Temperature Materials Laboratory, Oak Ridge National Labs, Oak Ridge, TN, with the help of Dr. Jane Howe. Section 2.2 provides a description of the experiment.

#### **4.2.2 Results and Discussion**

Lattice constants versus temperature curves for M<sup>III</sup>M<sup>V</sup>-pyrophosphates, Figures 4.2 (a) and (b), show that none of the samples exhibited the abrupt long-range/short-range order phase transition as observed for ZrP<sub>2</sub>O<sub>7</sub> (Figure 4.1) in the temperature range explored. In both (a) and (b) of Figure 4.2, the expansion behavior of most compounds is close to linear below 600°C. However, above 600°C most compounds showed a decrease in CTE. In (a), an exception to this behavior was observed for GaNbP<sub>4</sub>O<sub>14</sub>, which exhibited an increasing CTE at high temperatures.

AlNbP<sub>4</sub>O<sub>14</sub> exhibited what appeared to be a possible phase transition shown in Figure 4.2 (a); its thermal expansion curve indicated a slight shift to larger lattice constant values at around 700°C. The data for InNbP<sub>4</sub>O<sub>14</sub>, shown in Figure 4.2 (b), suggested a similar phase transition at ~600°C. The lattice constant versus temperature for BiTaP<sub>4</sub>O<sub>14</sub>, Figure 4.2 (b), also suggest a phase transition at approximately 300°C and possibly around 750°C as well.

These observations are shown in Figures 4.3 (a), (b), and (c). In calculating CTEs

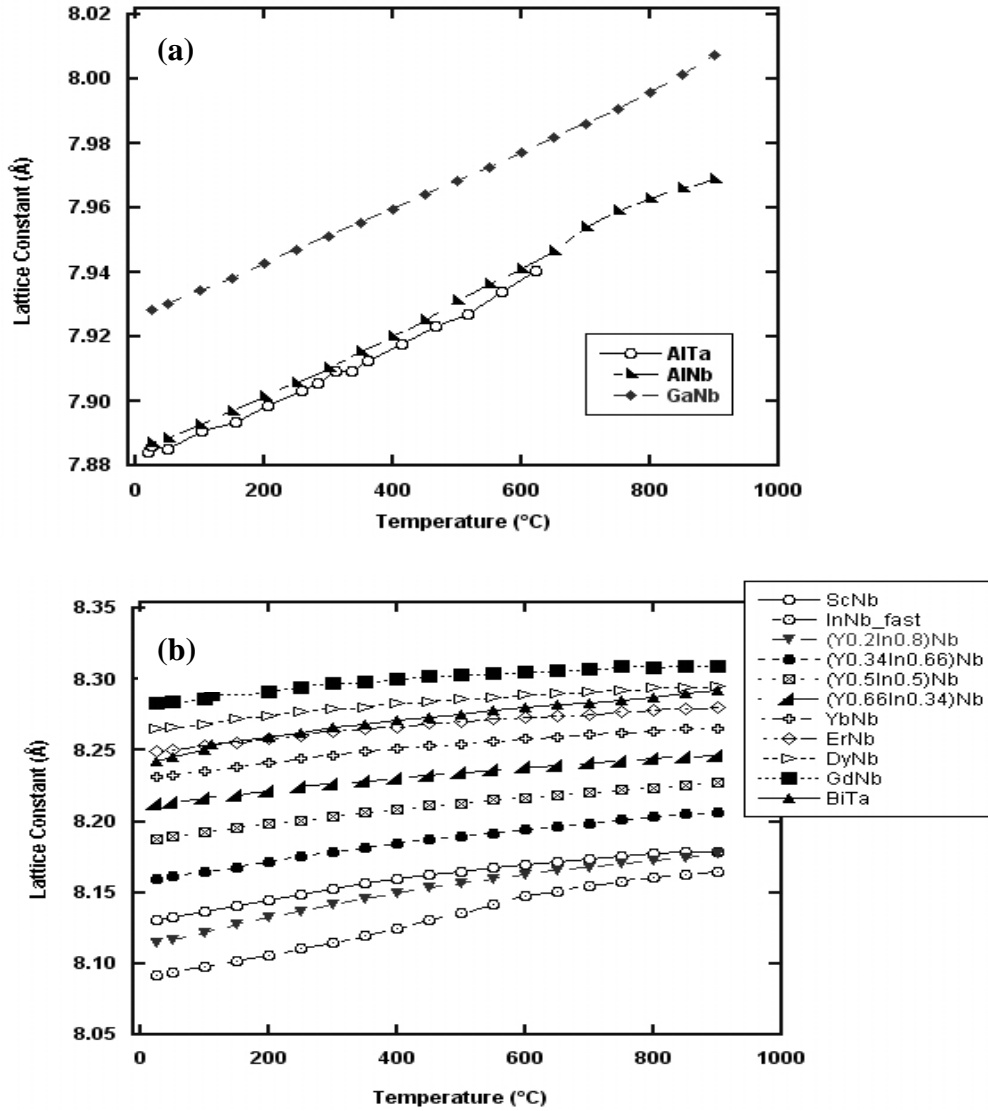


Figure 4.2: (a) Compiled plots of refined lattice constants versus temperature for  $\text{AlTaP}_4\text{O}_{14}$ ,  $\text{AlNbP}_4\text{O}_{14}$ , and  $\text{GaNbP}_4\text{O}_{14}$ . Data for  $\text{AlTaP}_4\text{O}_{14}$  obtained from Varga et al.<sup>1</sup> (b) Compiled plots for the remaining  $\text{M}^{\text{III}}\text{M}^{\text{IV}}$ -pyrophosphate compounds.

in the temperature ranges before and after the change in lattice constants, it was found that the CTEs for  $\text{AlNbP}_4\text{O}_{14}$  were  $13.5 \text{ ppm K}^{-1}$  (300 - 700°C) and  $9.38 \text{ ppm K}^{-1}$  (700 - 900°C). While  $\text{InNbP}_4\text{O}_{14}$  had a CTE of  $13.4 \text{ ppm K}^{-1}$  (300 - 600°C), its CTE was  $7.2$

ppm K<sup>-1</sup> (600 - 900°C). CTEs for BiTaP<sub>4</sub>O<sub>14</sub> were estimated at 10.4 ppm K<sup>-1</sup> (25 - 300°C), 5.7 ppm K<sup>-1</sup> (300 - 600°C), and 5.3 ppm K<sup>-1</sup> (750 - 900°C).

The changes in lattice constants observed for InNbP<sub>4</sub>O<sub>14</sub>, AlNbP<sub>4</sub>O<sub>14</sub>, and BaTiP<sub>4</sub>O<sub>14</sub>, Figures 4.3 (a), (b), and (c), along with some significant changes in CTE values, suggest long-range ordering of the structures at lower temperatures. Examination

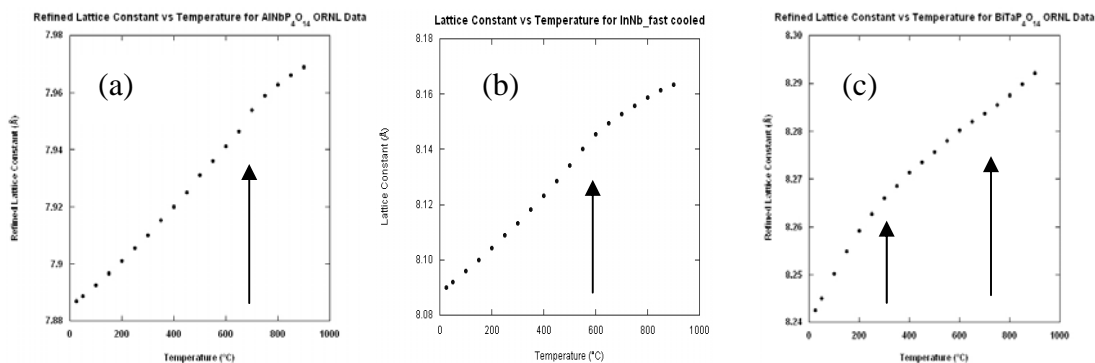


Figure 4.3: Plots of lattice constant versus temperature for (a) AlNbP<sub>4</sub>O<sub>14</sub>, (b) InNbP<sub>4</sub>O<sub>14</sub>, and (c) BiTaP<sub>4</sub>O<sub>14</sub> showing possible phase transitions. Error bars are not included for clarity.

of powder XRD scans for all compounds at all temperatures did not reveal any major changes structures. Further exploration at higher temperatures than those used in this study for AlNbP<sub>4</sub>O<sub>14</sub>, GaNbP<sub>4</sub>O<sub>14</sub> (which showed increasing CTEs with increasing temperature), InNbP<sub>4</sub>O<sub>14</sub>, and BiTaP<sub>4</sub>O<sub>14</sub> would help clarify what, if anything, is happening to the structures.

Though difficult to observe in powder XRD patterns due to low intensity, the data were examined for evidence of superlattice reflections in the patterns for AlNbP<sub>4</sub>O<sub>14</sub>, InNbP<sub>4</sub>O<sub>14</sub>, BiTaP<sub>4</sub>O<sub>14</sub>, as well as for all other compounds prepared in this work. Some

powder patterns showed possible evidence for superlattice reflections, while others indicated structures that were closely related to high temperature cubic  $ZrP_2O_7$ . The room temperature powder pattern of  $AlNbP_4O_{14}$ , for example, matched reflections of cubic

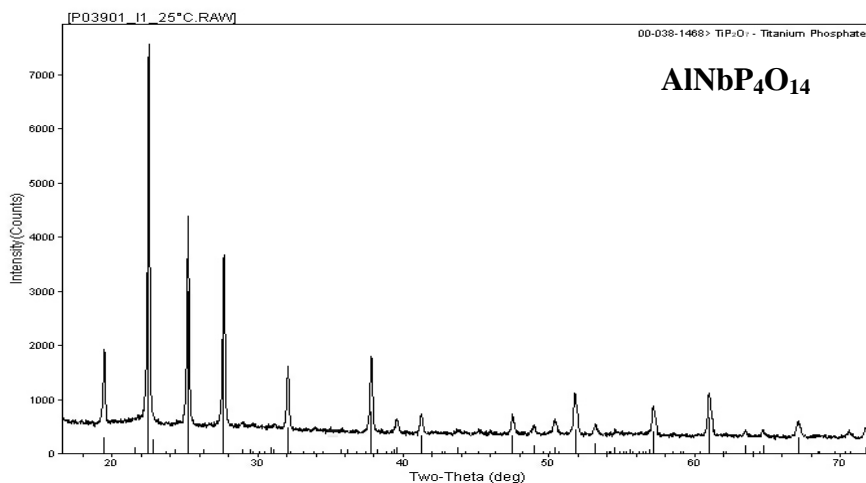


Figure 4.4: Zoom image of powder pattern obtained from ORNL data for  $AlNbP_4O_{14}$ . Peaks match those for PDF # 00-038-1468, cubic superlattice,  $TiP_2O_7$ . Vertical reflections for  $TiP_2O_7$  are shown through peaks of pattern.

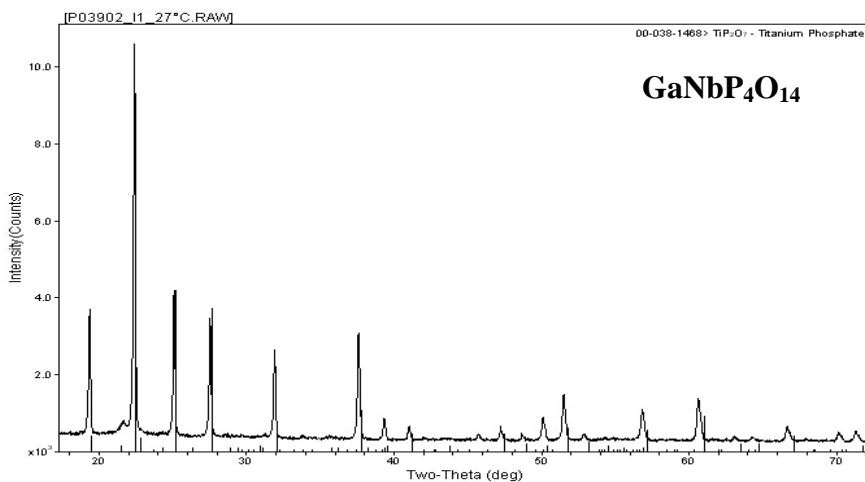


Figure 4.5: Zoom image of powder pattern obtained from ORNL data for  $GaNbP_4O_{14}$ . Peaks match those for PDF # 00-038-1468, cubic superlattice,  $TiP_2O_7$ . Vertical reflections for  $TiP_2O_7$  are shown through peaks of pattern.

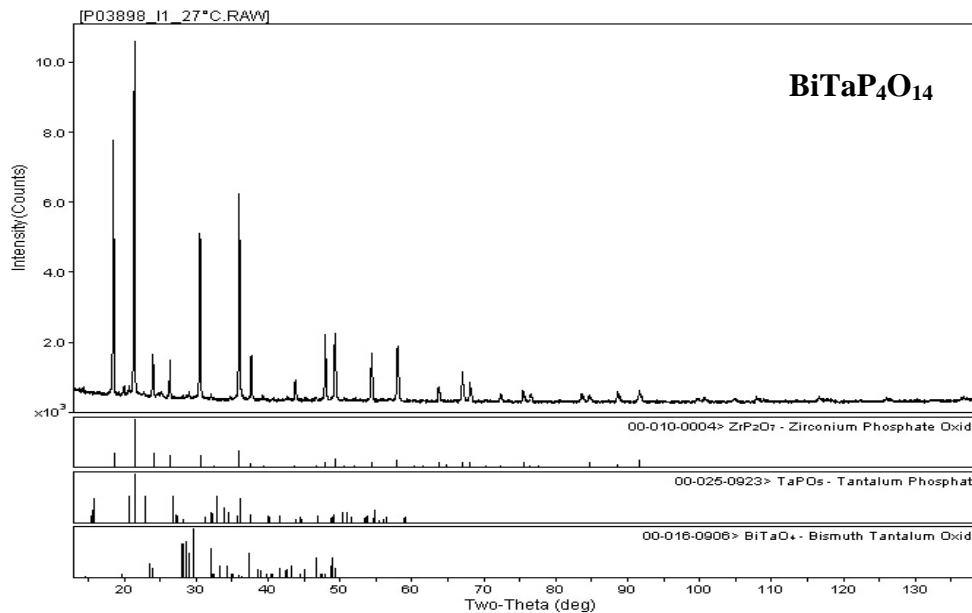


Figure 4.6: Zoom image of powder pattern obtained from ORNL data for BiTaP<sub>4</sub>O<sub>14</sub>. Below the powder pattern are reflections from the PDF that show peaks in the pattern match those for PDF # 00-010-0004, cubic ZrP<sub>2</sub>O<sub>7</sub>, and two impurity phases: PDF # 00-025-0923, TaPO<sub>4</sub> and PDF # 00-016-0906, BiTaPO<sub>4</sub>.

TiP<sub>2</sub>O<sub>7</sub> supercell ( $a = 24.742 \text{ \AA}$ , PDF # 00-038-1468), Figure 4.4. Peaks in the room temperature powder pattern for GaNbP<sub>4</sub>O<sub>14</sub> were noted to have the same general pattern as the TiP<sub>2</sub>O<sub>7</sub> supercell, Figure 4.5.

Peaks in the room temperature powder pattern for BiTaP<sub>4</sub>O<sub>14</sub>, Figure 4.6, appeared very similar to those of simple cubic ZrP<sub>2</sub>O<sub>7</sub> (PDF # 00-010-0004). However, BiTaP<sub>4</sub>O<sub>14</sub> also contained slight impurity phases identified as TaPO<sub>4</sub> (PDF # 00-025-0923) and BiTaO<sub>4</sub> (PDF # 00-016-0906).

Figures 4.7 and 4.8 show powder patterns for ScNbP<sub>4</sub>O<sub>14</sub> and InNbP<sub>4</sub>O<sub>14</sub> and each pattern displays a very close match to simple cubic ZrP<sub>2</sub>O<sub>7</sub> (PDF # 00-010-0004) and the

same unidentified peak at approximately 46.0 two-theta ( $^{\circ}$ ). The pattern for  $\text{InNbP}_4\text{O}_{14}$  showed an additional unidentified peak at approximately 86.0 two-theta ( $^{\circ}$ ).

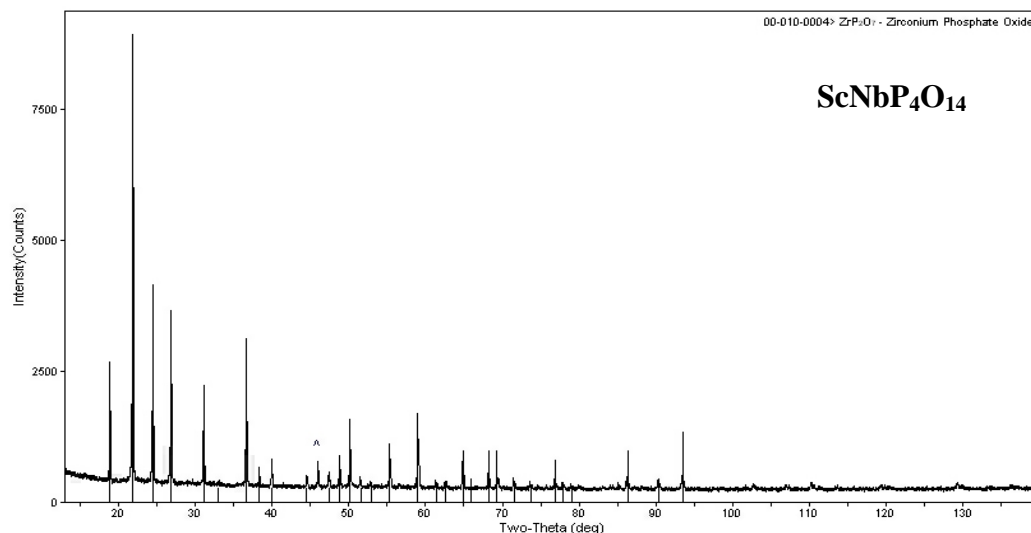


Figure 4.7: Powder pattern obtained from Scintag data for  $\text{ScNbP}_4\text{O}_{14}$ . Vertical lines through the peaks represent reflections for cubic  $\text{ZrP}_2\text{O}_7$  (PDF # 00-010-0004). One peak, indicated by ^, could be from an unidentified impurity.

In contrast to powder pattern evidence suggesting superlattice structures for  $\text{GaNbP}_4\text{O}_{14}$  and  $\text{AlNbP}_4\text{O}_{14}$ , powder XRD patterns for rare earth  $\text{M}^{\text{III}}\text{M}'^{\text{V}}$ -pyrophosphates suggested structures closely related to simple cubic  $\text{ZrP}_2\text{O}_7$  along with some impurity phases. Figure 4.9 shows the room temperature powder XRD pattern for  $\text{YbNbP}_4\text{O}_{14}$ ; its peaks nearly matching those for cubic  $\text{ZrP}_2\text{O}_7$  (PDF # 00-010-0004).  $\text{YbNbP}_4\text{O}_{14}$  was found to contain an impurity phase,  $\text{YbP}_3\text{O}_9$  (PDF # 00-045-0653), denoted by a star (\*). An unidentified peak at  $\sim 85.0$  two-theta ( $^{\circ}$ ) is indicated by the character, ^, in Figure 4.9.

Room temperature powder XRD patterns for  $\text{ErNbP}_4\text{O}_{14}$ ,  $\text{DyNbP}_4\text{O}_{14}$ , and

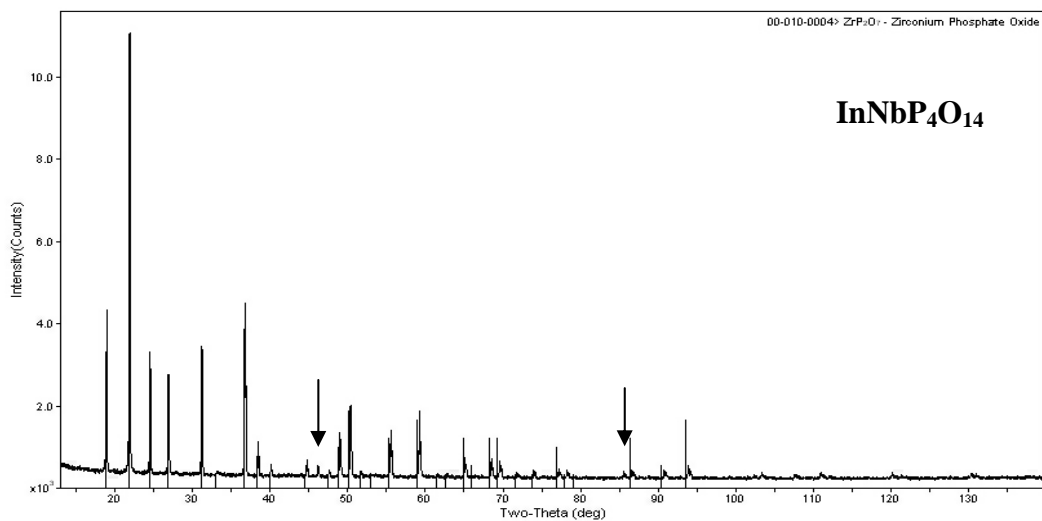


Figure 4.8: Powder pattern obtained from Scintag data for  $\text{InNbP}_4\text{O}_{14}$ . Vertical lines through the peaks represent reflections for cubic  $\text{ZrP}_2\text{O}_7$  (PDF # 00-010-0004). Two peaks, indicated by arrows, could belong to an unidentified impurity phase.

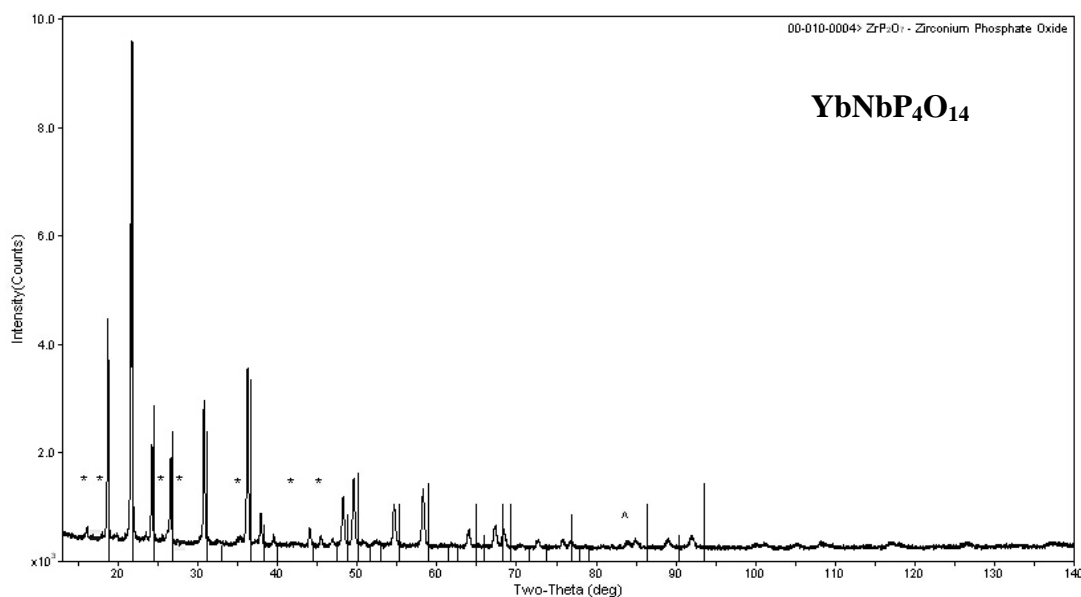


Figure 4.9: Powder pattern from ORNL data for  $\text{YbNbP}_4\text{O}_{14}$ . Peaks match those for PDF # 00-010-0004, cubic  $\text{ZrP}_2\text{O}_7$ . Vertical lines from the baseline of the patterns through the peaks for  $\text{YbNbP}_4\text{O}_{14}$  are the reflections for  $\text{ZrP}_2\text{O}_7$ . One impurity phase was identified  $\text{YbP}_3\text{O}_9$ ; its peaks denoted by \*. An unidentified peak at 84.5 two-theta ( $^\circ$ ) is indicated by ^.

GdNbP<sub>4</sub>O<sub>14</sub> matched reflections for cubic ZrP<sub>2</sub>O<sub>7</sub> (PDF # 00-010-0004) and all had slight impurities (not shown). ErNbP<sub>4</sub>O<sub>14</sub> contained two impurity phases, ErPO<sub>4</sub> (PDF # 00-009-0383) and Er(PO<sub>3</sub>)<sub>3</sub> (PDF # 00-055-0209). DyNbP<sub>4</sub>O<sub>14</sub> also was observed to contain two impurity phases, Dy(PO<sub>3</sub>)<sub>3</sub> (PDF # 00-052-1760) and DyNbO<sub>4</sub> (PDF # 00-022-1094). GdNbP<sub>4</sub>O<sub>14</sub> was found to contain one impurity phase, Gd(PO<sub>3</sub>)<sub>3</sub> (PDF # 00-052-1761).

As mentioned previously, superlattice reflections in powder XRD patterns are often weak and could be confused with peaks from a slight impurity phase(s). The match of an experimental powder XRD pattern to a particular A<sup>IV</sup>M<sup>V</sup><sub>2</sub>O<sub>7</sub> superlattice or to a simple cubic structure, therefore, was not considered absolute confirmation of the presence or absence of superlattice structures in some M<sup>III</sup>M<sup>V</sup>-pyrophosphates especially when impurities were also present. In addition, the possibility that some M<sup>III</sup>M<sup>V</sup>-pyrophosphates had symmetries lower than cubic was also considered; however, further analyses using, for example, high resolution synchrotron powder XRD, would be necessary to establish a lower symmetry.

Table 4.1 is a summary of weighted average ionic radii, refined room temperature lattice constants, and calculated average linear CTEs in three temperature ranges.

Average ionic radii were obtained from the work of Shannon.<sup>11</sup> Compounds from the work of Varga, et al.<sup>1</sup> are included in the summary (AlTaP<sub>4</sub>O<sub>14</sub>, GaTaP<sub>4</sub>O<sub>14</sub>, FeTaP<sub>4</sub>O<sub>14</sub>, YNbP<sub>4</sub>O<sub>14</sub>, and NdTaP<sub>4</sub>O<sub>14</sub>). Numbers in parentheses are standard deviations from refinements of room temperature lattice constants. Values listed in Table 4.1 were used for determining trends in the data; however, some interesting information was observed from the calculated CTEs for the compounds. AlTaP<sub>4</sub>O<sub>14</sub>, AlNbP<sub>4</sub>O<sub>14</sub>, and InNbP<sub>4</sub>O<sub>14</sub>, with relatively small average ionic radii, were noted to have CTEs that are very similar to

that for the LT form of  $\text{ZrP}_2\text{O}_7$  ( $\alpha_{\text{avg}} = 13.7 \text{ ppm K}^{-1}$ ; 25 - 293°C) in the temperature range from 300°C to 600°C: 12.8 ppm K<sup>-1</sup>, 13.1 ppm K<sup>-1</sup>, and 13.4 ppm K<sup>-1</sup>, respectively. This was reported by Varga, et al. for  $\text{AlTaP}_4\text{O}_{14}$  and  $\text{InNbP}_4\text{O}_{14}$ .

Table 4.1 also shows that the solid solution series,  $(\text{Y}_{1-x}\text{In}_x)\text{NbP}_4\text{O}_{14}$ , exhibits a trend toward lower CTE values with increasing Y content across the three temperature ranges. In addition, Table 4.1 reveals most of the larger average ionic radii compounds have moderate to low positive CTEs. Only four  $\text{M}^{\text{III}}\text{M}^{\text{V}}$ -pyrophosphates had CTEs comparable to that of the high temperature form of  $\text{ZrP}_2\text{O}_7$  ( $\alpha_{\text{avg}} = 5.5 \text{ ppm K}^{-1}$ ; 293 – 463°C):  $\text{YNbP}_4\text{O}_{14}$  ( $\alpha_{\text{avg}} = 5.1(0) \text{ ppm K}^{-1}$ ; 25 – 300°C),  $(\text{Y}_{0.34}\text{In}_{0.66})\text{NbP}_4\text{O}_{14}$  ( $\alpha_{\text{avg}} = 5.1(0) \text{ ppm K}^{-1}$ ; 600 – 900°C),  $(\text{Y}_{0.5}\text{In}_{0.5})\text{NbP}_4\text{O}_{14}$  ( $\alpha_{\text{avg}} = 5.41(0) \text{ ppm K}^{-1}$ ; 300 – 600°C),  $\text{BiTaP}_4\text{O}_{14}$  ( $\alpha_{\text{avg}} = 5.7(0) \text{ ppm K}^{-1}$ ; 300 – 600°C). Also observed were lower CTEs for the larger rare earth compounds in the 300 – 600°C and 600 – 900°C temperature ranges.

Figure 4.10 shows refined room temperature lattice constants versus average ionic radii for  $\text{M}^{\text{III}}\text{M}^{\text{V}}$ -pyrophosphates. A linear fit to the data (equation shown at the top of the plot) shows most data points clustering around the fitted line within reasonable limits with the exception of  $\text{ScNbP}_4\text{O}_{14}$  and  $\text{BiTaP}_4\text{O}_{14}$ . Interestingly, the average ionic radius of the ScNb cation (0.8325 Å) is smaller than that calculated for InNb (0.8600 Å) and the solid solution member  $(\text{Y}_{0.2}\text{In}_{0.8})\text{Nb}$  (0.8705 Å), yet  $\text{ScNbP}_4\text{O}_{14}$  has a larger room temperature lattice constant than those for the  $\text{InNbP}_4\text{O}_{14}$  and  $(\text{Y}_{0.2}\text{In}_{0.8})\text{NbP}_4\text{O}_{14}$ . On the other hand, the BiTa has the largest average ionic radius of all the compounds, 0.9750 Å, but  $\text{BiTaP}_4\text{O}_{14}$  exhibited a smaller room temperature lattice constant than several of the rare earth compounds (Table 4.1).

A plot of average linear CTE versus average ionic radius for the temperature

Table 4.1 Summary of Data for  $M^{III}M^V P_4O_{14}$  Compounds

Sample	Average Ionic Radius (Å)	25C RT Lattice Constant (Å)	AlTa (19-310C) AlTa(310-621C)			
			Zr CTE	CTE 25-300	CTE 300-600 CTE 600-900	
AlTa	0.7275	7.8862(10)		<b>10.5(0)</b>	<b>12.8(0)</b>	-
AlNb	0.7275	7.88694(19)		<b>10.7(1)</b>	<b>13.1(0)</b>	<b>11.9(0)</b>
GaNb	0.7700	7.92861(16)		<b>10.4</b>	<b>10.9</b>	<b>12.6</b>
GaTa	0.7700	7.9233(12)		-	-	-
FeTa	0.7825	7.9807(3)		-	-	-
ScNb	0.8325	8.13095(7)		<b>9.8(0)</b>	<b>6.9(5)</b>	<b>3.9(0)</b>
InNb_fast	0.8600	8.09162(7)		<b>10.5(0)</b>	<b>13.4(2)</b>	<b>7.2(2)</b>
InNb_slow	0.8600	8.09256(7)		<b>10.1(0)</b>	<b>13.5(0)</b>	<b>7.3(3)</b>
Zr < 290C	0.8600	8.2416(2)	<b>13.7</b>			
Zr > 290C	0.8600		<b>5.5</b>			
(Y0.2In0.8)Nb	0.8705	8.11526(8)		<b>12.1(0)</b>	<b>8.6(0)</b>	<b>6.0(2)</b>
(Y0.34In0.66)Nb	0.8767	8.15963(9)		<b>8.4(0)</b>	<b>6.5(0)</b>	<b>5.1(0)</b>
(Y0.50In0.50)Nb	0.8850	8.18779(15)		<b>7.0(0)</b>	<b>5.4(1)</b>	<b>4.1(0)</b>
(Y0.66In0.34)Nb	0.8933	8.21284(18)		<b>6.1(0)</b>	<b>4.7(5)</b>	<b>3.5(0)</b>
YbNb	0.8940	8.2316(2)		<b>6.8(0)</b>	<b>4.7(0)</b>	<b>3.1(0)</b>
ErNb	0.9050	8.24909(18)		<b>6.2(3)</b>	<b>4.1(4)</b>	<b>2.9(5)</b>
YNb	0.9100	8.2586(11)		<b>5.1(0)</b>	<b>4.0(3)</b>	-
DyNb	0.9160	8.2658(0)		<b>6.1(5)</b>	<b>3.9(2)</b>	<b>2.7(0)</b>
GdNb	0.9290	8.2830(5)		<b>6.0(0)</b>	<b>3.5(0)</b>	<b>1.6(0)</b>
NdTa	0.9515	8.3047(5)		-	-	-
BiTa	0.9750	8.24259(11)		<b>10.4(0)</b>	<b>5.7(0)</b>	<b>4.7(0)</b>

range 600 – 900°C is shown in Figure 4.11. Data were fit with a straight line. A trend was observed in the data that is nearly linear, but imperfect due to the outlier points for  $GaNbP_4O_{14}$ ,  $ScNbP_4O_{14}$ , and  $BiTaP_4O_{14}$ .  $ScNbP_4O_{14}$  and  $BiTaP_4O_{14}$  showed inconsistent CTEs in this temperature range relative to what might be expected for their cation sizes.  $GaNbP_4O_{14}$  was observed to exhibit increasing CTEs over this temperature range. The anomalous room temperature lattice constant (see Figure 4.10) and CTE (see Figure 4.11) for  $BiTaP_4O_{14}$  were considered to be in part due to the lone pair of electrons in the  $6s^2$  orbital of  $Bi^{3+}$ , which has been reported to result in greater distortion in the  $PO_4$  tetrahedra bonded to  $MO_6$  octahedra and to affect the overall network structure. Such distortion due to a lone pair of electrons has also been reported for  $Sb^{III}Sb^V P_4O_{14}$ .<sup>7</sup>  $ScNbP_4O_{14}$ , on the other hand, exhibited a larger than expected lattice constant and

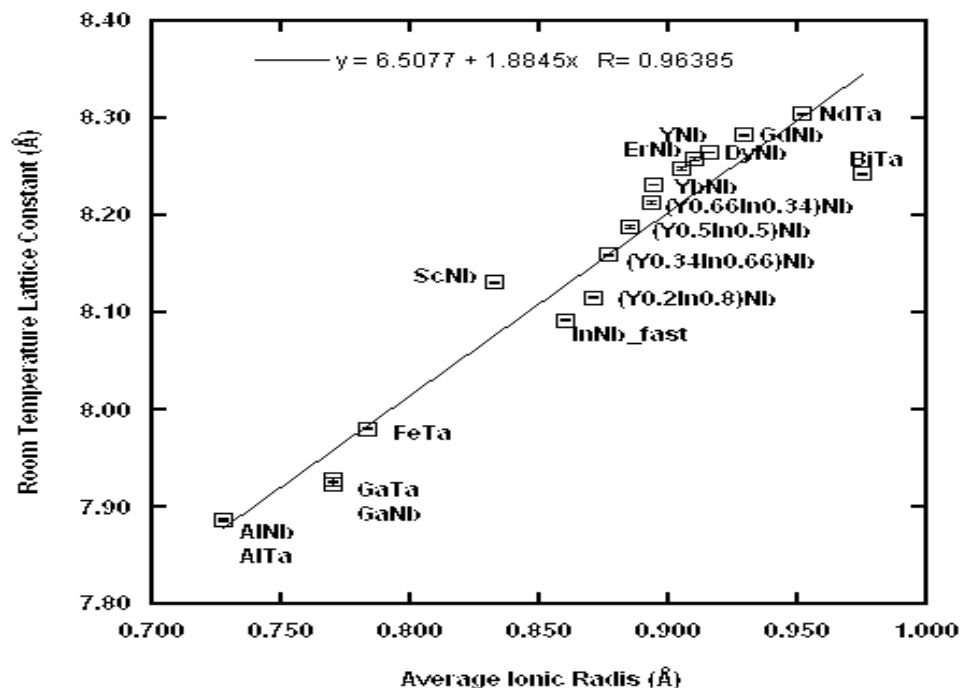


Figure 4.10: Room temperature lattice constants versus average ionic radii for  $M^{III}M'^V$ -pyrophosphate compounds. Most compounds cluster around the linear fit to the data (equation at top of plot). Error bars are included.

lower than expected CTE for its size.

An instantaneous CTE was calculated from a quadratic equation fit to the lattice constant versus temperature curves for the compounds prepared in this research. The quadratic was differentiated and divided by the lattice constant to get the CTE. The combined plot for instantaneous CTE versus temperature in the temperature range from 25 – 900°C is shown in Figure 4.12. It was observed that most instantaneous CTEs versus temperature curves decrease with increasing temperature. Exceptions to this tendency are  $AlTaP_4O_{14}$ ,  $AlNbP_4O_{14}$ , and  $GaNbP_4O_{14}$ , which showed increasing instantaneous CTE with increasing temperature (see Figure 4.13). Data for  $AlTaP_4O_{14}$  was only available from room temperature to 600 °C,<sup>1</sup> but average linear CTEs for  $GaNbP_4O_{14}$  were

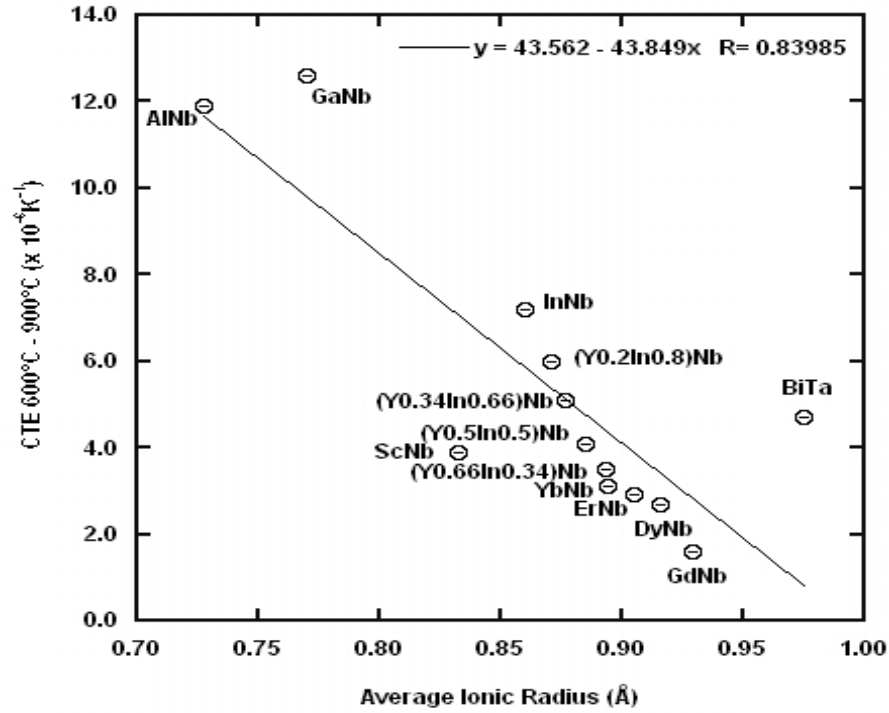


Figure 4.11: Plot of average linear CTE versus average ionic radius for  $M^{III}M^{IV}$ -pyrophosphates in the temperature range 600-900°C. Error bars are included.

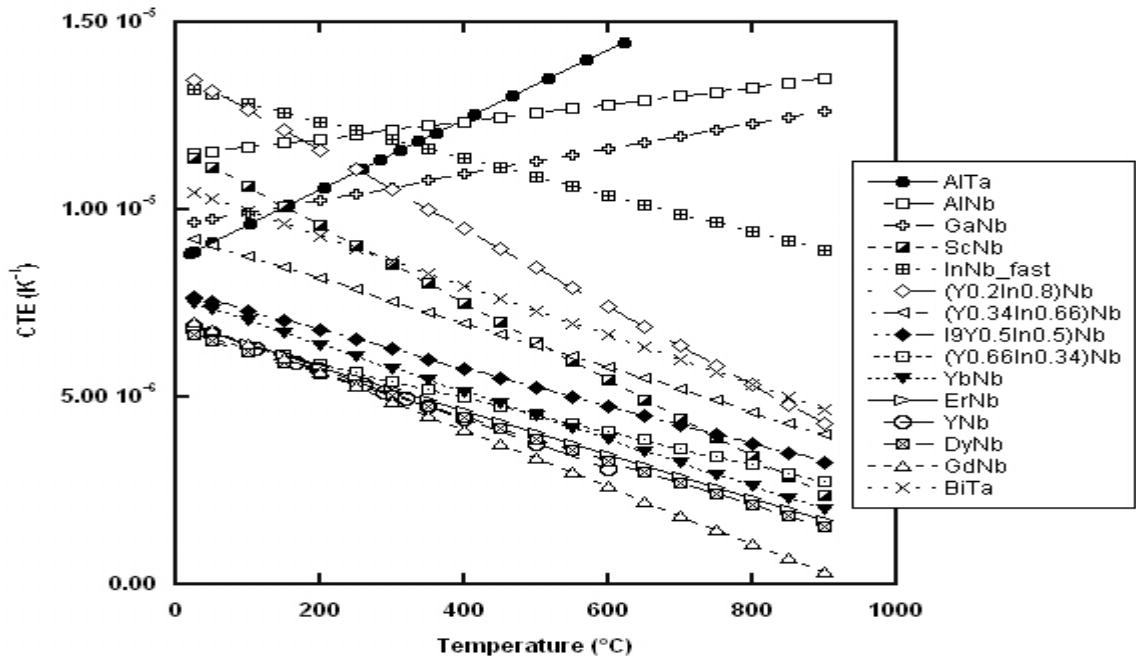


Figure 4.12: Instantaneous CTE versus temperature for  $M^{III}M^{IV}$ -pyrophosphates.

observed to increase on heating at all temperatures between 25 - 900°C, CTEs for  $\text{AlNbP}_4\text{O}_{14}$  increased from room temperature to 600°C and then decreased slightly between 600 – 900°C (see Table 4.1), which explains the small difference in the slopes of the two curves for these compounds in Figure 4.12.

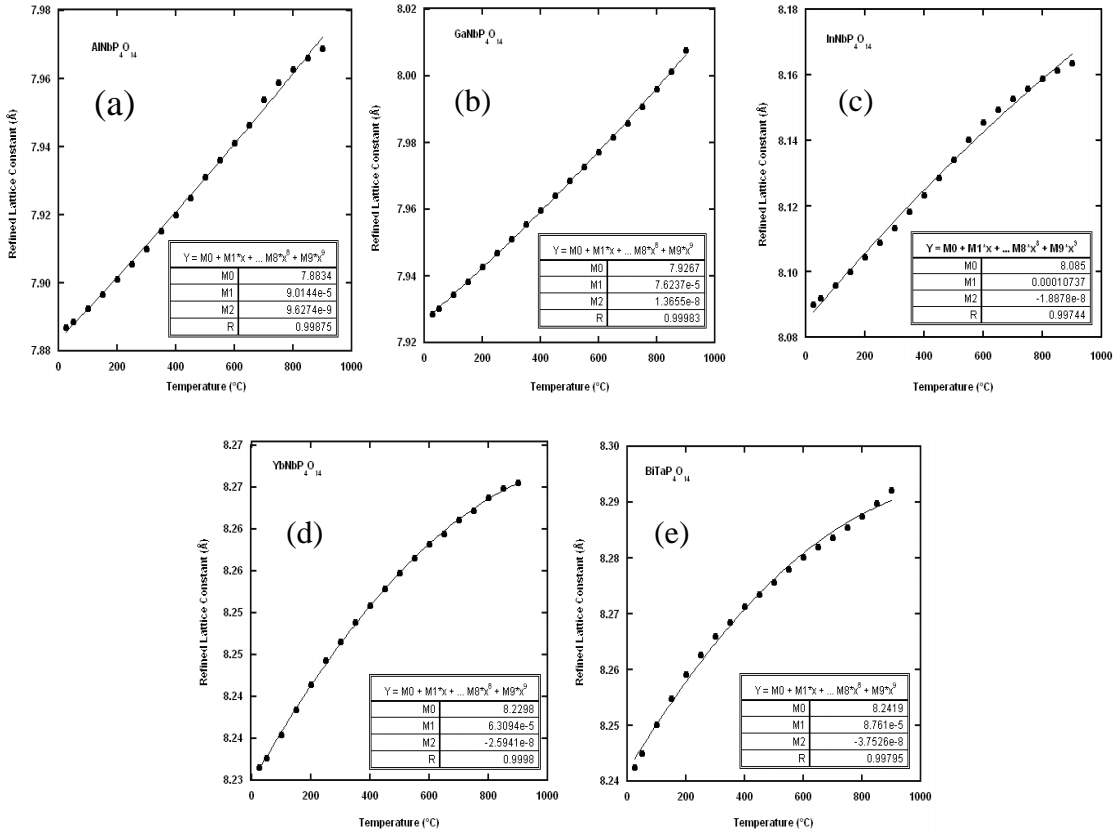


Figure 4.13: (a) – (e) Lattice constant versus temperature plots with quadratic fits to curves. (a)  $\text{AlNbP}_4\text{O}_{14}$ ; (b)  $\text{GaNbP}_4\text{O}_{14}$ ; (c)  $\text{InNbP}_4\text{O}_{14}$ ; (d)  $\text{YbNbP}_4\text{O}_{14}$ ; and (e)  $\text{BiTaP}_4\text{O}_{14}$ . Error bars are not included for clarity.

Some curves shown in Figure 4.12 did not have good quadratic fits to thermal expansion curves. Figures 4.13, (a) – (e), show lattice constants versus temperature plots with quadratic fits for comparison. In Figures 4.13 (a), (c), and (e),  $\text{AlNbP}_4\text{O}_{14}$ ,

InNbP<sub>4</sub>O<sub>14</sub>, and BiTaP<sub>4</sub>O<sub>14</sub>, respectively, display sigmoidal-shaped curves, presumably due to phase transitions (see Figures 4.3 (a) – (c)). In (b) and (d) of Figure 4.13, good quadratic fits were observed to the lattice constant versus temperature plots for GaNbP<sub>4</sub>O<sub>14</sub> and YbNbP<sub>4</sub>O<sub>14</sub>, respectively. This quality of fit was typical for the other compounds studied.

### 4.2.3 Electron Diffraction

TEM/ED was performed on some M<sup>III</sup>M<sup>V</sup>P<sub>4</sub>O<sub>14</sub> compounds to determine whether or not superlattice reflections were present. A description of the instrumentation and

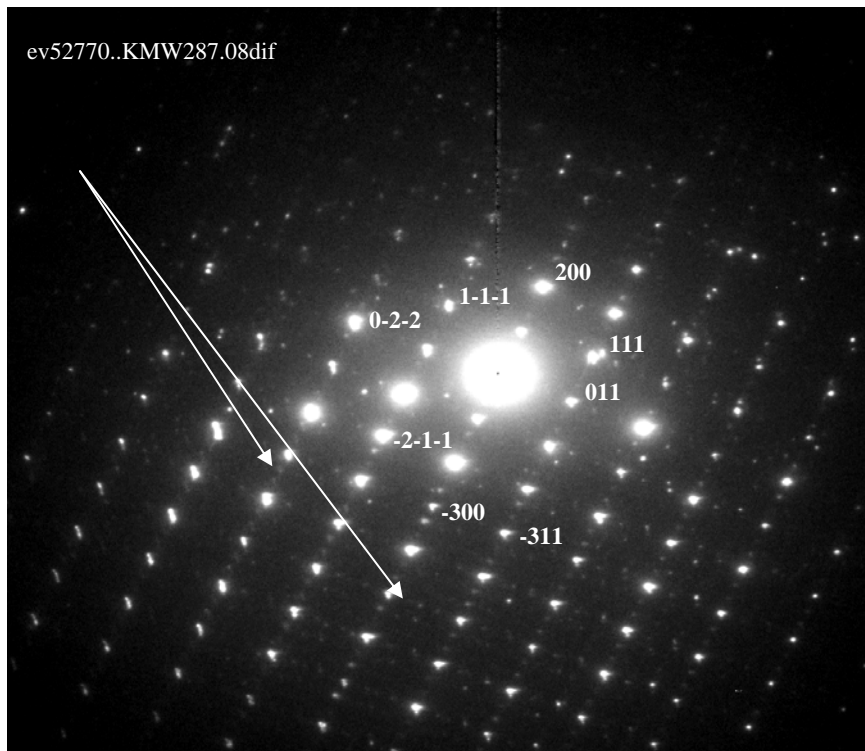


Figure 4.14: ED pattern of AlNbP<sub>4</sub>O<sub>14</sub> showing some reflections indexed on the subcell and weak supercell reflections indicated by the arrows. Weak reflections are in pairs horizontally and vertically across the pattern between the strong reflections.

calibration for this experiment was provided in Section 2.2. Figure 4.14 is an ED pattern of  $\text{AlNbP}_4\text{O}_{14}$  (KMW287). Arrows in Figure 4.14 point to weak reflections, two between each strong reflection horizontally and vertically across the pattern, which suggested possible tripling of the unit cell. D-spacing calculated from the ED pattern matched that found from the refined room temperature powder pattern for  $\text{AlNbP}_4\text{O}_{14}$ . The ED pattern was indexed with hkl values from the powder pattern. Figure 4.15 also shows superlattice reflections for this material.

Attempts to obtain good electron diffraction data for  $\text{InNbP}_4\text{O}_{14}$  and  $\text{YbNbP}_4\text{O}_{14}$  were unsuccessful. Crystallites appeared to be layered on top of one another. One ED pattern for the  $\text{YbNbP}_4\text{O}_{14}$  sample was clear of extraneous reflections, but indexing the ED data demonstrated the pattern probably belonged to an impurity phase.

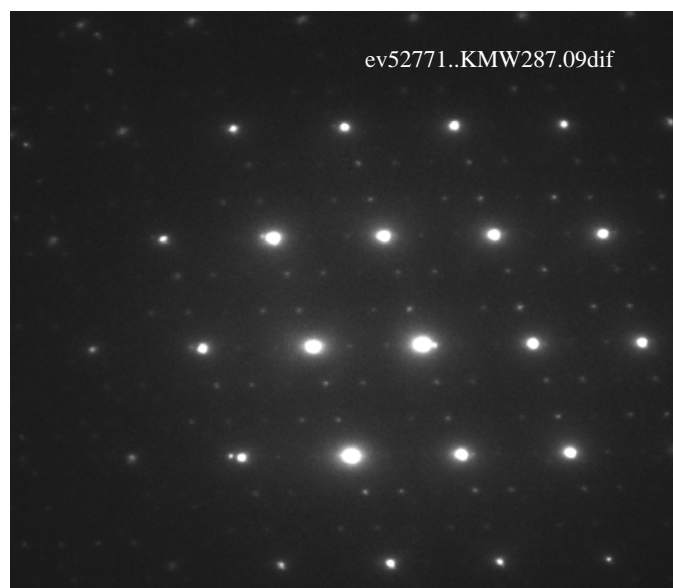


Figure 4.15: ED pattern of  $\text{AlNbP}_4\text{O}_{14}$  from the same crystallite shown in Figure 4.14. Weak superlattice reflections are apparent.

### 4.3 Conclusion

$M^{III}M^V$ -pyrophosphates were prepared over a relatively wide range of ionic radii and the compounds exhibited a wide range of CTEs over the temperature range explored. Room temperature lattice constants varied almost linearly with average ionic radii. Average linear CTE (600 – 900°C) versus average ionic radii also showed a linear trend, though imperfect.  $BiTaP_4O_{14}$ , the largest average ionic radii compound prepared, and  $ScNbP_4O_{14}$  displayed anomalous lattice constants and CTEs based on their size in comparison to lattice constants and CTEs for the other compounds. While  $BiTaP_4O_{14}$  has been reported to have some structural distortion due to an occupied  $6s^2$  orbital (suggesting a cause for the smaller than expected lattice constants and larger than expected CTEs), further study would be necessary to uncover the reasons for evidence of larger than expected lattice constants and smaller than expected CTEs for  $ScNbP_4O_{14}$ .

The analyses of powder diffraction patterns for the presence of superstructures did not provide absolute evidence for the presence or absence of superlattices in  $M^{III}M^V$ -pyrophosphates. Low intensity superlattice peaks could be missed or confused with impurity phases. More confidence was placed in the observed changes in lattice constants from thermal expansion studies and in TEM/ED.

Though no abrupt order/disorder transitions were observed in thermal studies for any of the compounds, temperature-induced phase changes were observed for  $AlNbP_4O_{14}$ ,  $InNbP_4O_{14}$ , and  $BiTaP_4O_{14}$ . CTEs estimated prior to the temperatures of phase transition for  $AlNbP_4O_{14}$  and  $InNbP_4O_{14}$  were comparable to that of low temperature  $ZrP_2O_7$ . The presence of a superstructure and possible long-range ordering in  $AlNbP_4O_{14}$  was supported by evidence from room temperature TEM/ED. Though weak reflections in the ED pattern can be attributed to other causes, such as double diffraction

or twinning,<sup>12</sup> it seems likely that a superlattice was correctly assigned. Though the CTE estimated prior to the phase transition for  $\text{BiTaP}_4\text{O}_{14}$  was high, it was not within a comparable range to that of the low temperature form of  $\text{ZrP}_2\text{O}_7$ . On the other hand,  $\text{BiTaP}_4\text{O}_{14}$  was found to have a CTE value comparable to cubic  $\text{ZrP}_2\text{O}_7$  in the temperature range between 300 – 600°C. All CTEs in the range 600 – 900 °C for the three compounds showed a decrease from that observed in the 300 – 600°C range. Though no phase transitions were observed for  $\text{AlTaP}_4\text{O}_{14}$  and  $\text{GaNbP}_4\text{O}_{14}$ , CTEs for the two compounds showed increases across the temperature ranges explored.

No changes in structures were observed in powder pattern analyses for compounds at any temperature. From this and other observations, a reasonable suggestion is that  $\text{AlNbP}_4\text{O}_{14}$ ,  $\text{AlTaP}_4\text{O}_{14}$ ,  $\text{GaNbP}_4\text{O}_{14}$ , and  $\text{InNbP}_4\text{O}_{14}$  may show order/disorder transitions at temperatures higher than those explored in this research. The phase transitions suggested by the data presented for  $\text{AlNbP}_4\text{O}_{14}$ ,  $\text{InNbP}_4\text{O}_{14}$ , and  $\text{BiTaP}_4\text{O}_{14}$ , however, raise questions about what changes, if any, are occurring to the structures of the compounds in the temperature range explored in this research.

#### 4.4 References

1. Varga, T., Wilkinson, A. P., Haluska, M. S., and Payzant, E. A., Preparation and thermal expansion of  $(M^{III0.5}M^{V0.5})P_2O_7$  with the cubic  $ZrP_2O_7$  structure. *Journal of Solid State Chemistry* 2005, 178, 3565-3570.
2. Harrison, D. E.; Hummel, F. A., Reactions in the System  $TiO_2$ - $P_2O_5$ . *J. Am. Ceram. Soc.* 1959, 42, 487-490.
3. Burdese, A.; Lucco Borlera, M., Sul sistema tra i pirofosfati di uranio e torio. *Ann. Chim. (Rome)* 1963, 53, 333-343.
4. Khosrovani, N.; Sleight, A. W.; Vogt, T., Structure of  $ZrV_2O_7$  from -263 to 470 °C. *J. Solid State Chem.* 1997, 132, 355-360.
5. Losilla, E. R.; Cabeza, A.; Bruque, S.; Aranda, M. A. G.; Sanz, J.; Iglesias, J. E.; Alonso, J. A., Syntheses, Structures, and Thermal Expansion of Germanium Pyrophosphates. *J. Solid State Chem.* 2001, 156, 213-219.
6. Gover, R. K. B.; Withers, N. D.; Allen, S.; Withers, R. L.; Evans, J. S. O., Structure and Phase Transitions in  $SnP_2O_7$ . *J. Solid State Chem.* 2002, 166, 42-48.
7. Verbaere, A.; Oyetola, S.; Guyomard, D.; Piffard, Y., New Mixed-Valence Antimony Phosphates:  $\alpha$ - and  $\beta$ - $Sb^{III}Sb^V(P_2O_7)_2$ . *J. Solid State Chem.* 1988, 75, 217-224.
8. Oyetola, S.; Verbaere, A.; Guyomard, D.; Crosnier, M. P.; Piffard, Y.; Tournoux, M., New  $ZrP_2O_7$ -like diphosphates of either mixed  $(M^{III}_{0.5}M^{V}_{0.5})$  cations (  $M=Sb$ ,  $Bi$ ,  $Hf$ ,  $Eu$ ;  $M'=Sb$ ,  $Nb$ ,  $Ta$ ) or  $M^V$  cations ( $M'=Ta$ ,  $Nb$ ): synthesis and structure. *Eur. J. Solid State Inorg. Chem.* 1991, 28, 23-36.
9. *JADE for XRD Pattern Processing, 7.0*; Materials Data, Inc.: Livermore, CA, 1995-2005.
10. Larson, A. C. V. D., R. B. *General Structural Analysis System, Win32*; Los Alamos Laboratory Report LAUR 86-748 Los Alamos National Laboratory: Los Alamos, NM, 2005.
11. Shannon, R. D., Revised Effective Ionic Radii and Systematic Studies of Interatomic Distances in Halides and Chalcogenides. *Acta Crystallographica, Section A* 1976, A 32, 751-767.
12. Withers, R. L.; Evans, J. S. O.; Hanson, J.; Sleight, A. W., An *in Situ* Temperature-Dependent Electron and X-ray Diffraction Study of Structural Phase Transitions in  $ZrV_2O_7$ . *J. Solid State Chem.* 1998, 137, 161-167.

## CHAPTER 5

### POSSIBLE AREAS FOR FUTURE STUDY

Further work on the structure of  $\text{PbP}_2\text{O}_7$  is needed, as a high quality model was not obtained in the current work. High resolution synchrotron powder XRD and neutron diffraction would help with this.

Evidence for a room temperature superstructure for  $\text{AlNbP}_4\text{O}_{14}$ , along with temperature-induced phase transitions for this compound,  $\text{InNbP}_4\text{O}_{14}$  and  $\text{BiTaP}_4\text{O}_{14}$ , raises questions as to what changes are occurring to their structures on heating. These issues may be addressed with the help of high quality neutron or synchrotron X-ray data at elevated temperatures.  $\text{GaNbP}_4\text{O}_{14}$ , which showed no phase transition  $< 900^\circ\text{C}$ , but did show increasing CTEs over the entire temperature range explored, should be included in this work as it may show a transition at higher temperatures.

## VITA

Kathleen White was born in Washington, D. C. to George L. and Victoria P. Madara. Her father was a career military officer and his assignments gave the family the opportunity to live in many areas of the United States and in Europe. Her mother was the daughter of Polish immigrants. Kathleen is married and has two adult children. She received her B.S. in Chemistry from Kennesaw State University, Kennesaw, Georgia in 1999 and accepted a graduate assistantship from the School of Chemistry and Biochemistry at the Georgia Institute of Technology, Atlanta, Georgia in 2000. Her Ph.D. work was under the direction of Dr. Angus P. Wilkinson. She earned a Ph.D. in Chemistry in August, 2006.